#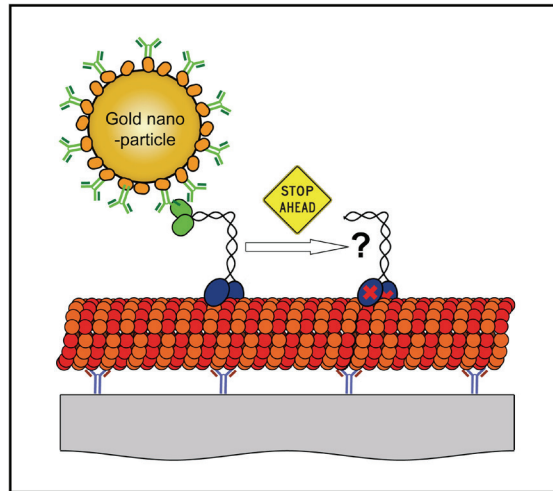 A novel parabolic prism-type TIR microscope to study gold nanoparticle-loaded kinesin-1 motors with nanometer precision

Dissertation

submitted for the degree of
Doctor rerum naturalium
(Dr. rer. nat.)
at the
Fakultät für Mathematik und Naturwissenschaften
Technische Universität Dresden
by

René Schneider

born on April 28th, 1983 in Dresden, Germany

Handed-in: November 1st, 2012
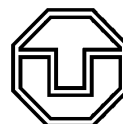Thesis defense: February 21st, 2013

List of reviewers:

Prof. Dr. Stefan Diez

B CUBE - Center for Molecular Bioengineering, Technische Universität Dresden,
Arnoldstraße 18, 01307 Dresden

Prof. Ph.D. Jonathon Howard

Max Planck Institute of Molecular Cell Biology and Genetics,
Pfotenhauerstraße 108, 01307 Dresden

ii

Erklärung entsprechend §5.5 der Promotionsordnung vom 23. Februar 2011

Hiermit versichere ich, dass ich die vorliegende Arbeit ohne unzulässige Hilfe Dritter und ohne Benutzung anderer als der angegebenen Hilfsmittel angefertigt habe; die aus fremden Quellen direkt oder indirekt übernommenen Gedanken sind als solche kenntlich gemacht. Die Arbeit wurde bisher weder im Inland noch im Ausland in gleicher oder ähnlicher Form einer anderen Prüfungsbehörde vorgelegt.

Die Dissertation wurde im Zeitraum vom 1. April 2009 bis zum 1. November 2012 verfasst und von Prof. Dr. Stefan Diez am B CUBE - Center for Molecular Bioengineering der Technischen Universität Dresden betreut.

Meine Person betreffend erkläre ich hiermit, dass keine früheren erfolglosen Promotionsverfahren stattgefunden haben.

Ich erkenne die Promotionsordnung der *Fakultät für Mathematik und Naturwissenschaften* der *Technischen Universität Dresden* an.

Dipl. Phys. René Schneider

Dresden, 1. November 2012

Summary

Movement of motor proteins along cytoskeletal filaments is fundamental for various cellular processes ranging from muscle contraction over cell division and flagellar movement to intracellular transport. Not surprisingly, the impairment of motility was shown to cause severe diseases. For example, a link between impaired intracellular transport and neurodegenerative diseases, such as Alzheimer's, has been established. There, the movement of kinesin-1, a neuronal motor protein transporting vesicles along microtubules toward the axonal terminal, is thought to be strongly affected by roadblocks leading to malfunction and death of the nerve cell. Detailed information on how the motility of kinesin-1 deteriorates in the presence of roadblocks and whether the motor has a mechanism to circumvent such obstructions is scarce. In this thesis, kinesin-1 motility was studied *in-vitro* in the presence of rigor kinesin-1 mutants, which served as permanent roadblocks, under controlled single-molecule conditions.

The 25 nm wide microtubule track, consisting of 13 individual protofilaments, resembles a multi-lane environment for transport by processive kinesin-1 motors. The existence of multiple traffic-lanes, allows kinesin-1 to utilize different paths for cargo transport and potentially also for the circumvention of roadblocks. However, direct observation of motor encounters with roadblocks has been intricate in the past, mainly due to limitations in both, spatial and temporal resolution. These limitations, intrinsic to fluorescent probes commonly utilized to report on the motor positions, originate from a low rate of photon generation (low brightness) and a limited photostability (short observation time). Thus, studying kinesin-1 encounters with microtubule-associated roadblocks requires alternative labels, which explicitly avoid the shortcomings of fluorescence and consequently allow for a higher localization precision.

Promising candidates for replacing fluorescent dyes are gold nanoparticles (AuNPs), which offer an enormous scattering cross-section due to plasmon resonance in the visible part of the optical spectrum. Problematic, however, is their incorporation into conventionally used (fluorescence) microscopes, because illumination and scattered light have the same

wavelength and cannot be separated spectrally. Therefore, an approach based on total internal reflection (TIR) utilizing a novel parabolically shaped quartz prism for illumination was developed within this thesis. This approach provided homogenous and spatially invariant illumination profiles in combination with a convenient control over a wide range of illumination angles. Moreover, single-molecule fluorescence as well as single-particle scattering were detectable with high signal-to-noise ratios. Importantly, AuNPs with a diameter of 40 nm provided sub-nanometer localization accuracies within millisecond integration times and reliably reported on the characteristic 8-nm stepping of individual kinesin-1 motors moving along microtubules. These results highlight the potential of AuNPs to replace fluorescent probes in future single-molecule experiments. The newly developed parabolic prism-type TIR microscope is expected to strongly facilitate such approaches in the future.

To study how the motility of kinesin-1 is affected by permanent roadblocks on the microtubule lattice, first, conventional objective-type TIRF microscopy was applied to GFP-labeled motors. An increasing density of roadblocks caused the mean velocity, run length, and dwell time to decrease exponentially. This is explained by (i) the kinesin-1 motors showing extended pausing phases when confronted with a roadblock and (ii) the roadblocks causing a reduction in the free path of the motors. Furthermore, kinesin-1 was found to be highly sensitive to the crowdedness of microtubules as a roadblock decoration as low as 1 % sufficed to significantly reduce the landing rate.

To study events, where kinesin-1 molecules continued their runs after having paused in front of a roadblock, AuNPs were loaded onto the tails of the motors. When observing the kinesin-1 motors with nanometer-precision, it was interestingly found that about 60 % of the runs continued by movements to the side, with the left and right direction being equally likely. This finding suggests that kinesin-1 is able to reach to a neighboring protofilament in order to ensure ongoing transportation. In the absence of roadblocks, individual kinesin-1 motors stepped sideward with a much lower, but non-vanishing probability (0.2 % per step). These findings suggest that processive motor proteins may possess an intrinsic side stepping mechanism, potentially optimized by evolution for their specific intracellular tasks.

Table of content

Abbreviations

ADP	Adenosine diphosphate
AOI	Angle of incidence
ATP	Adenosine triphosphate
AuNP	Gold nanoparticle
AuNP-motor	AuNP-loaded motor
AuNR	Gold nanorod
CCD	Charge-coupled device
CPD	Cumulative probability distribution
EM CCD	Electron-multiplied CCD
FLIC	Fluorescence interference contrast
GFP	Green fluorescent protein
GFP-motor	GFP-labeled motor
MAP	Microtubule-associated protein
MT	Microtubule
NA	Numerical aperture
PF	Protofilament
P_i	Inorganic phosphate
SM	Single-molecule
SNR	Signal-to-noise ratio
TIR	Total internal reflection
TIRF	Total internal reflection fluorescence

1. Introduction

In 1944, Nobel-prize decorated Erwin Schrödinger turned his attention to the newly emerging field of biophysics and speculated about the physical laws that govern the surprisingly ordered appearance of life [1]. His principle of 'order-from-disorder' nicely summarizes the fact that many biological processes, such as the beating of the heart, take place with an extremely high degree of order yet are driven by a myriad of individual events, such as the random diffusion of a molecule in solution. Due to the immense number of molecules, their detailed trajectories are hidden in the ensemble average. This circumstance sparked the interest in accessing and observing single molecules in their native environment to dissect the individual states that make up the ensemble. Along with others, Schrödinger's pioneering ideas paved the way and motivated today's single-molecule (SM) approaches applied in biophysics.

Coming of age in the 1970's, the rather young approach of SM biophysics tries to disassemble a certain biological process into its molecular constituents in order to identify and isolate the relevant building blocks necessary to drive the process. Eventually, biophysicists try to understand, characterize and quantify the specific function of a building block *in-vitro* (outside of the cell or *ex-vivo*), which often takes place at the SM level and therefore involves techniques with SM sensitivity (so-called SM techniques). Finally, the ultimate goal is to reassemble the relevant building blocks in order to reconstitute the biological process in a 'minimal system' [2].

Interestingly, the investigation of the specific function of a relevant building block is often only made possible by technological innovations. For example, an elegant innovation of such a SM technique was the patch clamp technique utilized by Neher and Sakmann in 1976 [3], who demonstrated the first time-resolved recordings of currents passing through an individual ion channel in a membrane. Major innovations that enabled the direct observation of single molecules under the microscope were the development of fluorescent markers and fluorescence microscopy, which so far culminated in (i) the

1

discovery of the green fluorescent protein (GFP) and a Nobel prize for Tsien, Chalfie and Shimomura in 2008 [4], (ii) the application of evanescent fields, notably already described by Sir Isaac Newton in 1704 [5], to TIR microscopy by Axelrod in 1981 [6], and (iii) the invention and development of highly sensitive charge-coupled device (CCD) cameras in 1969 and a Nobel prize for Smith and Boyle in 2009 [7]. Not surprisingly, the past decades are often referred to as being "the single-molecule years" [8].

Stunning examples of the direct observation of single molecules being at work in an *in-vitro* motility assay are the imaging of individual ATP turnover reactions of single myosins by Funatsu et. al. in 1995 [9], and kinesin-1 motor proteins moving along cytoskeletal filaments called microtubules (MTs) by Vale et. al. in 1996 [10]. These experiments applied the three aforementioned innovations in an ingenious manner and further enlivened the upcoming interest in such motility assays, which allow the reconstitution and thus observation of biomolecular transport in a controlled, artificial environment.

Today, the isolated kinesin-1 motor protein, being the relevant molecular constituent that drives intracellular anterograde transport along MTs, has been extensively studied. Recent publications therefore tend to investigate the interaction of kinesin-1 with other motor proteins [11], MT-associated proteins (MAPs) [12] and cargo-binding promoter proteins [13]. The inhibition of kinesin-1 was found to cause severe malfunction and disease phenotypes [14], some of which are also found in neurodegenerative diseases such as Alzheimer's [15]. There, a neuronal protein able to interact with the MT surface is strongly over-expressed and thus causes the tracks, necessary for kinesin-1 movement, to be highly decorated. Consequently, the influence of such 'roadblocks' on the motility of kinesin-1 is a biologically and medically relevant process to be investigated in detail.

An interesting observation was that kinesin-1 motor proteins were able to pass and circumvent roadblocks [16,17]. This might be an intrinsic property of many motor proteins since encounters with roadblocks *in-vivo* are expected to occur frequently given an enormous number of MAPs. The exact mechanism

by which motor proteins circumvent a permanent roadblock has been subject to speculation and only little is known about the nanometer-precise path a motor takes in order to overcome the blocked site. Serendipitously, the minimal system needed to reconstitute and investigate such impaired molecular transport of kinesin-1 requires the addition of only one kind of road-blocking proteins. This PhD thesis therefore aims on the direct observation of single kinesin-1 motor proteins dealing with permanent roadblocks and addresses the question of how kinesin-1 manages to get around the blocked site.

As characteristic for biophysics this project necessitates technological innovation. This is because fluorescent probes, such as GFPs, utilized to report on the molecules' position only provide imprecise positional information due to their low brightness and short lifetime. Highly promising candidates for replacing fluorescent probes are strongly scattering AuNPs, however their incorporation into existing fluorescence-based microscopes is intricate. Thus, a novel imaging apparatus, in the form of a parabolic prism-type TIR microscope, had to be developed, which allowed the collection of SM fluorescence and single-particle scattering signals in order to observe both, individual fluorescently labeled as well as AuNP-loaded motor (AuNP-motor) proteins with nanometer resolution.

The following section will provide an overview of the key proteins necessary to drive biomolecular transport *in-vivo*. Furthermore, the example of Alzheimer's disease is used to exemplify how impaired biomolecular transport is connected to malfunction and disease. The second section focuses on *in-vitro* motility assays, which resemble the ideal tool to study isolated motor proteins in a controlled environment. Subsequently, the key methods to impair the motility of motor proteins in such *in-vitro* assays are presented, which enables setting up an experimental routine to study the circumvention of roadblocks. Since nanometer-precise image information is needed to investigate the detailed path of a motor 'around' a blocked site, the principles of TIR microscopy and its extension toward the use of scattering AuNPs will be

addressed in the third and last section of this chapter. This will finally motivate the development of the parabolic prism-type TIR microscope, which forms the technological heart of this thesis.

1.1 Molecular transport *in-vivo* and its impairment

For an average eukaryotic cell, such as a fibroblast (Fig. 1, left), with a typical diameter of several tens of micrometers, the delivery of proteins produced near the nucleus to the places where they are needed relies in part on thermal diffusion. Similar to the way a drop of milk dilutes in a cup of coffee, a simple estimation of the time necessary for an average protein to get from the center of the cell to the outer membrane yields a time span of approximately one second[*]. Thus, thermal diffusion is fast enough to distribute the cells constituents reliably on micrometer length scales. However, this mechanism becomes insufficient when cells show extremely long extensions along one dimension. One such example is a neuron (Fig. 1, right), whose axons can span a distance of some hundreds of centimeters, e.g. in humans from the spinal cord to the food. In this case, the thermal diffusion of an average protein from the nucleus through the axon to the synapse will take approximately 250 years. From this estimation it can be concluded that such highly elongated cells must have evolved a directed mode of transportation.

It was therefore not to a surprise when scientists observed vesicles to be actively transported one-dimensionally along cytoskeletal filaments within the squid giant axon [18]. It was later found that all eukaryotic cells contain a stunningly complex and extremely specified set of proteins that drive and establish the transport machinery. Such proteins are called 'motor proteins' due to analogy to macroscopic motors. More remarkably even was the discovery that one single such molecule is able to move cargo processively along its cytoskeletal track [19].

---

[*]According to the one-dimensional diffusion equation $<x^2> = 2Dt$, with $<x^2>$ being the mean-square displacement, D the diffusion constant of an average 100 kDa protein of 70 $\mu m^2/s$ and, t the time span (for more details see [87]).
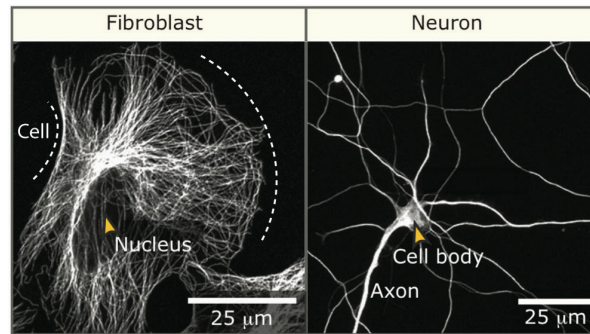
Fig. 1 | Different cell types require distinct transport mechanisms.
The various shapes and sizes of certain cell types require that their transport network be organized differently. In the human fibroblast (left) few individual transport filaments (MTs) are visible and stretch from the cell nucleus to the outer membrane. In the neuron (right), a myriad of such filaments is packed together into bundles forming the long, thin axon projections extending from the cell body to the presynaptic terminal. Adapted from [20].

Today, three families of motor proteins acting on cytoskeletal filaments are known. First, the actin-based myosin family, and second the two MT-based families of dynein and kinesin. Although some of the motor proteins in the three families are highly specialized on vastly different biological processes (e.g. myosin is involved in muscle contraction, dynein is involved in flagella movement of sperm, and kinesin is involved in spindle organization), each family contains motors that are involved in intracellular long-range transport. This work focuses on the founding member of the kinesin family, namely kinesin-1 [21], which moves with typical velocities of some micrometers per second reducing the time needed to reach the synapse to only a few days, which is 10,000-fold faster than thermal diffusion.

Microtubules – the multi-lane track for kinesin motors

MTs are protein polymer tubes with a diameter of 25 nm made from α- and β–tubulin heterodimers (Fig. 2). These 110 kDa heterodimers self-assemble head-to-tail into protofilaments (PFs) and thereby constitute a 'traffic lane' in which the transport direction is structurally encoded by the directionality of α–/β–tubulin dimers, somewhat comparable to human footsteps in the snow. The β-tubulin decorated end of the MT is called the plus

end and typically points away from the center of the cell toward the outer membrane.

Inside cells, typically 13 PFs, each with a diameter of approximately 6 nm [22], assemble in parallel to form the tubule. When MTs are reconstituted *in-vitro*, the number of PFs can vary, in extreme cases from 9 to 17, depending on the polymerization conditions. Such non-13-PF MTs show a supertwist in their structure, resulting in helical continuation of the PFs along the MT centerline [23].
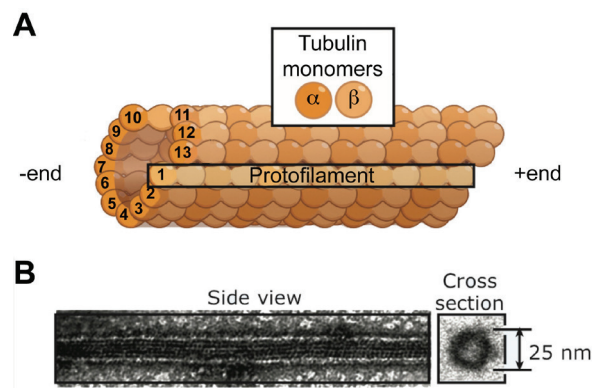
Fig. 2 | Microtubule polymers are made of tubulin heterodimers.
(A) Individual α-/β-tubulin dimers assemble head-to-tail into protofilaments whereupon 13 of those arrange side-by-side to form the hollow MT. (B) Electron micrographs of MTs polymerized *in-vitro* from purified tubulin. Adapted from [20].

MTs are extremely stiff polymers with a persistence length in the range of millimeters [24], however they are also subject to a rapid switching between growing and shrinking phases, called 'dynamic instability'. This behavior provides the cell with a mechanism to permanently rearrange and recycle its MT tracks, e.g. when responding to external cues or when initiating cell division. The dynamic instability can be inhibited by the addition of cytostatic drugs, such as paclitaxel [25], which was applied throughout this work.

Kinesin-1 – a robust long-range transporter of vesicular cargos

The kinesin-1 motor protein, formerly called 'conventional kinesin', is a 120 kDa homodimeric protein (also termed heavy chain dimer) that consists of (i) two N-terminal motor domains (also termed motor heads) necessary for binding into the gap between α- and β-tubulin subunit [26], (ii) an 14 amino acid neck linker region necessary for coordination between the two motor heads [27], and (iii) a dimerization domain (Fig. 3, [28,29]). The full-length
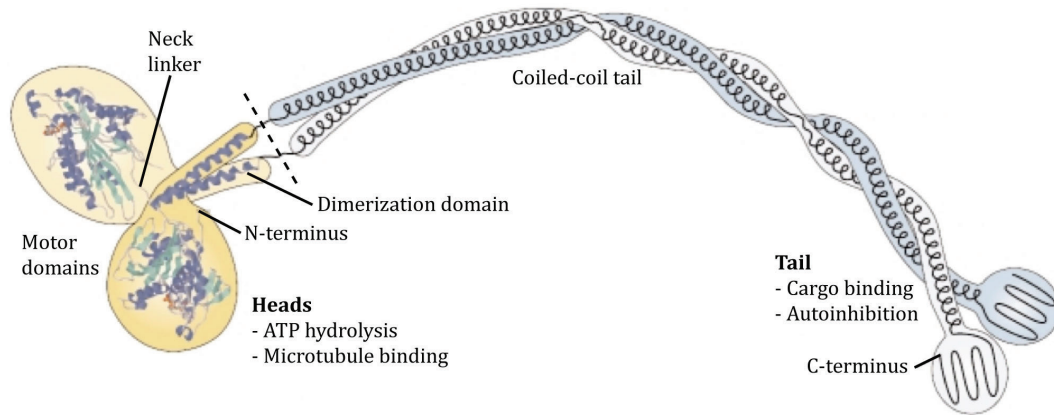
Fig. 3 | Structure of the full-length kinesin-1 heavy chain dimer.
The crystal structure of the motor and dimerization domains is available, whereas the structure of the coiled-coil tail is inferred from electron microscopic images and coiled-coil prediction analyses. Adapted from [30].

protein features a large coiled-coil stalk, which (i) provides binding sites for regulatory light chains and (ii) contains a C-terminal tail domain that functions as inhibitor for both motor domains but is activated upon cargo-binding [13,31,32]. This autoinhibition mechanism is one reason why this motor protein is often studied with a truncated tail where the protein chain is terminated behind the first dimerization domain (see dashed line in Fig. 3) [33,34]. Such a truncated protein dimer, which contained the first 430 amino acids of the kinesin-1 heavy chain, was used throughout this thesis. Notably, the dimeric motor protein was expressed in a GFP-labeled and an unlabeled variant, having a molecular weight of 150 kDa and 100 kDa, respectively.

Both motor domains use energy derived from the hydrolysis of ATP to perform consecutive steps of 16 nm, which translocates the center-of-mass of

the dimeric molecule by 8 nm per step. This distance corresponds to the spacing of the α-/β-tubulin dimers along one PF. Both heads thereby move in a hand-over-hand mechanism, similar to the human bipedalism, toward the plus end of the MT with a velocity in the range of one micrometer per second [35]. On average, a single motor can take several dozens of consecutive steps before detaching from the MT lattice, which gives a low probability for detaching in the range of 1 % per step. Furthermore, single kinesin-1 molecules were shown to work against forces in the range of 5 pN *in-vivo* [36]. Thus, the kinesin-1 motor protein is highly optimized for the fast and long-ranged transport of large objects such as vesicles and organelles away from the nucleus. Quite importantly, it was shown that kinesin-1 walks along a single PF path [34,37], with a low probability of stepping to the side [38].

During the stepping process the motor heads cycle alternately through a complex hydrolysis pathway, which can be simplified to four nucleotide-states in each head. In direction of hydrolysis these are: the three strongly-bound no-nucleotide, ATP and ADP+ P_i states and the weakly bound ADP state. Excellent reviews of the current model of the kinesin–1 stepping mechanism can be found in [39-41]. Briefly, in solution, both motor heads (for simplicity called A and B in Fig. 4) are in the ADP state [41]. Attachment of head A to the MT triggers the release of its ADP. Head A is now in the no-nucleotide state and hence strongly bound whilst head B is weakly bound. Following ATP binding to head A, internal strain is exerted onto head B causing it to undergo a biased diffusional search for the next forward binding site. After hydrolysis of ATP into ADP+P_i in head A, head B is allowed to make a connection to the next forward binding site, release its ADP and switch into the strongly-bound no-nucleotide state. Upon P_i-release, the energy available from ATP hydrolysis is now being used to detach head A from the former binding site and switch into the weakly bound ADP state. With the binding of ATP to head B the hydrolysis cycle can restart anew.

8

The strong binding of ATP requires a short amino acid sequence, termed Walker A motif[*] [42], which is a distinct feature of all kinesin motor domains. It contains a lysine (K) residue crucial for binding to the β-phosphate of the ATP molecule. A single-point mutation of the following threonine (T) to asparagine (N) or isoleucine (i) has been shown to cancel the motor protein's ability to bind ATP [16,43]. Because these mutated proteins are still able to bind strongly to the MT but unable to perform steps, they are termed 'rigor mutants'.
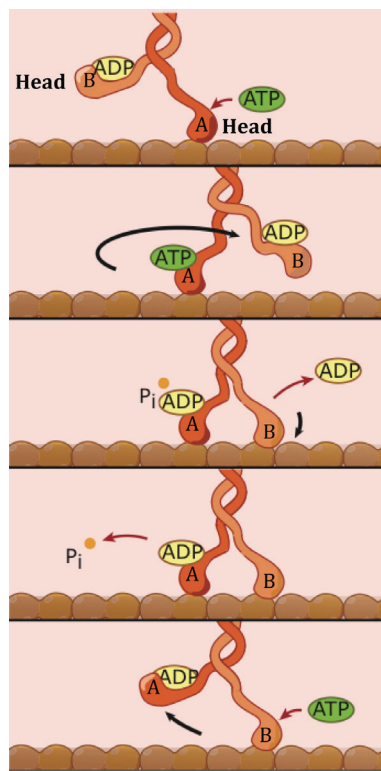
Fig. 4 | Current model of the kinesin-1 hydrolysis cycle.
The nucleotide state in one head changes several times in response to the nucleotide state of the other head. Coordination is facilitated via the neck linker (not depicted here). Adapted from [20].

Impaired molecular transport *in-vivo*

Both MT-based motor families, dynein and kinesin, are responsible for the axonal transport in neurons [44-46]. Whereas dynein motor proteins are moving toward the minus end of MTs, facilitating 'retrograde' transport toward the cell center, kinesin motor proteins are responsible for 'anterograde' transport away from the center. This process delivers newly synthesized

---

[*]Amino acid sequence: GXXXXGK(T/S), using the standard abbreviations for glycine (G), lysine (K), threonine (T), and serine (S). X denotes any amino acid.

material, such as mRNA and proteins packaged into vesicles [47] and assembled neurofilaments [48], to the axon's presynaptic terminal.

Impairment of anterograde transport, either by mutation of motor or cytoskeletal proteins or as a consequence of neurodegenerative processes, has been shown to cause severe dysfunctions and neurodegenerative diseases [14,15]. Neurodegenerative diseases have experienced increased attention over the past decade because they pose a huge economical impact on the senescent societies in developed countries [49].

An example of how impaired molecular transport of motor proteins is involved in neurodegenerative processes was proposed for Alzheimer's disease [50]. There is indication that the MT-stabilizing protein tau [51] is overexpressed in early stages of the disease causing the MT to be highly decorated [52]. This process is thought to interfere with MT-based transport causing an increased probability for motors to encounter tau roadblocks [12,53-55]. In a later stage, the neuron reacts on highly decorated MTs by hyperphosphorylation of the tau protein [56], which subsequently detaches from the MT lattice and leaves behind an unstabilized, vulnerable MT. At this stage, the MT-severing protein katanin was shown cut the MT tracks into pieces [57], which leads to hindered supply of the presynaptic terminal of this axon. The hyperphosphorylated tau proteins assemble into huge protein aggregates (termed tau tangles), which appears to be an characteristic and unifying feature in neurodegenerative diseases [58]. Interestingly, confirmation of affection of a patient with Alzheimer's disease is done by directly observing atrophy of brain matter and accumulation of protein aggregates, which only occur in the latest stage of the disease. It is therefore highly promising to investigate cellular processes that are affected during early onset of the disease, such as the anterograde transport by kinesin-1, and thus be able to diagnose Alzheimer's disease at an earlier stage in the future. In order to do so, detailed knowledge about how kinesin-1 operates in a crowded environment is necessary. This approach requires control over the environment of the motor protein, i.e. the 'crowdedness' or density of

roadblocks on the MT lattice, which is hardly controllable within cells. To circumvent this problem, the interaction of motor proteins with MTs is often studied outside of the cell, in the controlled environment of so-called *in-vitro* motility assays.

1.2 Molecular transport *in-vitro* and its impairment

To study the movement of individual motor proteins along MTs under controlled SM conditions, the minimal system for molecular transport is reconstituted on inorganic substrates, such as glass coverslips [10,19,21,59,60]. This is achieved by two complementary approaches: (i) In so-called 'gliding motility assays' (Fig. 5A), the purified motor proteins are immobilized on a glass coverslip and MTs, polymerized from purified tubulin, are propelled by the motors, comparable to a stage diver surfing on the crowd below. (ii) In contrast, so-called 'stepping motility assays' (Fig. 5B), utilize the inverted geometry, where MTs are immobilized on the glass coverslip via antibodies and motor proteins are added to interact individually with the provided tracks.
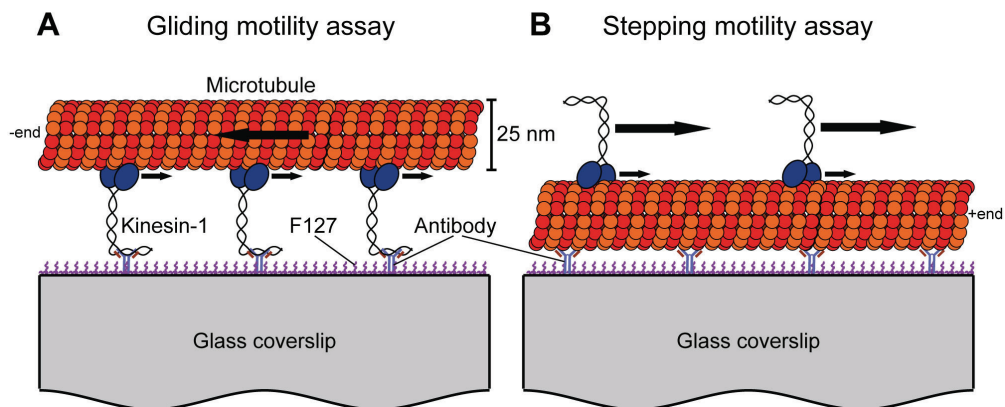

Fig. 5 | *In-vitro* motility assays.
(A) Gliding motility assays, where surface-bound motor molecules propel the MTs and (B) stepping motility assays, where the MTs are immobilized on the surface and motors walk on them.

Typically, both assays are performed in flow cells, where two glass coverslips are glued together by stripes of, for example, double-sided sticky tape (see [60,61] and the Materials and methods chapter, page 99). The volumes between the stripes define channels, which allow the quick exchange of solutions enabling the step-by-step treatment of the surface with different solutions.

Impaired molecular transport *in-vitro*

The effect of roadblock density on the motility of kinesin-1 has been studied *in-vitro* using various kinds of either native roadblocks, such as purified neuronal proteins [12,55,62], cell extracts [16], slower motors [63,64] and motor proteins in crowding conditions [64,65], or artificial roadblocks, such as streptavidin and quantum dots [17], single-headed [63,66] and double-headed [16,65] kinesin rigor mutants. These results contributed debatable aspects to the ongoing discussion of kinesin-1 dealing with roadblocks:

a) **Reduced mean velocity due to waiting phases:** Once a motor landed on a roadblock-decorated MT, the mean velocity was reduced in most cases using non-native roadblocks. This is thought to originate from short waiting phases of motors being confronted with a permanent roadblock. Direct observation of such waiting phases was so far only performed in [16,17,67]. Interestingly, the mean velocity of kinesin-1 transport was not or only mildly affected by native roadblocks [53,55].

b) **The duration of waiting phases:** Controversy arises over the probability and length of waiting phases. Telley et. al. [16] found waiting phases one order of magnitude smaller than the unimpeded kinesin-1 dwell time – the total time bound to the MT – resulting in a low probability for waiting. In contrast, Dr. Till Korten found rather extended waiting phases in the order of 0.5 s in his PhD thesis [67]. Despite these differing results, both authors suggest the detachment rate – the inverse of the pausing time – to be enhanced when the motor is facing a roadblock.

c) Reduced run length and dwell time: The extent to which the SM motility parameters run length – the total distance covered on the MT – and dwell time are affected by roadblocks remains a matter of debate. Comparative studies quantifying both parameters in presence of native and non-native roadblocks are rare but revealed a strongly reduced run length and dwell time [16,67]. Other publications focusing on either run length or dwell time also found decreased values in presence of roadblocks [12,17,62,63,66]. Somewhat contradictory results, where the run length as well as the dwell time remained constant [55,63] or even increased [65] were published, however these results may be affected by the harsh MT treatment applied in [63] or the lack of SM control in [65].

d) Reduced landing rate: There is mounting evidence that the landing rate of motors on roadblock-decorated MTs is reduced, presumably because the number of free binding sites is diminished [12,16,55,62,65].

e) Motors were able to circumvent permanent roadblocks: Surprisingly, it was found that kinesin-1 motor proteins were able to overcome a permanent roadblock in some cases and continued their walk normally [12,16,17,63]. Controversy arises over the mechanism by which kinesin motors accomplish this demanding task, given the fact that undisturbed kinesin-1 motors mainly follow a single PF [34,37].

Given the fact, that native neuronal MAPs bind reversibly to the MT lattice and might be removed by actively stepping motors, poses a problem for the controlled investigation of roadblock encounters in *in-vitro* motility assays. To study the specific scenario of kinesin-1 motors running into a permanently occupied binding site, kinesin-1 rigor mutants, which bind irreversibly to the MT and thereby block the path of the motors, were utilized throughout this thesis. A promising approach, offering valuable information on the behavior of kinesin-1 in a crowded environment would furthermore involve the utilization of fluorescently labeled roadblocks, because this allows answering the

question whether the decrease in the motility parameters can be explained by the mean spacing of roadblocks along the MTs,

Mechanisms to overcome roadblocks

Several mechanisms for kinesin motor proteins to overcome a permanent roadblock have been proposed earlier [16,17,38,63,65,66,68,69] and involve (i) the detachment of the motor protein from the MT upon encountering a roadblock followed by diffusional search and immediate re-attachment to another free PF, (ii) removal of the permanent roadblock from the MT lattice due to competition for the same binding site, and (iii) side stepping to neighboring PFs.

a) Immediate detachment of a motor upon encounter of a permanent roadblock is likely because first the dwell time was found to decrease, which is a sign for enhanced detachment when blocked by a roadblock, and second the probability for waiting was shown to remain low in presence of roadblocks [16,17]. However, the immediate rebinding to the MT lattice, which happens on the millisecond timescale, depends on the diffusion constant of the motor. Since the diffusion of a molecule cannot be slowed down, such events remained unresolved in earlier studies since the temporal resolution of fluorescence-based imaging techniques is often too low to capture this process.

b) The removal of roadblocks or the temporary freeing of an occupied binding site is a reasonable mechanism for native neuronal MAPs, which explains the mild effect of tau on kinesin-1 velocity, both *in-vivo* [53] and *in-vitro* [65]. Even more convincing is the fact that the physiological tau-to-tubulin ratio in neurons is between 0.025 to 0.05 (1 μM tau to 20 μM - 40 μM assembled tubulin, [70]), which converts into a mean spacing of roadblocks in the range of approximately 300 nm along a single PF. The high *in-vivo* velocity of kinesin-1 of 1.8 μm/s [35], would therefore translate into a rate of approximately six roadblock encounters per second. Given this high rate and the mild effect tau caused on the run length and dwell time of kinesin-1 leads to the hypothesis that tau proteins – and maybe other neuronal MAPs as well –

are transiently removed from the proximity of the motor binding site or may not fully occupy the motor binding site [71]. Further research has to clarify the timescales of the association between native MAPs and MTs, both in absence and presence of motors.

       c) The hypothesis of side stepping of motor proteins has gained increased attention in the last years. Since kinesin-1 has a low probability of side stepping and therefore mainly follows a single PF path [34,37,38], it can be speculated whether PF tracking is an intrinsic feature of kinesin-1 only or of the whole kinesin superfamily. Quite surprisingly, other processive proteins of the kinesin superfamily, such as kinesin-8 (kip3), were shown to follow the PF path less strictly, having a pronounced 10 % chance to move toward the left PF for every forward step taken [68]. Therefore, it can be speculated that the kinesin-1 motor is evolutionary optimized for immediate detachment upon roadblock encounter to allow ongoing transportation on a neighboring PF or to hand over the job of transportation to another motor protein bound to the same cargo. This is backed by theoretical investigations [72] and experimental *in-vivo* studies [36]. It is speculated that the length of the kinesin-1 neck linker of about 4 nm allows the binding to a tubulin dimer on a neighboring PF [38,63]. This poses the question whether kinesin-1 might be able to utilize this pathway when confronted with blocked binding sites.

1.3 Imaging of molecular transport using TIR microscopy

       To study the motility of single kinesin-1 motor proteins in presence of roadblocks and the exact mechanism by which they manage to overcome a roadblock, *in-vitro* assays in combination with camera-based, wide-field TIR microscopy were performed. In TIR microscopy a laser beam is guided under shallow angles onto an interface separating a substrate from a medium with lower refractive index (Fig. 6). Above a critical angle of incidence (AOI) the impinging laser beam is totally reflected. However, part of the light penetrates the medium with the lower refractive index in the form of an exponentially decaying evanescent field. This allows illumination of entities, e.g. fluorescent

or scattering probes, which are within a layer of approximately 100 nm (the so-called 'penetration depth') from the interface, whereas entities further away are not illuminated.
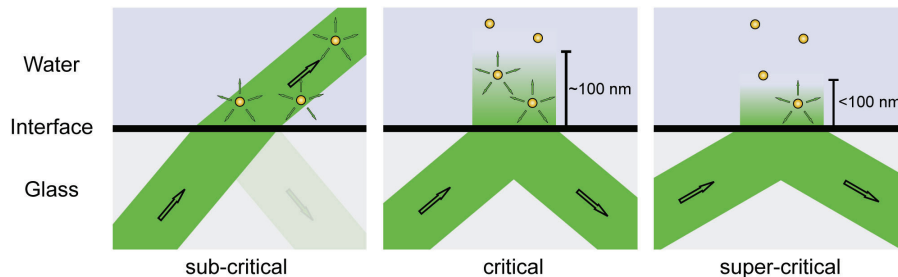

Fig. 6 | Principle of TIR illumination.
A laser beam impinges under increasing AOIs onto the glass-water interface (black solid line), which resembles a jump in the refractive index from 1.52 in the coverslip to 1.33 in the water medium. For sub-critical angles (left), the laser beam is refracted and propagates unhindered through the water medium, illuminating entities even far away from the interface. Only a small part of the incoming light is reflected. TIR occurs at AOIs bigger than the critical angle (middle) generating a spatially confined evanescent field with a typical penetration depth of the exponentially decaying intensity of 100 nm. Further increasing the AOI reduces the penetration depth even more (right), thus restricting illumination to only those entities very close to the interface.

In the first TIR microscopes, laser light was guided onto the interface by a variety of prism-shapes made of glass or quartz (Fig. 7A). Their construction is straightforward and the optics theory well described (see Axelrod et. al. [73] for an excellent review). Among the applications of prism-type TIR microscopes in biology, material science, and medicine [73,74] are studies regarding surface interactions of ligands with lipid membranes [74], cell adhesion to substrates [6], and vesicle transport inside cells [74]. Despite these successful experiments, prism-type TIR microscopy is nowadays only a side arm of the imaging community and no prism-type TIR microscope has made the step into the commercial market.

This fruitless development of prism-type TIR microscopes originated from recent achievements in constructing high NA objectives that enable the setup of objective-type TIR microscopes (Fig. 7B). In particular, when the NA exceeds the refractive index of the medium to be penetrated, shallow-angle

illumination above the critical AOI – and thus TIR illumination – can be achieved by guiding a thin laser beam through the periphery of the objective's pupil. Today, objective-type TIR has become the method of choice for fluorescence applications in cell biology for the following reasons: (i) The technique is easily implemented into existing microscopes because the laser beam is brought to the back-focal plane of the objective by simple insertion of an optical element (such as a dichroic mirror) into the illumination path. (ii) Changing the AOI is achieved easily by moving the laser beam within the back-focal plane of the objective. Connected to that is a change in penetration depth that is important for quantitative microscopy. Quite importantly, during this procedure the illuminated area remains at the same location, a fact not readily achieved in prism-type TIR microscopy. (iii) Using an inverted microscope, cell experiments in open dishes are possible because both, illumination and imaging, occur from the bottom. Consequently, objective-type TIR operation is facile and commercial systems have penetrated the market already for more than a decade [73].
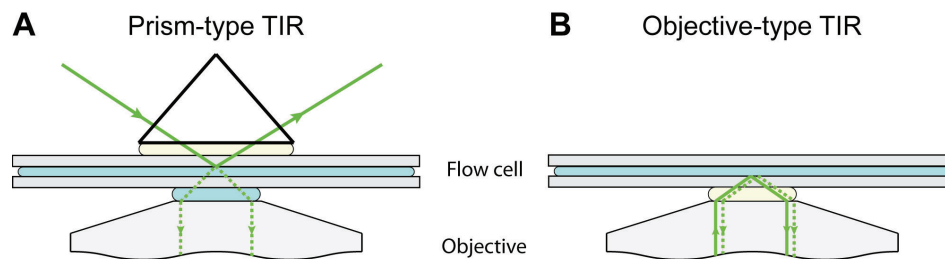
Fig. 7 | Prism- versus objective-type TIR microscopy.
(A) In prism-type TIR various prism geometries can be applied to guide the illumination laser beam (green solid) onto the sample surface. Detection light (green dashed) is captured with a water immersion objective from below. (B) In objective-type TIR a high numerical aperture (NA) oil immersion objective is used to guide the illumination laser beam (green solid) onto the sample surface. Detection light (green dashed) is captured along the same pathway and requires a separation method, e. g. by spectral filters.

Nonetheless, illumination and detection paths overlap in objective-type TIR (see Fig. 7B). The particular strengths of this method therefore lies in imaging fluorescent probes, where excitation and emission wavelengths differ

from each other, hence rendering spectral separation possible. Thus, a common approach involves the application of motor proteins labeled with a fluorescent tag. Unfortunately, such fluorescent proteins, organic dyes, or quantum dots suffer from photobleaching, photon blinking, fluorescence saturation, and/or a low number of photons being generated upon excitation [75-77]. These features impose restrictions when fast and precise localization or long-term observation of single molecules or particles is necessary [78]. This poses a major hurdle here, since nanometer-precise information is desired for the detailed study of kinesin-1 motor proteins overcoming roadblocks. Serendipitously, the above mentioned disadvantages can be overcome by a multitude of scattering probes, out of which strongly scattering AuNPs are among the most promising ones [79-82].

AuNPs as imaging probes

AuNPs exhibit an enormous scattering cross-section in the visible part of the optical spectrum due to plasmon resonance [79,83]. For example, the scattering cross-section of a 40 nm AuNP is approximately 50,000 times larger than the fluorescence emission cross-section of a GFP molecule (see detailed comparison in Table 1). Thus, for equal illumination intensities, a 40 nm AuNP generates a four orders of magnitude larger number of photons than a single GFP molecule. In effect a 40 nm AuNP resembles a 500-fold more effective imaging probe compared to a GFP molecule, taking into account the cross-sectional areas of both probes (last row in Table 1). Moreover, AuNPs provide long-term stability and allow for a versatile surface chemistry. Interestingly, because generation of photons relies on elastic scattering, AuNP emission rates do not saturate, which is in stark contrast to fluorescent probes [84]. Consequently, the number of scattered photons scales linearly with the applied illumination power and allows adjustment of the AuNP brightness to the imaging requirements. This impressive comparison underlines the potential of AuNPs for the nanometer-precise imaging and localization of single molecules.

Table 1 | Optical properties of a GFP molecule and a 40 nm AuNP.

Physical property	GFP molecule	40 nm AuNP	Comparison to GFP molecule
Radius	2.1 nm[a]	20 nm	10 times larger
Cross-sectional area	13 nm^2	1300 nm^2	100 times larger
Volume	40 nm^3	35000 nm^3	1,000 times larger
Absorption cross-section[b]	0.007 nm^2 (at 489 nm)	3000 nm^2 (at 532 nm)	400,000 times larger
Emission/scattering cross-section[c]	0.006 nm^2 (at 509 nm)	300 nm^2 (at 532 nm)	50,000 times larger
Effective cross-section[d]	0.05 %	23 %	500 times more effective

[a]assuming GFP is spherical.

[b]measured at maximum; GFP value calculated from molar absorption of 41800 M^{-1}cm^{-1} [85]. AuNP value estimated from [79,83].

[c]GFP value estimated using quantum efficiency of 0.79 [86]. AuNP value estimated from [79].

[d]emission/scattering cross-section relative to cross-sectional area.

AuNPs as nano-mechanical probes

A drawback of AuNPs however, is their larger size compared to fluorescent proteins, which alters the mechanical properties of a AuNP-loaded protein (see detailed comparison in Table 2). Furthermore, the probe may cause sterical constraints either on the movement of the motor protein itself or when stepping along the surface-bound MT. As a consequence, a AuNP-loaded average protein diffuses around seven times slower than an unloaded average protein (compare last row in Table 2). Nevertheless, the drag force of a 40 nm AuNP transported by a kinesin-1 motor protein with a velocity of about 1 µm/s is in the femtonewton (fN) regime, which is at least three orders of magnitude smaller than the maximum stall force of kinesin-1. Hence, the velocity of AuNP-loaded kinesin-1 motor proteins is expected to remain unaltered provided the particle causes no further sterical constraints.

Table 2 | Mechanical properties of an average protein and a 40 nm AuNP.

Property	Average protein	40 nm AuNP	Comparison to average protein
Density	$1.38 \cdot 10^3$ kg/m^3	$19.3 \cdot 10^3$ kg/m^3	14 times denser
Radius	3 nm	20 nm	7 times larger
Volume	120 nm^3	35000 nm^3	300 times larger
Molecular mass	100 kDa	400,000 kDa	4000 times heavier
Drag coefficient[a]	60 pN·s/m	380 pN·s/m	From Stokes' law: $\sim$ 7 times higher
Diffusion coefficient[a]	70 µm^2/s	10 µm^2/s	From Einstein relation: $\sim$ 7 times slower

Values for the average protein are adapted from [87]. Values for AuNPs are calculated accordingly.

[a]In water at 20°C

Despite the highly promising arguments for imaging, AuNPs come for a prize, which is their challenging incorporation into objective-type TIR setups. This is because the totally reflected beam remains in the detection path and – having the same wavelength – dominates over the scattered signal (see solid and dashed green lines in Fig. 7B). If the totally reflected beam were to be reliably blocked only a restricted observation area would remain [88]. Interestingly, this problem is solved in prism-type TIR where the totally reflected illumination beam is naturally rejected from entering the detection path (compare with Fig. 7A). However, prism-type TIR setups in turn have the disadvantage that the quick and comfortable usage, i.e. changing of the AOI, and hence the penetration depth of the evanescent field, is more troublesome compared to objective-type TIR. Moreover, while changing the AOI, the illuminated area can vary widely, in extreme cases even leaving the current field of view. These disadvantages arise directly from the commonly applied polygonal shapes of the prisms, which do not provide a focal spot to which the illumination laser beam can be focused. Therefore, a novel approach based on a parabolically shaped prism was developed in this thesis, which allows the detection of SM fluorescence as well as single-particle scattering with high signal-to-noise ratios (SNRs). Due to the parabolic shape of the prism, adjusting the AOI becomes straightforward as it only necessitates the

translational movement of the incoming laser beam in one direction (see also [89], where a similar strategy based on a parabolically shaped mirror has been used for the high-throughput imaging of single DNA molecules). During this procedure the illuminated area remains at the same location, which resembles a distinct feature of this prism-type TIR setup, resulting in a mechanism by which the AOI is adjusted comparable to objective-type TIR. Moreover, our setup requires only low constructional efforts, which makes it an attractive tool worth being patented [90].

The next chapter reports on the optical and geometrical properties of the newly developed parabolic prism-type TIR setup, and provides a quantitative comparison of detection efficiencies and SNRs in prism- and objective-type TIR fluorescence (TIRF) microscopy. Furthermore, the high potential of scattering probes to achieve localization errors on the nanometer scale will be demonstrated by loading AuNPs to kinesin-1 motor proteins. To utilize the precise imaging of AuNP labels to the biophysical problem of roadblock circumvention a two-step approach was taken: First, the third chapter addresses the question of how the motility of kinesin-1 is effected by varying densities of roadblocks sitting on the MT lattice. Answering this question involves measuring the mean velocity, run length, dwell time and landing rate, which are parameters that can be obtained performing conventional objective-type TIRF microscopy providing low spatial and temporal resolution for the fluorescently labeled motors. Secondly, the fourth chapter focuses on the behavior of kinesin-1 when encountering and waiting in front of a permanent roadblock. There, the direct observation of the circumvention step requires the AuNPs and the parabolic prism-type TIR setup to be utilized. This approach provides the resolution needed to directly observe motor proteins overtaking roadblocks.

2. A novel parabolic prism-type TIR microscope

In order to combine the advantages of prism- and objective-type TIR, a new approach based on a parabolically shaped quartz prism has been developed. Parabolically shaped surfaces are attractive for microscopy applications because they focus light, which travels parallel to the optical axis of the paraboloid into the focal spot and, vice versa, light emanating from the focal spot leaves the paraboloid in parallel to the optical axis [89,91-98]. These properties were used to construct a parabolic quartz prism where the AOI of the illumination light could be adjusted between 45° and 72° by translational movement of a single mirror (Fig. 8A and Supporting Fig. 1 in the Appendix chapter A.1, page 109). As an additional benefit, the quartz material allows efficient TIR illumination with ultraviolet wavelengths, a feature not yet available for TIRF objectives.

2.1 Optical properties of the parabolic prism-type TIR

Assuming a critical angle α_{crit} for TIR at the sample interface of 61°, TIR illumination was possible for AOIs above this value[*]. Dependent on the NA of the imaging objective, smaller AOIs resulted in dark-field and bright-field illumination, respectively. Coupling the parabolic quartz prism to the top of a glass-made microscopic flow cell at variable heights by immersion oil – with refractive index larger than that of quartz – allowed to always position the focal spot vertically at the glass-water interface (see Fig. 8A and Supporting Fig. 2 in the Appendix chapter A.2, page 111).

---

[*]The critical angle is calculated by $\alpha_{\mathrm{crit}} = \mathrm{ArcSin}(n_{\mathrm{water}}/n_{\mathrm{glass}})$; refractive indices for the glass substrate and the water medium of $n_{\mathrm{glass}} = 1.52$ and $n_{\mathrm{water}} = 1.33$ were used, respectively.
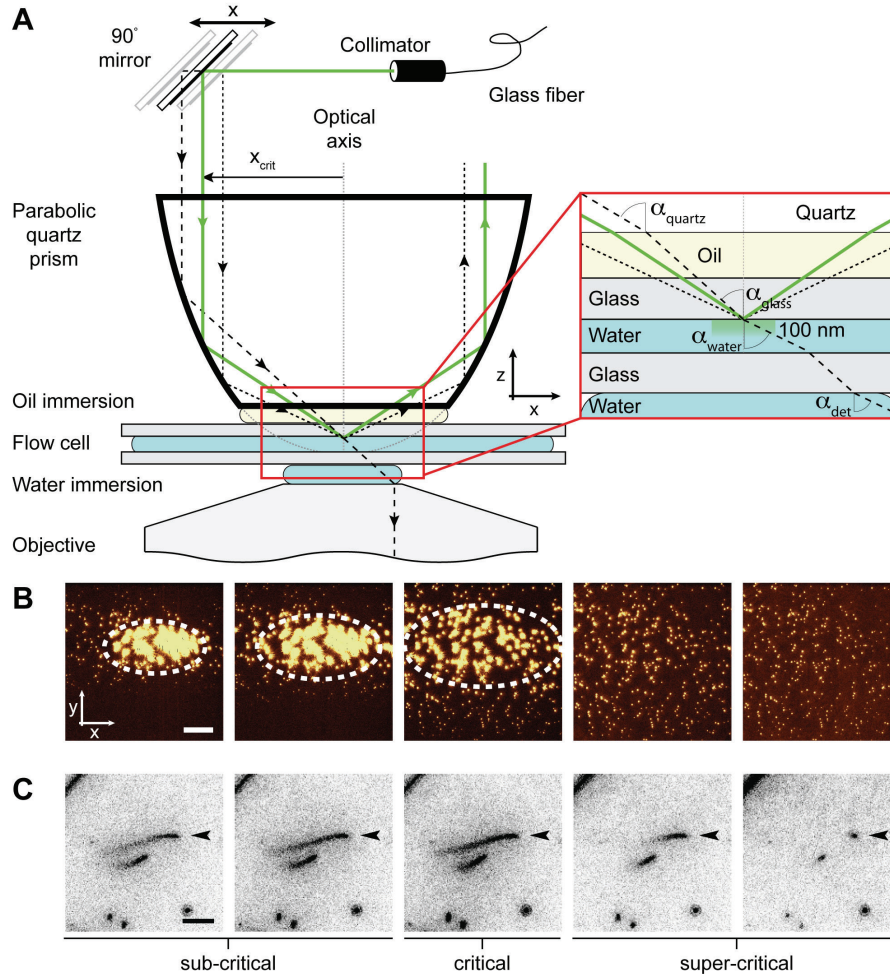
Fig. 8 | Design and application of the novel parabolic prism-type TIR.
(A) Collimated illumination light is vertically directed into the parabolic quartz prism by a 90° mirror which can be moved horizontally. Depending on the position of the mirror, the beams enter the prism at different distances from the optical axis (dashed black, solid green, and dotted black lines). They are reflected at different positions on the parabolic surface and reach the spatially invariant focal spot at the glass-water interface with different angles. Various modes of illumination (e.g. TIR illumination for angles larger than the critical angle) are achievable and imaging is carried out on an inverted microscope through the objective from the bottom. (B) The size of the illumination area can be varied by the adjustable fiber collimator. Substrate-attached 40 nm AuNPs were illuminated with a 532 nm laser. The illumination area was increased from a minimal size of 90 x 35 μm² up to larger than 130 x 130 μm² (left to right). Bar size: 25 μm. (C) The AOI can be varied using the translational movement of the 90° mirror. Fluorescently labeled MTs (arrow), bound to the glass surface with one end and pointing away from the surface with their remaining parts in a tilted orientation, were illuminated with a 532 nm laser while successively increasing the AOI from low, sub-critical angles (left) to high, super-critical angles (right). Bar size: 10 μm.

Changing the size of the illuminated area

The size of the illuminated area could be varied by an adjustable fiber collimator. This was tested using 40 nm AuNPs (Fig. 8B) and fluorescently labeled streptavidin molecules unspecifically attached to the glass surface of the flow cell (see Supporting Fig. 3 in the Appendix chapter A.3, page 112). The minimum size of the illuminated area, approximated by a 2D-Gaussian, was found to be in the order of 90 x 35 μm^2 at the glass-water interface. This area is smaller than the ones typically obtained by conventional objective-type TIR setups and may provide an advantage for applications where large optical power densities in the sample plane are desired.

The asymmetric shape of the illuminated area followed from two reasons: First and foremost, the illumination light impinges onto the glass-water interface with a finite AOI. Therefore, a horizontal cross-section through the beam profile creates an elliptically shaped area, leading to stronger confinement in *y*-direction. Secondly, the curvature of the parabolic surface perpendicular to the optical axis is higher than the curvature parallel to the optical axis. This leads to enhanced focusing of the collimated illumination laser beam in *y*-direction. Defocusing the laser beam by means of the adjustable fiber collimator allowed continuous variation of the illumination area up to a size larger than 130 x 130 μm^2. Notably, all illumination profiles observed in these experiments exhibited a high degree of homogeneity. Uneven illumination, interference fringes and effects of shadowing, which are often inherent to conventional objective-type TIR setups due to refractive index inhomogeneities in the illumination pathway [99,100], are thus avoided using parabolic prism-type TIR.

Changing the AOI of the illumination laser

The AOI of the illumination light could be varied by the translational movement of a single mirror. Accordingly, the penetration depth of the illumination light changed as demonstrated by the use of fluorescently labeled MTs (Fig. 8C, see Appendix chapter A.4, page 113). MTs primarily landed end-

on, causing the remaining parts of the MTs to point away from the surface in a tilted orientation. Similar to previous results, where tilted MTs had been used to measure and calibrate the TIR penetration depths [101], a clear change in MT appearance became visible when successively increasing the AOI from low, sub-critical to high, super-critical angles. At the former condition ($\alpha_{glass} < \alpha_{crit}$), the parts of the MTs near the surface appeared with moderate intensities. The imaging contrast smoothly decreased along the lengths of the tilted MTs due to defocussing and background excitation. At the critical angle ($\alpha_{glass} = \alpha_{crit}$), the fluorescence intensity near the surface reached a maximum. The penetration depth became finite leading to vertically restricted excitation of the tilted MTs as well as the background. For super-critical angles ($\alpha_{glass} > \alpha_{crit}$), the fluorescence intensity near the surface remained high but decayed rapidly along the MTs due to the decreased penetration depth. During AOI adjustment, the illumination area remained at the same position.
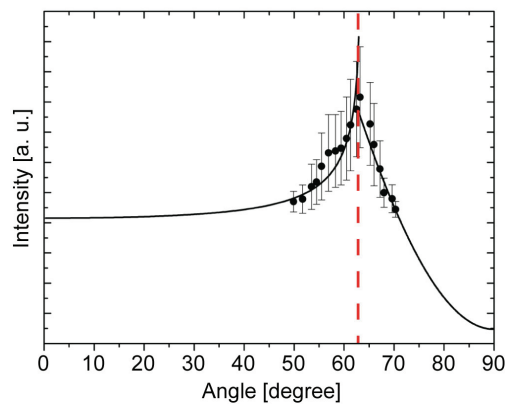
Fig. 9 | Scattered light intensity as a function of the AOI.
The scattered intensity of 40 nm AuNPs (mean ± sd, N = 262 particles) is plotted versus the AOI applied to the TIR interface. A fit with the corresponding Fresnel equations yielded a critical angle of 63° (red dashed line) in agreement with the estimated critical angle of 61° and previous results obtained with a similar system [101].

When repeating the same kind of experiments with surface-immobilized 40 nm AuNPs, the scattered light intensities as a function of the AOI was in agreement with the corresponding Fresnel equations for sub- and super-critical angle illumination (Fig. 9). Varying the AOI starting from low

sub-critical to high super-critical angles led to a pronounced enhancement in the average scattered intensity and decreased rapidly when the critical angle was exceeded.

2.2 Quantitative comparison of prism- and objective-type TIRF microscopy

Comparative studies investigating the illumination and detection efficiencies for TIRF microscopy inherent to prism- and objective-type setups are rare [102]. To benchmark the parabolic prism-type TIR setup in comparison to objective-type TIR, SNRs in images obtained from individual GFP-labeled kinesin-1 molecules attached to surface-immobilized MTs were investigated (Fig. 10, see the Materials and methods chapter, page 99).
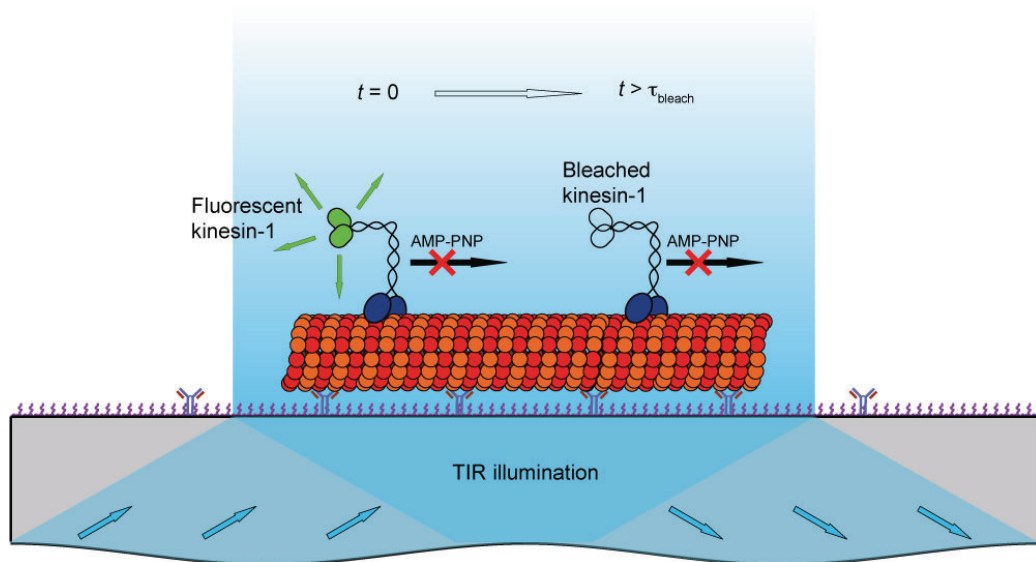
Fig. 10 | SM bleaching assay based on the geometry of a stepping assay.
A glass coverslip, treated with Pluronic F127 to block against unspecific protein adsorption, was decorated with anti-tubulin antibodies to hold rhodamine-labeled MTs on the surface. Individual GFP-labeled kinesin-1 motor proteins were immobilized on the MTs by the presence of the non-hydrolyzable ATP-analogue AMP-PNP. Initially ($t = 0$), all GFP molecules are active and emit fluorescence while after a period ($t > \tau_{bleach}$) most of the molecules are bleached.

To allow for a fair comparison, equal power densities of the evanescent fields need to be adjusted in both setups. Due to the different geometries of the illumination pathways in prism- and objective-type TIR (Fig. 11A and B), it is not sufficient to simply adjust equal laser powers entering the quartz prism or the microscope objective. This is because equal laser powers do not
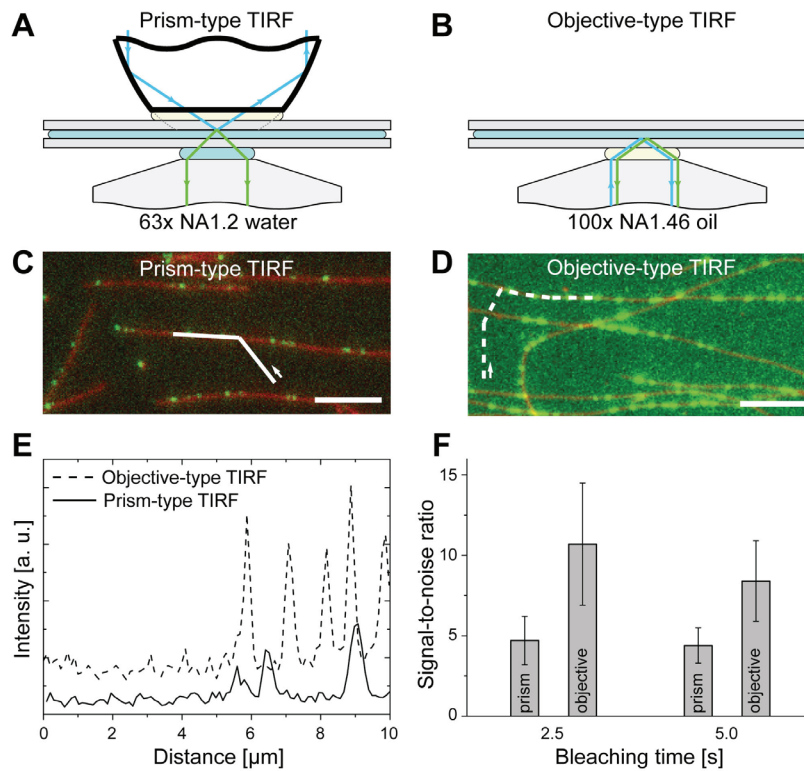
Fig. 11 | Comparison of prism- and objective-type TIRF.
Illustration of the parabolic prism-type TIRF (A) and objective-type TIRF (B) setups where critical-angle illumination (blue line) is performed on the far side (A) and on the near side (B) of the objective, respectively. SM fluorescence (green line) is captured using a 63x NA1.2 water objective (A) and a 100x NA1.46 oil objective (B). Example images of individual GFP-labeled kinesin-1 motor molecules (green) immobilized on MTs (red) by the presence of AMP-PNP using parabolic prism-type TIRF (C) and objective-type TIRF (D). The illumination laser powers were adjusted such that equal bleaching times occurred in both setups. Bar size: 5 μm. (E) Line scans taken from (C) and (D) showing lower background levels and lower noise for prism-type TIRF (solid curve) but higher signal amplitudes for objective-type TIRF (dashed curve). (F) The comparison of SNRs calculated from experiments performed at bleaching times of 2.5 s and 5.0 s shows lower SNRs for prism-type TIRF (SNR = 4.8 ± 1.5 and 4.4 ± 1.1) as compared to objective-type TIRF (SNR = 10.7 ± 3.8 and 8.4 ± 2.5).

necessarily convert into equal power densities directly in the evanescent field due to differences in the illuminated area. Therefore, a method based on the bleaching times of the investigated fluorescent molecules was developed. This is reasonable because the bleaching times deterministically decrease with increasing power density [103,104]. Vice versa, equal bleaching times are expected to originate from equal power densities in the evanescent fields.

For both setups, the GFP signal was maximized by adjusting the AOI to the critical angle and avoided premature bleaching. For the results to be evaluated in the following, the laser powers were adjusted such that the GFP molecules bleached within 2.5 ± 0.3 s (mean ± sd; $N = 225$ molecules) and 2.5 ± 0.1 s ($N = 362$) for prism-type and objective type TIRF, respectively (see Fig. 11C-E for typical images and intensity line scans obtained under these conditions).

It appeared that prism-type TIRF performed better than objective-type TIRF in terms of low background levels* (about one third compared to objective-type TIRF) and low noise levels** (about one half compared to objective-type TIRF). On the other hand, objective-type TIRF produced higher peak intensities*** (about four times compared to prism-type TIRF). Using prism-type TIRF, a SNR**** of 4.8 ± 1.5 (mean ± sd) was obtained, in contrast to objective-type TIRF with a SNR of 10.7 ± 3.8 (Fig. 11F). At bleaching times of 5 s, the SNRs decreased to 4.4 ± 1.1 ($N = 61$, prism-type TIRF) and 8.4 ± 2.5 ($N = 375$, objective-type TIRF). At equal power densities, objective-type TIRF thus allowed for SNRs around twofold larger than prism- type TIRF.

For both, prism-type and objective-type TIRF, the dependence of the optical noise on the amplitude of the fluorescence intensities was described by the same square-root relationship (see Supporting Fig. 4 in the Appendix chapter A.5, page 114). As a consequence, the SNR also depended on the

---

*Defined as the mean pixel intensity values in regions without fluorescent molecules.

**Defined as the standard deviation of pixel intensity values in regions without fluorescent molecules.

***Defined as the amplitudes of the Gaussians fitted to pixel intensity values of fluorescent molecules.

****Defined as peak intensities divided by noise levels.

amplitude by a square-root relationship: on average, four times more photons collected in the objective-type TIRF measurements compared to the prism-type setup thus result in an about twofold better SNR. In order to explain this difference, a multitude of factors that lead to increased detection of photons for objective-type TIRF has to be considered:

(i) The emission patterns of dipoles close (less than 50 nm) to an optical interface (e. g. glass-water) is strongly shifted toward the medium with the higher refractive index [105]. This leads to enhanced emission toward the glass coverslip and thus the objective in objective-type TIRF. Using an excellent discussion by Enderlein and Ruckstuhl [105], the percentage of photons being emitted toward the glass coverslip and toward the water medium was estimated to 72 % and 28 %, respectively. Similar values of 74 % and 26 % (i.e. a ratio of about 3 in favor of objective-type TIRF) were directly measured (see the Appendix chapter A.6 and the Supporting Fig. 5, page 116).

(ii) The NAs of the C-Apochromat 63x NA1.2 W Korr objective used for prism-type TIRF and the αPlan-Apochromat 100x NA1.46 objective (both Zeiss) used for objective-type TIRF were different. Consequently, both objectives collect different amounts of light, the ratio of which can be obtained by relating the integral areas of spherical cones with opening angles *2·ArcSin(NA/n)* to each other. In our case, this estimation led to a factor of about 1.3 times more photons being collected in objective-type TIRF.

(iii) In the spectral range of the GFP emission, the transmission of the high-NA objective used in the objective-type TIRF setup was 0.9 times the transmission of the objective used in the prism-type TIRF setup (data provided by the objective vendors).

(iv) Light attenuation through the additional 100 μm layer of water present in the prism-type TIRF setup allowed for a 1.1 times more efficient light capture in the objective-type TIRF setup. Taken together, objective-type TIRF collects a factor of 3.9-fold (3 × 1.3 × 0.9 × 1.1) more photons than prism-type TIRF, mainly due to efficient nearfield coupling of molecules to the glass substrate. As a consequence, the expected difference in SNRs for both setups

yields a factor of 1.96 (square root of 3.9), in good agreement with the twofold difference being experimentally measured. Notably, this difference in the SNRs was imposed by the experimental conditions adjusted for equal bleaching times in both TIRF setups. In fact, the sensitivity of the SNR on the excitation power was confirmed by measurements at 4-fold lower laser power in objective-type TIRF yielding SNRs similar to the ones obtained in our prism-type TIRF experiments (see Supporting Fig. 4, page 114).

2.3 Sub-nanometer localization precision of 40 nm AuNPs

SM experiments often involve the accurate localization of the imaged entities down to well below the pixel size of the image [33,40,82]. Such a high precision relies on the fact that (i) the peak positions of Gaussian photon distributions can be determined with much smaller errors than the optical resolution limit and (ii) that these localization errors scale inversely with the square root of the number of collected photons. The large scattering cross-section of AuNPs gives them a distinct advantage with regard to the latter criterion. In the following section a method to determine the localization error is introduced and later applied to compare the localization precision of individual GFP molecules and 40 nm AuNPs.

Defining and determining the localization error

To quantify the localization precision of light-emitting objects, the center positions were determined by fitting their images to two-dimensional Gaussians (Fig. 12) using FIESTA tracking software [106]. The positions obtained in every frame of the acquired image sequence resemble a normal distribution around the mean position. The width of the distribution is termed 'localization error' and was estimated by using a Maximum-Likelihood method. As the localization error is strongly dictated by the total number of collected photons per frame N, the 'volume' under the fitted distribution was converted into photons using the camera's sensitivity (see Materials and methods chapter, page 99).

In essence, the localization error measures the standard error of the mean of the pixelated intensity distribution. Therefore, a rule of thumb for estimating the localization error can be applied, taking into account (i) the standard deviation given by the resolution limit of approximately half the
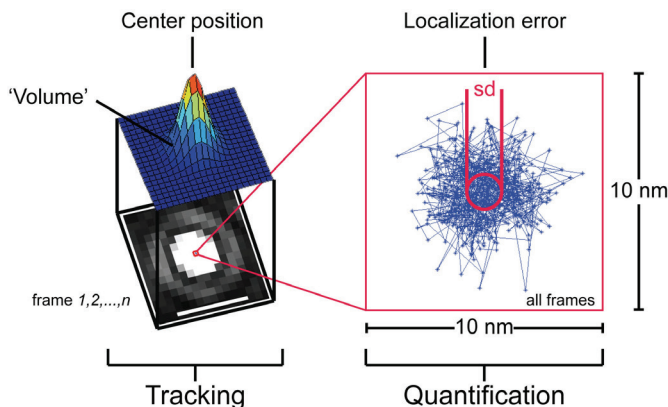
Fig. 12 | Determination of the localization error.
Tracking of a light-emitting entity (bottom left, bar size: 1 µm) was performed by fitting a two-dimensional Gaussian to its pixelated intensity distribution in every frame of an image sequence and yielded the center position and the volume intensity (number of total digital counts below the Gaussian). Quantification of the localization error is achieved by determining the standard deviation of the distribution of center positions. Note that the distribution of center positions fits into a box $(10 \times 10 \ nm^2)$ much smaller than the area of a pixel (here: $100 \times 100 \ nm^2$).

wavelength λ of the emission light, and (ii) the number of events being captured provided by the number of collected photons per frame N. For example, the localization precision of a single object emitting 100 photons at a wavelength of 500 nm can be estimated to

$$\sigma = \frac{\lambda}{2\sqrt{N}} = \frac{250 \ nm}{\sqrt{100}} = 25 \ nm.$$

In principle, the localization error can be made arbitrarily small. However, this necessitates an extremely large number of photons being emitted from an individual entity. The application of brightly scattering AuNPs to the protein of interest is therefore an ideal approach to harness nanometer-precise spatial information of the molecule's position.

Localization precision of GFP molecules and 40 nm AuNPs

To demonstrate the potential of brightly scattering AuNPs in combination with parabolic prism-type TIR the localization precision of individual GFP molecules and 40 nm AuNPs were compared in a configuration where both labels were attached to kinesin-1 motor proteins bound to surface-immobilized MTs (Fig. 13A and the Materials and methods chapter, page 99).
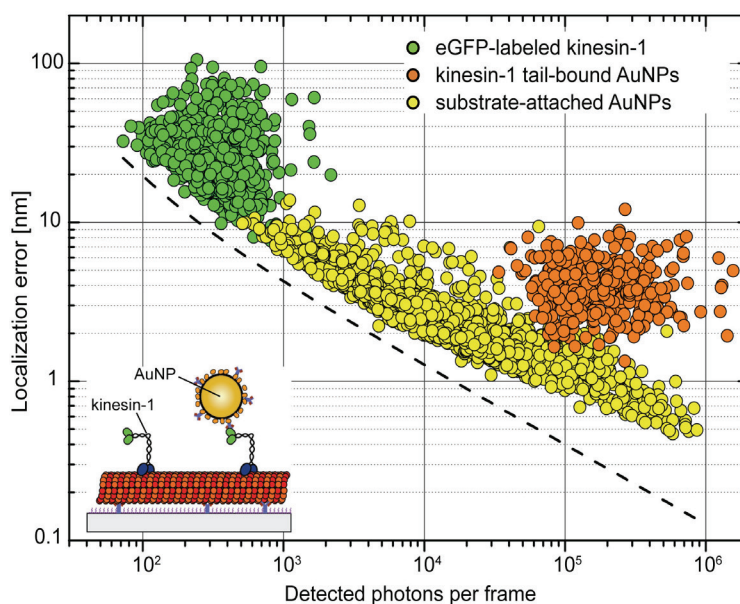
Fig. 13 | Localization precision for GFP molecules and 40 nm AuNPs.
(A) The localization errors as functions of the number of detected photons per frame for: GFP molecules at the tails of kinesin-1 motor proteins bound to substrate-attached MTs (green dots) and 40 nm AuNPs bound to the GFP molecules (orange dots, see inset for molecular geometries) as well as 40 nm AuNPs directly attached to the substrate (yellow dots). Each dot represents the localization error of an individual GFP molecule or 40 nm AuNP. Motor proteins were rendered immobile to the MTs by the presence of AMP-PNP.

Moreover, the limits of localization precision of 40 nm AuNPs directly immobilized on the substrate surface were explored. Single GFP molecules attached to kinesin-1 motor proteins on surface-immobilized MTs were localized to a precision of 28 ± 13 nm (mean ± sd, $N = 1009$ molecules) by collecting between 100 to 1000 photons within a 100 ms acquisition time (Fig. 13A, green dots). Notably, only in the very best cases the localization error was below 10 nm. When streptavidin-conjugated 40 nm AuNPs were loaded onto

the tails of kinesin-1 motors via biotinylated GFP antibodies the localization error was determined to be 3.8 ± 1.8 nm (mean $\pm$ sd, $N = 385$ particles, Fig. 13A, orange dots). In this case, the number of collected photons ranged from 100,000 to 1,000,000 within a 30 ms acquisition time. For similar numbers of detected photons, substrate-bound 40 nm AuNPs were localized with errors well below 1 nm (Fig. 13A, yellow dots). This improvement in localization precision was attributed to the avoidance of positional fluctuations of the 40 nm AuNPs due to the molecular flexibility of the kinesin-1 tails. In the very best cases, substrate-attached 40 nm AuNPs were localized with a precision of 5 Å. The dependency of the localization error on the number of collected photons was well predicted by theory over four orders of magnitude (Fig. 13A, dashed line). The slight deviations of the experimental data from the predicted behavior are assumed to mainly originate from systematic errors in determining the actual photon number (below 10,000 detected photons per frame) and spatial drift (above 10,000 detected photons per frame, see the Materials and methods chapter, page 99).
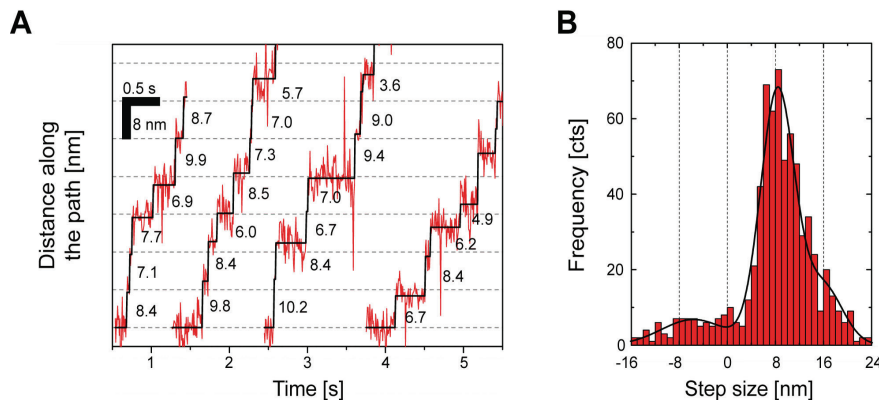
Fig. 14 | AuNPs report on the characteristic 8-nm stepping of kinesin-1.
(A) Stepwise motion of 40 nm AuNPs attached to kinesin-1 motors walking along MTs in the presence of 1 µM ATP (velocity of 17 nm/s $\pm$ 6 nm/s, mean $\pm$ sd, $N = 22$). The distance along the path (red line) was examined with a step-finding algorithm (black line). (B) Histogram of step sizes calculated from 22 AuNPs performing a total of 715 steps. A minor fraction of steps was found at +16 nm, which corresponds to two consecutive steps that were too fast to be resolved individually.

Finally, 40 nm AuNPs were applied to study the stepping of kinesin-1 motor proteins along MTs. This was done in a stepping assay by replacing AMP-PNP by 1 µM ATP which subsequently produced linear movement of AuNPs. The trajectories of 22 transported AuNPs (measured with 15 ms acquisition time) were projected onto their linearized path (Fig. 14A). A step-finding algorithm [107] was applied and yielded a step size histogram with a major peak at 8.3 ± 4.0 nm (mean ± sd, $N = 498$ steps, Fig. 14B), agreeing well with the spacing of α-/β-tubulin dimers along a PF as well as the step sizes formerly obtained by polystyrene beads and quantum dots attached to kinesin-1 tails [60,108]. The broad width of the peak is mainly attributed to the AuNPs being flexibly coupled to the kinesin-1 motors via streptavidin, biotinylated GFP antibodies, GFP at the motor tails and the tails themselves (estimated total linker length about 45 nm). Because no external forces are applied, the particles are free to undergo tethered diffusion around the MT-interacting kinesin-1 motor domains. Notably, the width of the peak (4.0 nm) is in agreement with the localization precision of 3.8 nm obtained for 40 nm AuNPs attached to immobilized kinesin-1 motors. The reduction of localization precision due to linkage flexibility can be overcome in setups with external force application, e.g. in optical tweezers. There, the linkage can be strained limiting the tethered diffusion to the direction perpendicular to the applied force. However, this strategy comes at the cost of not being able to measure on a load-free system. A second reason for the broad peak is freely diffusing AuNPs present in the flow channel. These particles occasionally penetrate the observational TIR field and contribute a fluctuating optical background to the image, reducing the ability to localize the AuNPs of interest with 1 nm precision in each frame. In fact, the latter problem is also present in SM fluorescence experiments, where the localization precision likewise decreases in the presence of free fluorophores in solution.

2.4 Discussion

The quartz-based, parabolic prism-type, wide-field TIR setup presented here enables the detection of SM fluorescence and single-particle scattering with high SNRs. Moreover, due to the parabolic shape of the prism, adjusting the penetration depth of the evanescent field can be readily achieved by the translational movement of only one mirror. Notably, this is possible while keeping the illuminated area at the same location, an important property when the detection of both, weak fluorescent as well as strong scattering signals in the same assay are envisioned. This is because (i) the excitation of single fluorophores is optimal at the critical AOI due to a peak in the evanescent intensity (compare Fig. 9) and (ii) a reduced optical background due to a shorter penetration depth rather than optimal illumination is desired for scattering probes. Hence, an optimal AOI for both imaging probes is quickly found by sampling a range of AOIs while illuminating the same area on the sample. Construction of the device, easily implementable into any commercial microscope in place of the usual bright-field condenser, is straightforward. In comparison to objective-type TIR setups, our approach (i) allows to work at AOIs well exceeding the critical angle for TIR, thus making the illumination of ultra-thin sample layers possible and (ii) enables the detection of scattering signals with low background. Together with the Carl Zeiss Imaging GmbH, the concept of parabolic prism-type TIR was filed as a German patent application in 2011 [90] and the results presented in this chapter have been published [109].

To quantitatively compare the performance of prism-type and objective-type TIR setups in fluorescence applications, a novel calibration method based on the characteristic bleaching times of single molecules was introduced. It was found that objective-type TIRF generally collects more photons than prism-type TIRF, mainly because near-field-emission into the glass substrate (i.e. into the direction of the image-collecting objective) is enhanced [105]. On the other hand, prism-type TIR setups exhibit lower background signals due to the decoupling of illumination and detection light

paths [102]. This feature becomes of particular interest for the imaging of scattering probes where no spectral separation between illumination and emission light is possible. Prism-type TIR is thus the method of choice for the imaging of scattering probes, which naturally overcome the intrinsic limitations of photobleaching, photon blinking, and saturation inherent to fluorescent probes.

Using the scattered light of 40 nm AuNPs illuminated by the parabolic prism-type TIR setup with acquisition times in the range of 10 ms, localization precisions below 1 nm were achieved, proving the applicability of these particles for the detection of conformational changes of biomolecules. The high localization precision relies on the facts that (i) the peak positions of Gaussian photon distributions can be localized with much smaller errors than the optical resolution limit and (ii) that the localization error scales inversely with the square root of the number of collected photons. The enormous scattering cross-section of AuNPs gives them a distinct advantage with regard to the latter criterion. Proving the applicability of these particles for the detection of conformational changes of biomolecules, the characteristic 8-nm steps of individual kinesin-1 motor proteins walking along the surface of MTs was successfully imaged. Consequently, parts of the results of this chapter are about to be published [109].

Having established and characterized the parabolic prism-type TIR setup, allowing for SM fluorescence and single-particle scattering to be detected with high SNRs , the biophysical problem outlined in the introduction can be tackled. To be more precise, the interest lies in (i) the extent to which the motility of kinesin-1 motor proteins is affected by increasing densities of permanent roadblocks and (ii) how kinesin-1 motor proteins proceed when getting stuck in front of a permanent roadblock.

Therefore, the next chapter focuses on the problem of how the motility of kinesin-1 changes in response to the number of permanent roadblocks bound along the MT lattice. Answering this question mainly involves measurement of the motility parameters, run length, dwell time, mean

velocity, and landing rate of single motors in dependence of the roadblock density. Therefore, conventional stepping assays utilizing objective-type TIRF microscopy will be performed. Notably, since the determination of the motility parameters of single motors does not require extremely precise spatial and temporal resolution, conventional GFP-labeled motor (GFP-motors) proteins suffice to accomplish this task. Quite antithetic, answering the second part of the biophysical problem in the second next chapter requires both, nanometer-precise localization and millisecond temporal resolution. This is because (i) nanometer-precise spatial information is desired to gain information about the specific pathway the motor utilizes to get around a blocked site and (ii) a millisecond temporal resolution is needed since a fast diffusional pathway might be utilized. Consequently, this involves the labeling of kinesin-1 motors with AuNP probes and imaging with the parabolic prism-type TIR microscope in conjunction with a fast CMOS camera.

3. Motility of kinesin-1 motors in the presence of roadblocks

As outlined in the introduction, kinesin-1 motor proteins *in-vivo* frequently encounter roadblocks bound to the MT lattice. The aim of this chapter is to quantify to which extent the motility of kinesin-1 changes in response to the roadblock density on the MT lattice. To answer this question, kinesin-1 rigor mutants, incapable of binding ATP, are introduced into a stepping motility assay. Such mutants bind irreversibly to the binding site of kinesin-1 on the MT lattice and therefore constitute an ideal model to study the scenario of roadblocks encountering permanent roadblocks under the controlled *in-vitro* conditions of a SM stepping assay.

The first section of this chapter presents the genetic and mechanical properties of the kinesin-1 rigor mutant applied in this investigation. The second section then focuses on roadblock decoration of surface-immobilized MTs enabling a calibration curve to be obtained by directly measuring the density of GFP-labeled roadblocks on the MTs. The characterization and quantification of the kinesin-1 motility in the presence of different densities of unlabeled roadblocks is presented in the third section. In the fourth section, these results will be compared with a simulation that treats kinesin-1 as a Poisson stepper walking along PFs of restricted length.

3.1 A rigor mutant serves as permanent roadblock

In order to generate ideal roadblocks, the fact that a point mutation in the Walker A domain of kinesin-1 inhibits ATP binding, was utilized [42]. This mutation results in immobile motors which bind irreversibly to the MT lattice [16,43]. Here, two roadblock constructs were generated: Starting from a GFP-labeled and unlabeled kinesin-1 motor protein a single-point mutation was introduced to yield the GFP- and unlabeled roadblock, respectively (Fig. 15, rkin430eGFP and rkin430, see [28] and the Materials and methods chapter,

page 99). The proteins were expressed in *E. coli* and purified by affinity chromatography on Ni-NTA columns. These two roadblock proteins together with the GFP-motor constitute the set of tools needed to determine and quantify the effect of roadblocks on kinesin-1 motility.
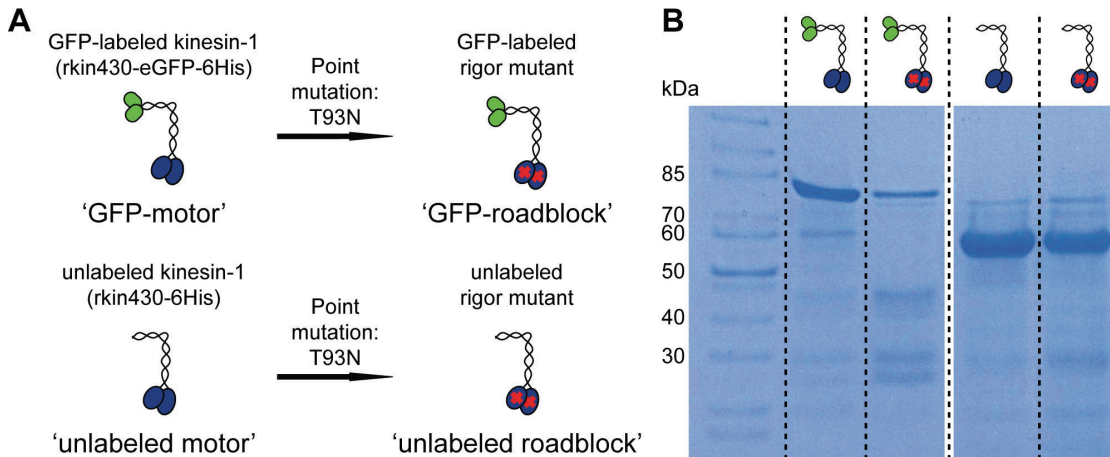

Fig. 15 | The GFP-labeled and unlabeled roadblock.
(A) The GFP-labeled and unlabeled kinesin-1 motor (left column) served as a template for a single-point mutation (T93N) that gave rise to a GFP-labeled and unlabeled kinesin-1 rigor mutant, termed 'GFP-roadblock' and 'unlabeled roadblock' (right column). (B) A SDS-gel showing the denatured protein monomers of the GFP-motor and -roadblock (first and second from left, both at 75 kDa), and the unlabeled motor and roadblock (third and fourth column, both at 55 kDa).

To investigate how single GFP-roadblocks interact with the MT lattice, SM experiments basing on the geometry of a stepping motility assay in conjunction with conventional objective-type TIRF microscopy were performed (see [60] for an excellent tutorial). The GFP-roadblocks were found to bind strongly to surface-immobilized MTs and no net movement was detected in presence of 1 mM ATP (Fig. 16A,B). Furthermore, it was found that the integrated fluorescence signal superimposed with the MTs showed a small numeric, however statistically insignificant decrease over a period of 20 minutes (Fig. 16C). This decrease allowed the estimation of the upper limit of the detachment rate, which was determined to 0.003 s^{-1} within the 95 % confidence interval. After active kinesin-1 motors were allowed to interact with decorated MTs at concentrations of 3 nM and 0.3 nM for 20 minutes, still

no significant decrease in fluorescence was observed. Thus, the roadblock can be regarded as irreversibly bound and kinesin-1 motor proteins are unable to kick-off the roadblocks from the MT lattice.
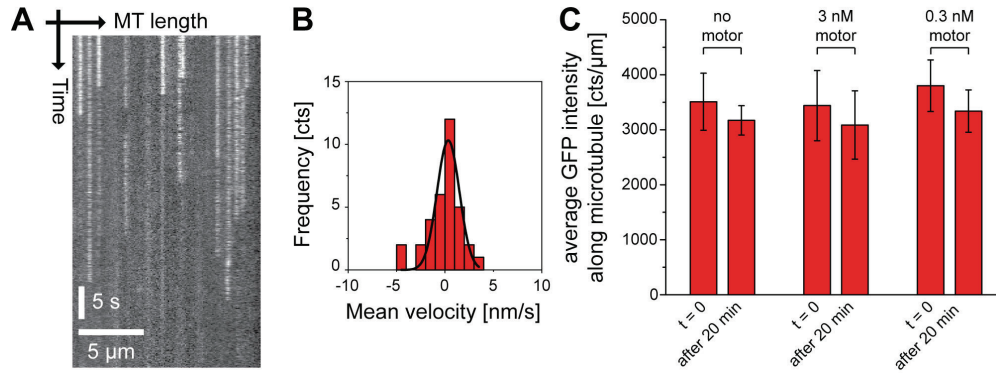

Fig. 16 | GFP-roadblocks are immobile and irreversibly bound on MTs.
(A) A kymograph representing the temporal development (vertical axis) of the fluorescence of individual GFP-roadblocks bound along the length of a 15 μm long MT (horizontal axis). Over a period of 50 seconds the GFP signal disappeared due to photobleaching. (B) The mean velocity of individual GFP-roadblocks was determined to 0.3 ± 1.2 nm/s (mean ± sd, $N = 34$). (C) Comparison of the integrated intensity of GFP-roadblocks bound along the MTs at the beginning of the experiment ($t = 0$) and after a waiting period of 20 minutes during which 0 nM (left), 3 nM (middle), and 0.3 nM (right) GFP-motors were allowed to interact with the decorated MTs. The GFP intensity was measured after washing the channel with fresh imaging solution, i.e. in absence of active GFP-motors. A single GFP-roadblock caused an average fluorescence signal of 650 counts per μm, which is in the range of the observed fluorescence drop (~ 400 counts per μm). Thus, on average less than 1 GFP-roadblock (400/650 = 0.6) detached from a one μm long MT during the waiting period.

3.2 Mean spacing of roadblocks on the microtubule lattice

The density of roadblocks bound to surface-immobilized MTs is an important parameter necessary to be controlled, since it gives rise to a mean spacing of roadblocks along the PFs. To estimate the correlation between density and mean spacing, a calibration curve was obtained relating the directly measured number of GFP-roadblocks per μm of MT to the concentration of GFP-roadblocks in the channel (Fig. 17, see the Materials and methods chapter, page 99).
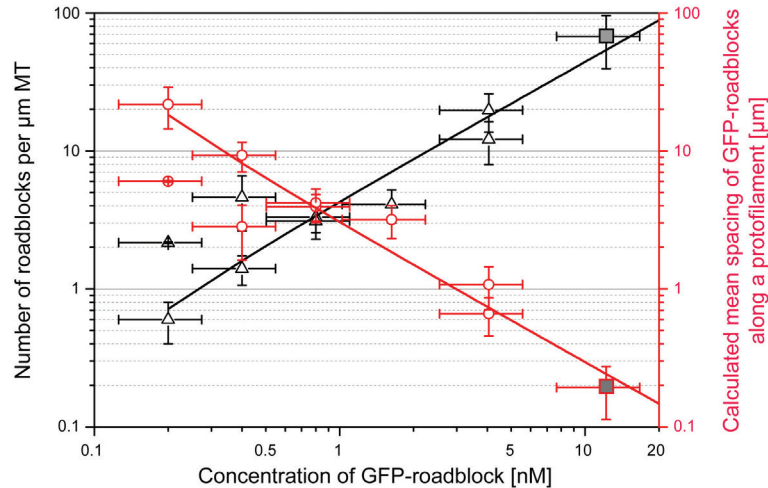
Fig. 17 | Density and mean spacing of GFP-roadblocks.
Surface-immobilized MTs were incubated for 1 minute with various concentrations of GFP-roadblocks ranging from 0.2 nM to 4 nM. The density of roadblocks per μm of MT (black triangles, left axis) depended linearly on the concentration of roadblocks in the channel. The data point for the highest concentration (grey square) was obtained by incubating three times longer (3 minutes) at 4 nM and was not included in the linear fit (black line). The mean spacing of GFP-roadblocks along a single PF (red circles, right axis) was calculated from the density assuming that all PFs of the 13-PF MTs are accessible. The data point at the highest concentration was again not included in the linear fit (red line).

The density of GFP-roadblocks on the MTs increased linearly from 0.6 up to more than 20 molecules per μm of MT for roadblock concentrations of 0.2 nM up to 4 nM, respectively. A line fit to the obtained roadblock densities yielded a relation of $4.4 \pm 0.6\ \mu m^{-1} \cdot nM^{-1}$ (roadblocks per μm of MT and nM of GFP-roadblocks), which enables the conversion of the concentration of roadblocks in the channel into a mean spacing along the PFs. Using the assumption that the MTs provided 13 available PFs the mean spacing of GFP-roadblocks was determined to 22 μm ($= 13/0.6\ \mu m^{-1}$) and 0.65 μm ($= 13/20\ \mu m^{-1}$) for roadblock concentrations of 0.2 and 4 nM, respectively. In turn, this calibration curve can now also be applied to calculate a certain roadblock concentration from a given mean spacing of roadblocks.

3.3 Deterioration of motor motility in presence of roadblocks

To determine how the motility of GFP-motors depends on the mean spacing of roadblocks on surface-immobilized MTs, a conventional stepping assay was performed in conjunction with objective-type TIRF microscopy, providing reasonable spatial resolution of approximately 30 nm and poor temporal resolution of 100 ms for the individual GFP-motors. To allow optimal image contrast of the individual GFP-motors, unlabeled roadblocks instead of GFP-labeled roadblocks were used in these experiments. The surface-immobilized MTs were pre-incubated with varying concentrations of unlabeled roadblocks, ranging from 0.75 nM up to 15 nM, for 1 minute (see the Materials and methods chapter, page 99). Subsequently, the GFP-motors were allowed to interact with such decorated MTs in presence of 1 mM ATP.

A clear effect of MT decoration on the movement of individual motors was observed in kymographs taken from the movie streams (Fig. 18A). In absence of roadblocks the majority of motors showed steady motion, whereas for increasing roadblock concentrations more motors showed jagged trajectories (see the five different event classes classified in Fig. 18B). At the highest roadblock concentration of 15 nM, motor movement was almost completely diminished. The mean velocity of a single motor (termed mean SM velocity) was obtained by fitting the time-displacement curve to a line and determining the slope. The run length and dwell time of a single motor (termed SM run length and SM dwell time, respectively) were directly determined from the total length and duration of the molecular trajectory. To identify the average run length (dwell time) of the motors, the distribution of SM run lengths (dwell times) was evaluated using cumulative probability distributions (CPDs) and subsequent fitting with a mono-exponential function. The CPD describes the fraction of SM run lengths (dwell times) being shorter than a given sample run length (dwell time) and was calculated similar to the method described in [110]. The advantage of CPDs over histograms is the avoidance of binning, which can affect the fitting results, particularly when the

data points within the single bins are not normally distributed, e.g. in the case of exponentially distributed data.
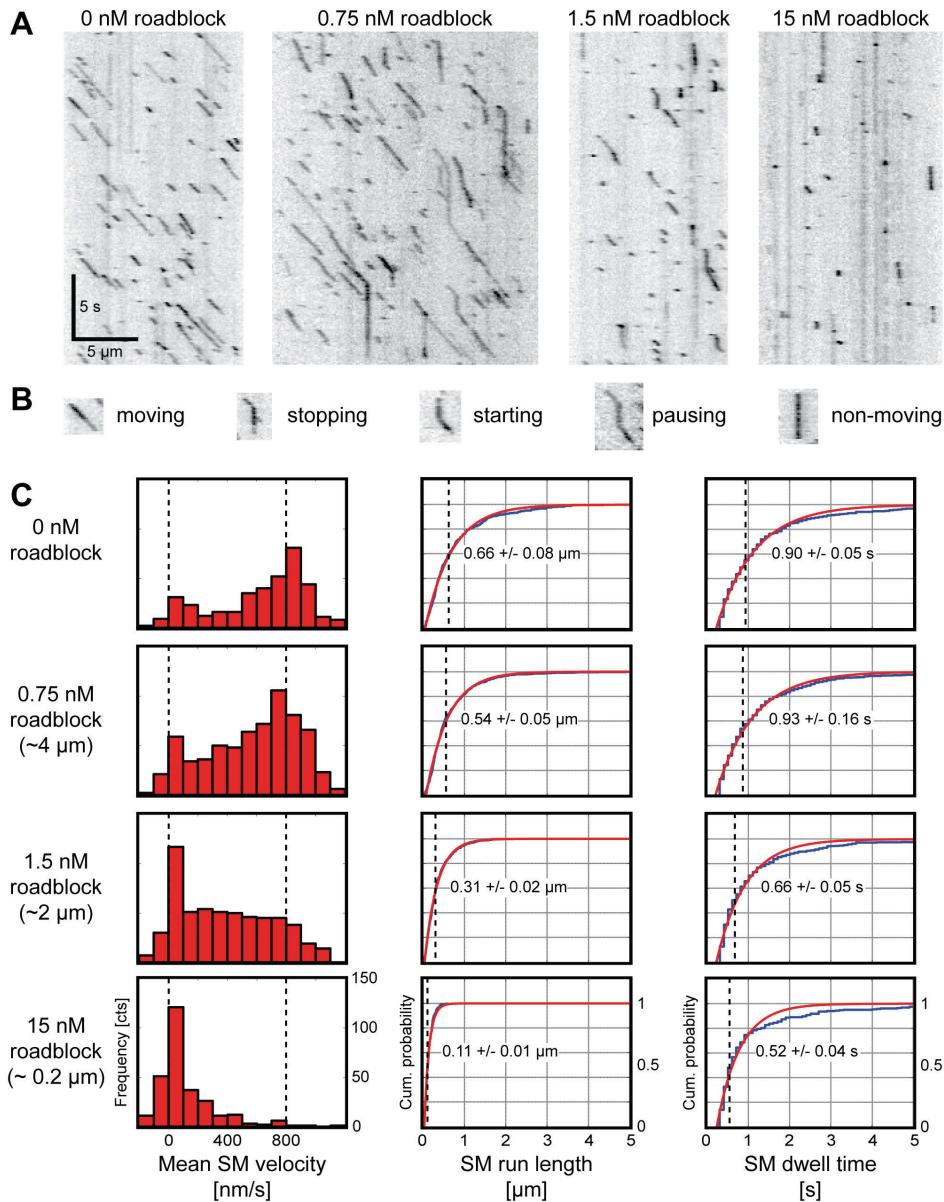
Fig. 18 | Deterioration of GFP-motor motility with increasing roadblock concentration.
(A) Kymographs showing individual GFP-motors at 1 mM ATP walking along MTs pre-incubated with 0, 0.75, 1.5, and 15 nM unlabeled roadblock. (B) Classification of the individual events present in the kymographs. (C) The distribution of the motility parameters in response to the conditions in (A). Histograms of the mean SM velocity (left), and CPDs of the SM run lengths (middle, mean ± fit error) and SM dwell times (right, mean ± fit error), for increasing roadblock concentrations (CPDs: raw data in blue, mono-exponential fit in red).

The histogram of the mean SM velocities showed a bimodal distribution, with a major peak at the transport velocity of 800 nm/s and a minor slow-velocity peak (Fig. 18C, dashed lines in left panel). The slow-velocity peak, accounting for approximately 20 % of the data points, was already present in absence of roadblocks and originates from (i) a fraction of dysfunctional motors that are still able to bind to the MT but cannot perform steps and (ii) the presence of intrinsic roadblocks such as the β-tubulin antibodies forming the anchor points of the MT to the surface. At the highest roadblock concentration no transport peak was observed, instead the majority of motors formed a slow-velocity peak with an average velocity of 100 nm/s. Negative velocities were caused by mislocalization due to the limited localization precision of about 30 nm, which becomes evident only for short traces (< 0.5 s) of non-moving molecules.

The run length was found to strongly depend on the concentration of roadblocks (6-fold decrease, from 0.66 μm to 0.11 μm, Fig. 18C, dashed lines in middle panel). This is evidence that the roadblocks in effect cause a reduction of the available free path along the PFs. Furthermore, the mono-exponential fit was in close agreement with the experimental data for all concentrations of roadblocks.

The average dwell time was determined similarly to the run lengths using CPDs and mono-exponential fitting and allows addressing the question of what happened when a motor encountered a roadblock. For example, if motors detach immediately upon encounter of the roadblock, the dwell time should decrease similar to the run length. In contrast, if motors are able to wait in front of a roadblock, the dwell time should either (i) decrease less strongly than the run length, (ii) remain constant, or (iii) even increase depending on whether the detachment rate in front of a roadblock is (i) enhanced, (ii) unchanged, or (iii) declined compared to unimpeded movement. Surprisingly it was found that the dwell time depended only mildly on the roadblock concentration (rather small decrease, from 0.9 s to 0.5 s, Fig. 18C, dashed lines in right panel). The mono-exponential fit was in agreement with

the experimental data for low concentrations of roadblocks whereas the occurrence of longer dwell times at higher roadblock concentrations was not correctly described. Longer dwell times are thought to originate from motors encountering several roadblocks one after another leading to a sequence of pausing events. The fact that the dwell time decreased less than the run length (twofold versus 6-fold) is evidence for a non-immediate detachment upon roadblock encounter but also for a detachment rate being somewhat enhanced in front of a roadblock. From the shortest dwell time an approximate pausing time of 0.5 seconds can be estimated, thus yielding an about twofold enhanced detachment rate (0.9 s ÷ 0.5 s) when the motor is dealing with a blocked site

In order to be able to predict the mean velocity, run length, and dwell time for certain roadblock concentrations in future experiments, their functional dependence on the roadblock concentration was investigated (Fig. 19). To compare mean velocities at different roadblock concentrations, an overall average of the mean SM velocities was calculated. It was found that the mean velocity, starting from 638 ± 58 nm/s (N = 382 molecules in 3 movies) in absence of roadblocks, decreased mono-exponentially with a decay constant of 3.1 ± 0.5 nM (mean ± sd, N = 6 data points, see Fig. 19A). The decay constant corresponds to the roadblock concentration, i.e. mean spacing, at which the motility parameter decreased to 37 % (1/e) and resembles a useful measure to compare the impact of roadblocks on the motility parameters. Given the experimentally determined calibration curve between roadblock concentration and number of roadblocks on the MT ($4.4 ± 0.6\ \mu m^{-1} \cdot nM^{-1}$, compare Fig. 17), this decay constant can be converted into a roadblock spacing of 1.0 ± 0.3 μm, which is close to the unimpeded run length of kinesin-1.

It is important to note, that the calibration curve was obtained for GFP-labeled roadblocks and may not appropriately describe the decoration with the unlabeled roadblock used here. However, the motility of GFP-motors in the presence of the formerly used GFP-labeled roadblocks was found to deteriorate similarly, i.e. a decay constant of 3.4 nM for the mean velocity was

found (data not shown), in close agreement with the decay constant for the unlabeled roadblock presented here. Thus, the different size and uncertainties in the protein concentration of both kinds of roadblocks contribute little to the determined decay constant.
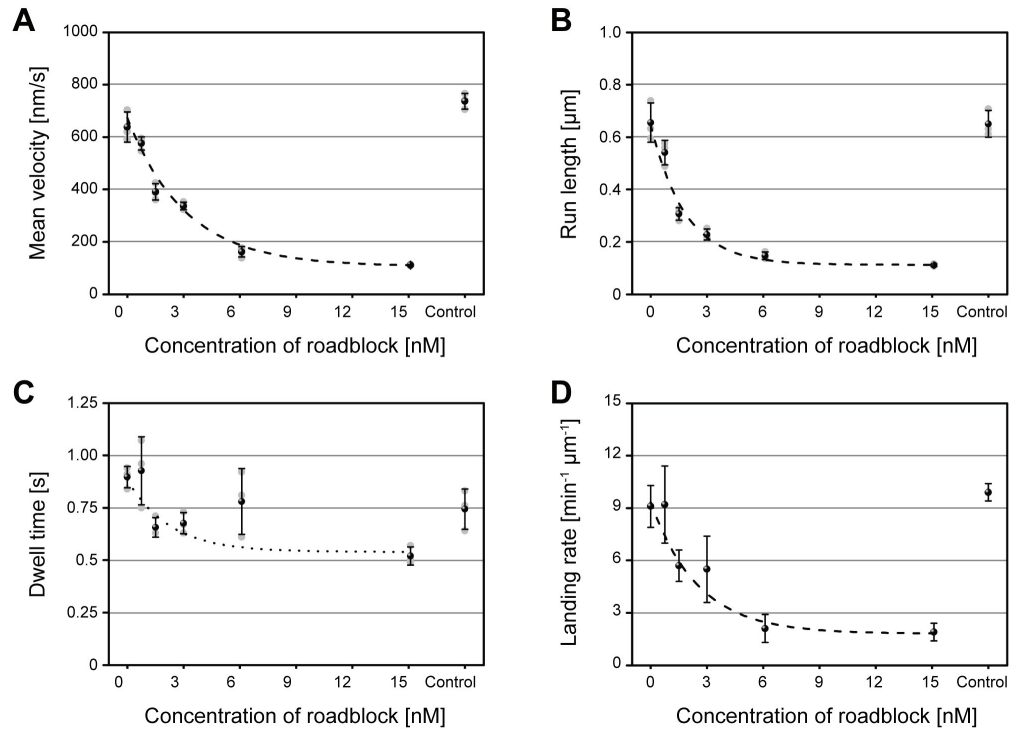
Fig. 19 | Mean velocity, run length, dwell time and landing rate exponentially decrease with roadblock concentration.
The mean velocity, run length, dwell time, and landing rate obtained at roadblock concentrations ranging from 0 nM to 15 nM were fitted to mono-exponentials. Control measurements (far right data point in each graph) were performed at the end of the experiment. Each data point (black dots) represents the mean ± sd of three individual movie streams (light grey dots). The decrease in mean velocity (A), run length (B), dwell time (C), and landing rate (D) were well described by mono-exponential fits (R^2 = 0.98, 0.95, 0.73, and 0.95, respectively).

The run length was found to deteriorate faster than the mean velocity with a decay constant of 1.8 ± 0.4 nM (mean ± sd, $N = 6$, Fig. 19B, equals a roadblock spacing of 1.6 ± 0.6 µm). Again, a similar decay constant of 1.7 nM was obtained for GFP-motors in presence of the formerly used GFP-roadblocks (data not shown).

In contrast, the dwell time was found to deteriorate less strongly than the run length with a decay constant of 2.2 ± 1.2 nM (mean ± sd, $N = 6$, equals a roadblock spacing of 1.3 ± 0.9 μm) and an offset dwell time of 0.5 s. Photobleaching caused the GFP molecules to bleach within 7.5 seconds, which leads to an underestimation of the dwell time by approximately 10 %. These results suggest that the process of waiting in front of a roadblock becomes the dominant motor behavior when the mean spacing is sufficiently small.

The landing rate was found to agree with a mono-exponential fit yielding a decay constant of 2.5 ± 0.7 nM (mean ± sd, $N = 6$, equals a roadblock spacing of 1.2 ± 0.5 μm). It was hypothesized earlier that the reduction in landing rate originates from the reduced availability of binding sites. However, alternative explanations such as (i) the electrostatic repulsion of unbound motors due to an increased decoration of the negatively charged MT with positively charged roadblocks as well as (ii) motors not being captured within a minimum of three frames (300 ms) are reasonable. It is interesting to note, that a roadblock spacing of 1.2 ± 0.5 μm corresponds to approximately 11 ± 5 roadblocks per μm of MT. Hence, only 1 % of the tubulin-dimers (11 roadblocks ÷ 1625 tubulin-dimers which make up a 1 μm long 13-PF MT) need to be occupied by roadblocks to deteriorate the motility to 1/e (37 %).

The mono-exponential fits of the four parameters discussed here yielded similar decay constants in the range of approximately 1 μm, which is a reasonable value, because it matches with the undisturbed kinesin-1 run length. Thus, when the roadblocks are distanced further apart, a mild effect on the motility is expected, because only few motors actually interact with the roadblock. In contrast, when the roadblocks are spaced closer together, more motors wait in front of roadblocks and hence the motility is strongly deteriorated.

3.4 Computer simulations of kinesin-1 motors in presence of roadblocks

To explain the functional dependence of the motility parameters on roadblock density, computer simulations were carried out taking four assumptions into account: (i) The kinesin-1 motor was modeled as an ideal Poisson stepper with an exponentially distributed off-rate (k_{off} = 1.1 s^{-1}, the inverse of the 0.9 second dwell time) and a velocity of 800 nm/s (both values were measured in absence of roadblocks in the previous section, compare Fig. 18C). (ii) Only a single PF rather than the three-dimensional, multi-lane structure of a MT was considered. Hence, the simulation ignored switching to another PF. (iii) As a roadblock permanently blocks the path of a motor, the free length of the PF was restricted to the mean spacing of roadblocks. (iv) When a motor encountered a roadblock it switched into a waiting phase with exponentially distributed waiting times with an average of 0.5 seconds. After the waiting phase, the motor ceased its run and detached from the PF. The process of overcoming roadblocks, which leads to a continuation of the run, was thus not included in this analysis. This appeared reasonable, since overcoming roadblocks was observed for a minority of only approximately 20 % of all motor events in this work and approximately 50 % in a previous investigation [67]. The large fraction in this publication can be explained by (i) a charge effect of their negative streptavidin roadblocks on the positive motors and (ii) their buffer conditions (BRB20 compared to BRB80 used herein, for buffers see Materials and Methods chapter, page 99). The simulation was then run for different mean roadblock spacings and the distributions of the motility parameters mean SM velocity, SM run length and SM dwell time were evaluated similar to the previous section (see the Materials and methods chapter, page 99). To allow for a comparison between the simulation and the experimental data, the mean roadblock spacing was converted back into concentration using the previously determined relationship (4.4 ± 0.6 µm^{-1}·nM^{-1}, compare Fig. 17)

Strikingly, the simulation reproduced the distribution of mean SM velocity, SM run length and SM dwell time in response to an increasing roadblock concentration. The simulation replicated the transition of the majority of the motors moving at 800 nm/s for a large roadblock spacing of 100 μm (equals a roadblock concentration of 0.03 nM) to the majority being stuck in the slow-velocity peak at a small roadblock spacing of 0.1 μm (equals a roadblock concentration of 30 nM, Fig. 20A, left panel). Only for extremely
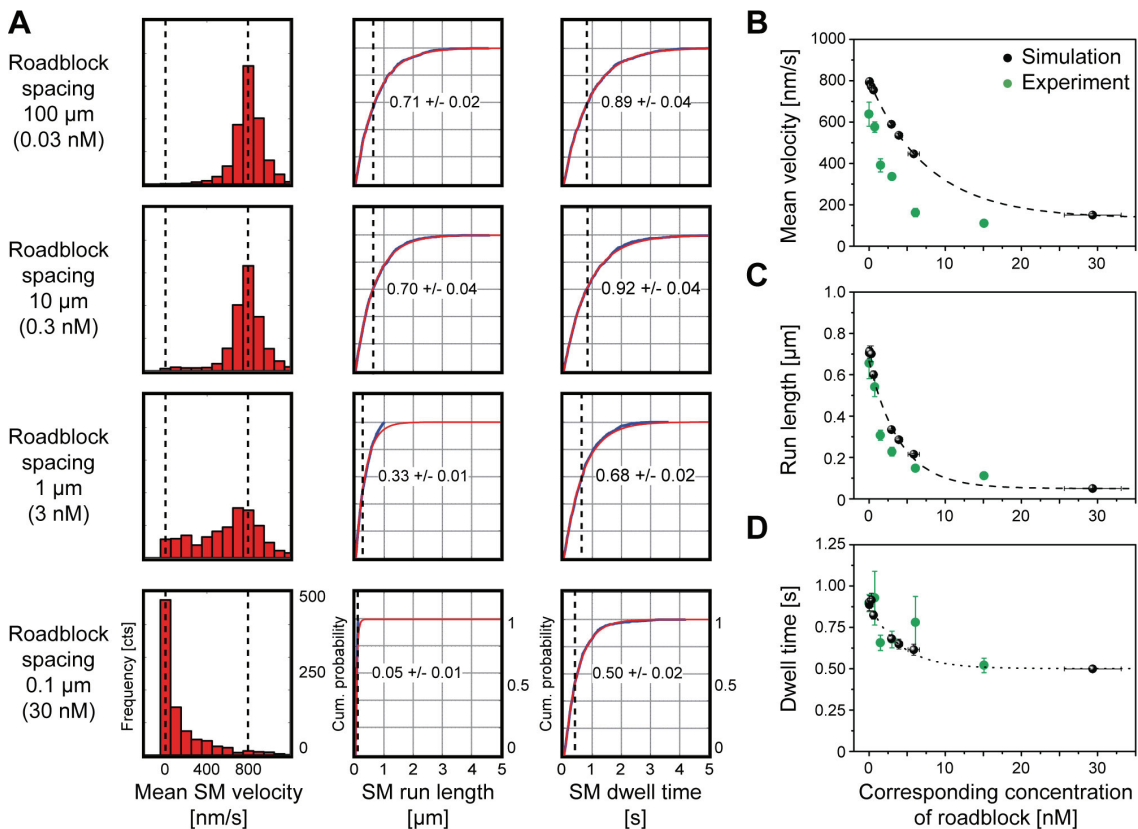
Fig. 20 | Mean velocity, run length, and dwell time exponentially decrease with increasing roadblock concentration in simulations of randomly stepping motors.

(A) Histograms of the mean SM velocity (left panel) and CPDs of the SM run lengths (middle panel) and dwell times (right panel) for increasing roadblock concentration (decreasing roadblock spacings) of 0.03 nM to 30 nM (100 μm to 0.1 μm, CPDs: raw data in blue, mono-exponential fit in red). The mean velocity (B), run length (C), and dwell time (D) were plotted against the corresponding roadblock concentration, which was derived from the roadblock spacing, and fitted to mono-exponentials (black dashed or dotted line R^2 = 0.99, 0.99, and 0.98, respectively). Each data point (black dots) represents the mean ± sd of three individual runs of the simulation for 1000 molecules each. The experimental results from the previous section (green dots) are displayed for comparison.

small roadblock separations of below 1 μm the histogram of the mean SM velocity smeared out and resulted in a large slow-velocity peak. This is because most motors encountered a roadblock and waited for the run to cease. As the mean SM velocity of the simulated molecules is always positive, a consequence of the unlimited localization precision in the simulation, the slow-velocity peak is not normally distributed. This fact biased the calculation of the mean velocity obtained from the simulations to show slightly larger values compared to the experiments (compare green and black dots in Fig. 20B). There, the mono-exponential fit for the simulated mean velocity yielded a 2.5-fold larger decay constant of 7.8 ± 0.2 nM (0.38 ± 0.06 μm) compared to the experiments (mean ± sd, $N = 8$ data points). This means, that the effect of roadblocks on the mean velocity was underestimated in the simulations compared to the experiments.

The run length showed a pronounced decrease from 700 nm for the largest roadblock spacing of 100 μm down to 50 nm for the smallest spacing (Fig. 20A, middle panel). It was found that the distribution of run lengths was exponential down to roadblock separations of approximately 1 μm. When the separation of roadblocks was shorter than that, the simulated run lengths deviated from the fit and were no longer described correctly. In fact, the run length was restricted to the maximum separation distance of the roadblocks, i.e. at a roadblock spacing of 1 μm the distribution of run lengths showed a clear cut-off at this value. Only a 2.2-fold larger decay constant of 4.0 ± 0.3 nM (0.74 ± 0.16 μm) was found compared to the experiments (mean ± sd, $N = 8$ data points, compare green and black dots, Fig. 20C). The effect of roadblocks on the run length of kinesin-1 motors was slightly underestimated. However, this result suggests that the assumption of randomly distributed roadblocks, giving rise to a shorter free path along a single PF, is appropriate.

In agreement with the experiments, the dwell time only mildly decreased from 0.9 seconds for large roadblock separations to 0.5 seconds for the smallest roadblock separation (Fig. 20A, right panel). This reflects the fact that for short roadblock spacings the majority of the motors encountered a

roadblock and waited on average 0.5 seconds before finally detaching. The dwell time showed a 1.6-fold larger decay constant of 3.9 ± 0.4 nM (0.76 ± 0.18 µm) compared to the experiments (black dots and dashed line in Fig. 20D).

Eventually, the simulation yielded results that agree qualitatively and quantitatively with the experimental data, in particular all three motility parameters decreased clearly mono-exponentially. The simulated decay constant deviated from the experimentally determined ones by approximately a factor of 2. This means, that the simulation underestimated the impact by which roadblocks influence the motility of kinesin-1 in experiments.

3.5 Discussion

This chapter focused on the influence of permanent roadblocks on the motility of kinesin-1 motor proteins. In order to tackle that problem, a kinesin-1 motor was genetically modified in a way that it was unable to bind ATP and hence unable to perform steps however still providing unaltered association to the MT lattice. This mutated motor, available as GFP-labeled and unlabeled protein, consequently served as an ideal roadblock to study the scenario of motors encountering permanently blocked sites in SM stepping assays utilizing conventional objective-type TIRF microscopy.

Testing the applicability of the rigor kinesin-1 mutants as permanent roadblocks revealed (i) immobile association with the MT in presence of ATP and (ii) irreversible binding, i.e. actively walking kinesin-1 motors were not able to remove roadblocks from the MT lattice, both in agreement with a previous study [16]. Thus, the rigor mutants provided ideal properties to influence the movement of kinesin-1 motors.

To allow conversion of the roadblock concentration used to decorate the surface-immobilized MTs into a mean spacing of roadblocks, a calibration curve was measured by directly counting the number of MT-bound GFP-labeled roadblocks (Fig. 17). This calibration curve yielded a linear relationship, which originates from the incubation period being too short

(60 seconds) to reach equilibrium. Consequently, the calibration curve allowed accessing information on the mean roadblock spacing along individual PFs, a parameter not being available in former roadblock studies [17,55,62,63,65-67].

The number of available PFs was expected to cause the largest impact on the calculated mean spacing of roadblocks. Whereas the total number of PFs of surface-bound MTs, was assumed to vary by 10 % (± 1 PF corresponds to 8 % variation), the number of actually accessible PFs is unknown, potentially leading to larger deviations. The accessibility of single PFs can be diminished due to the MTs being anchored to the surface via several anti-β-tubulin antibodies having a size between 5 to 10 nm [111]. Thus, the PFs used for anchoring the MT are located near the glass surface and might not be fully approachable for motors and roadblocks, respectively. Moreover, since the antibodies bind to the β-tubulin subunit and therefore themselves resemble permanent intrinsic roadblocks, they were also expected to affect the motility of motor proteins. This explains why in absence of roadblocks, kinesin-1 showed occasional stopping, starting and pausing events.

The dependency of the SM motility parameters mean velocity, run length, dwell time and landing rate on roadblock density was determined using GFP-motors walking on MTs decorated with unlabeled roadblocks. It was found that an increasing roadblock density caused the motor proteins to (i) move with a slower mean velocity, (ii) cover a shorter distance on the MT, (iii) remain associated with the MT lattice for shorter but finite times, and (iv) associate with roadblock-decorated MTs with a smaller landing rate. These four findings agree qualitatively with three previous *in-vitro* studies [16,17,66]. However, four aspects obtained from the data presented here help particularly to firm the ground on which the current picture of kinesin-1 dealing with roadblocks is based:

a) No premature detachment: The finding that the mean velocity deteriorated upon roadblock addition is clear indication for the existence of waiting phases. These waiting phases were directly observed (Fig. 18A) and motors moved with their full velocity between pauses, both in agreement with

[16,17,67]. Thus, kinesin-1 does not detach immediately upon roadblock encounter but instead switches into a waiting phase when confronted with a roadblock.

b) Reduced run length: An up to 6-fold decrease in the length of the motor runs was observed upon roadblock addition. Decorating the MTs with up to 15 nM unlabeled roadblocks, yielded a mean roadblock spacing of 0.2 μm along a single PF. In such a path-restricted environment, the motors showed an average run length of approximately 0.1 μm, which is in close agreement with the simulation of randomly stepping motors (compare Fig. 20C). This is a new observation, which directly shows that the length of the motor runs is strongly reduced only when the spacing of roadblocks becomes much shorter than the unimpeded run length.

c) Extended waiting phases and enhanced detachment: The dwell time only decreased twofold from 0.9 seconds in absence of roadblocks to 0.5 seconds for the highest density of roadblocks. This is evidence for two facts: First, the detachment rate of 2 s^{-1} (1 ÷ 0.5 s) in front of a roadblock is finite, i.e. not approaching zero for larger roadblock densities, which is in contrast to Crevel et. al. [66]. Secondly, the detachment rate is enhanced approximately a factor of two (0.9 s ÷ 0.5 s) when the motor is stuck in front of a roadblock compared to the unimpeded movement. Enhanced detachment rates are in agreement with prior studies [16,66,67], however such extended waiting phases were only observed by [17,67]. Both findings clearly point toward kinesin-1 being able to exhibit extended waiting phases when confronted with a roadblock in contrast to earlier studies, which showed waiting times one or more orders of magnitude shorter [16,66].

d) Reduced landing rate: The landing rate was found to deteriorate with a decay constant of 2.5 ± 0.7 nM (1.2 ± 0.5 μm), comparable to the other motility parameters. This is a surprising finding, because a decoration of only 1 % of the tubulin dimers, which follows from a roadblock spacing of 1.2 ± 0.5 μm, suffices to deteriorate the landing rate to 37 % (1/e). This fact provides clear evidence that the limited availability of binding sites is only a

minor determinant for the reduced landing rate, which conflicts with the hypotheses in previous publications [12,16,55,62,65]. Instead, reduced landing may originate from a charge effect, due to the increased decoration of the negatively charged MTs with positively charged roadblock molecules [112]. This appears reasonable, since saturation of the MT lattice with kinesin-1 molecules is achieved only when incubated with 100- to 1000-fold larger concentrations [16,112,113].

It can be concluded, that kinesin-1 can sensitively screen the crowdedness on the MT lattice, a fact that was speculated to exist also *in-vivo*. For example, the neuronal MAP tau clearly mediated the reduction of the landing rate for both individual motors [55] and vesicles or beads transported by multi-motors [53,62], which led to the hypothesis that vesicular transport *in-vivo* might be regulated differentially depending on the kind of MAP [12,114]. The high sensitivity of kinesin-1 toward the crowdedness on the MT lattice resembles an advantageous property for chemical sensing applications in nanotechnology, medicine and diagnostics [115]. For medical applications for example, the velocity and extent of vesicular transport could be used as a reporter mechanism to access information on the presence of MAPs in neurodegenerative diseases, markedly before severe symptoms such as atrophy of brain matter and accumulation of protein aggregates have emerged.

In order to test whether the mean spacing of roadblocks alone can explain the qualitative as well as quantitative deterioration in the motility parameters, computer simulations were carried out, rendering the random stepping of kinesin-1 motors on individual PFs limited in length due to the presence of roadblocks. The new finding that all four motility parameters showed a mono-exponential decay enables an attractive approach to quantify the impact of different roadblocks on the motility of kinesin-1. Furthermore, comparing the simulated decay constants with the ones obtained from the experiments revealed that the roadblocks acted two times more efficient in the

experiments compared to the simulation, i.e. an approximately two times lower concentration of roadblocks was necessary to deteriorate the motility by 37 % (1/e). Thus, the distribution of roadblocks on the MT lattice as well as the mechanisms by which roadblocks interact with motor proteins must be reconsidered.

First, since the actual number of available PFs in the experiments is unknown, it is assumed that the PFs on the top half of the MT (faced toward the aqueous medium) are well accessible whereas the PFs on the bottom half of the MT show drastically reduced accessibility. In this case the GFP-roadblocks are randomly distributed on only 7 rather than 13 PFs, resulting in an approximately two times higher roadblock density and thus halved decay constants compared to a fully accessible MT.

Secondly, a discrepancy between simulation and experiment is the distribution of roadblock spacings. When roadblocks are distributed randomly on the MT surface, the resulting distribution of spacings is exponential (with a decay constant equal to the mean), i.e. shorter spacings appear more often than longer ones. The simulation however only considered a mean roadblock spacing, which still provides a helpful abstraction, expected to not contribute significantly to the simulated decay constants.

Thirdly, it is not known whether kinesin-1 motor proteins can pass each other on adjacent PFs. It was shown that under saturating conditions a single motor cross-linked two successive tubulin dimers along the same PF [113], i.e. saturation occurred at a 2:1 molar ratio of motor to polymerized tubulin. This is indication that individual motors indeed fit next to each other on adjacent PFs. However, if motility under these conditions is still provided can be doubted, since it was found that on highly loaded MTs, individual motors showed an extremely low processivity of only 2.5 successive steps [66]. Thus, a single roadblock might in principle block up to three PFs at once (1 bound + 2 adjacent PFs). This could explain the smaller decay constants observed in the experiments, because the roadblocks might affect motors

walking on an adjacent PF, in essence causing the roadblock density projected on a single PF to be higher than calculated.

Lastly, the fact that the process of roadblock circumvention was not considered in the simulation caused an underestimation of the run length and dwell time leading to a bias toward larger decay constants. However, since a fraction of only about 20 % of the kinesin-1 motors showed intermittent pausing, a large impact on the simulated decay constants is not expected.

The small deviation between simulation and experiment suggests that the roadblocks indeed bind randomly to the MT lattice. If for example, the roadblock would form clusters on the MT lattice (as indicated by Roos et. al. [116] but not observed here), the reduction in the mean free path is expected to be less drastic. Consequently, the deterioration of the motor motility would be expected to occur with markedly larger decay constants in the experiments than in the simulation. As this was not observed, a potential attractive interaction between kinesin-1 molecules, leading to such a clustering effect, is too small to contribute observably to the deterioration of motor motility.

So far, the observation of GFP-labeled kinesin-1 motors was performed by utilizing objective-type TIRF microscopy providing a low temporal resolution of 100 ms and a limited localization precision of only 30 nm. This low resolution, although providing SM sensitivity, generally prohibits (i) the observation of motors switching between individual PFs and (ii) the detection of individual 8 nm steps that make up that movement. Thus, in TIRF microscopy the individual motor proteins can be treated as uniformly moving motors (moving steadily by 800 nm per second) advancing on a 25 nm wide one-way MT road. For the investigation regarding the deterioration of the motility parameters in dependence on the mean spacing of roadblocks, TIRF microscopy still yielded valuable information. In contrast, whether roadblock circumvention involves (i) a side step to an adjacent PF or (ii) a diffusive process is not possible to be answered here and needs further investigation.

Thus, the following chapter turns toward the question of how the motor protein eventually overcomes a permanent roadblock by imaging single AuNP-motors dealing with roadblocks, notably utilizing the newly developed parabolic prism-type TIR microscope, providing nanometer precision and millisecond temporal resolution.

4. AuNP-loaded kinesin-1 motors overcoming permanent roadblocks

The previous chapter showed that the motility of kinesin-1 deteriorated with increasing roadblock density on the MT lattice. Left out in that investigation was a small but interesting class of events, which comprised of motors that continued their walk normally after having paused in front of the roadblock. The main goal of this chapter is to elucidate which pathway a single motor utilizes to get around a roadblock. Two hypotheses of roadblock circumvention are of particular interest: (i) a diffusion-based mechanism, i.e. detachment of the motor upon roadblock encounter followed by immediate re-attachment, and (ii) an active side step to a neighboring or more-distanced PF. Whereas the former hypothesis requires a high temporal resolution due to the fast molecular diffusion, the latter one necessitates nanometer-precise localization due to the PFs being separated by only 6 nm. Both requirements can be met by utilizing 40 nm streptavidin-coated AuNPs, which were loaded onto the GFP-tail of kinesin-1 motors via biotinylated GFP antibodies (Fig. 21, similar to the method utilized in Fig. 14, page 34). Consequently, parabolic prism-type TIR microscopy was performed using a fast CMOS camera for detection. This approach allowed the detection of fluorescent GFP-motors with a low temporal resolution of 100 ms as well as strongly scattering AuNP-motors with a high temporal resolution of 1 ms.

Of crucial importance for this investigation is the guarantee of controlled SM conditions. It is therefore necessary to prove for (i) AuNP transport being driven by individual motors, (ii) the large AuNP label having a negligible impact on the movement of individual motors, and (iii) AuNP- and GFP-motors being similarly affected by roadblocks. In order to perform these check-ups, the dwell time, run length and velocity of single AuNP-motors was measured in absence and presence of roadblocks and compared to the GFP-

motors, notably within the same experimental setup. The results of these experiments will be presented in the first two sections of this chapter.
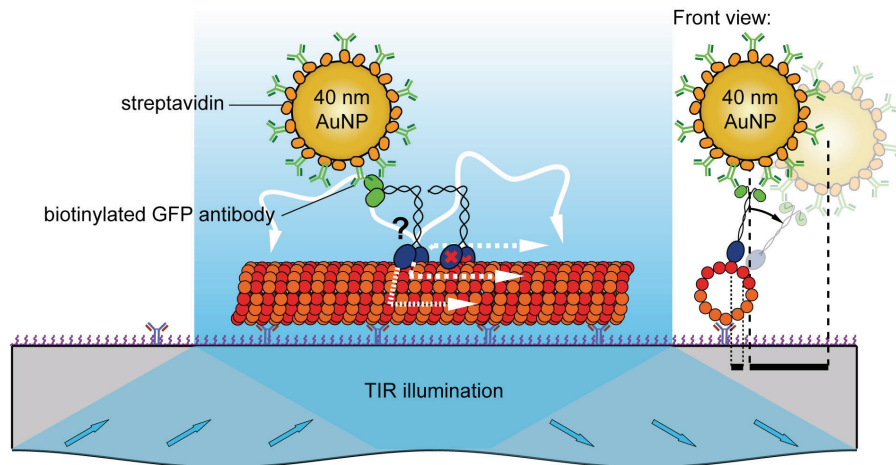

Fig. 21 | AuNP-loaded kinesin-1 stepping assay in presence of unlabeled roadblocks.
Surface-immobilized MTs were decorated with 2 and 4 nM unlabeled roadblocks. Individual AuNP-motors (GFP-motors, bound to GFP antibody-conjugated 40 nm streptavidin-coated AuNPs) were allowed to interact with decorated MTs in presence of 1 mM ATP. Different mechanisms by which a motor could potentially overcome a blocked site involve (i) detachment from the MT upon roadblock encounter followed by diffusional search and immediate re-attachment to another free PF in the forward or backward direction (solid zigzag arrows), (ii) side stepping to an adjacent PF (dashed arrow) or (iii) to a more distanced PF (dotted arrow) both, toward the left or right side. *Front view:* Switching to an adjacent PF requires the motor domain to move sideways by 6 nm (black bar between dotted lines). The accompanied side movement of the AuNP is amplified by the motor tail and the AuNP diameter (black bar between dashed lines).

In order to study how motors eventually overcome a permanently-blocked site on the MT, AuNP-motors were allowed to interact with roadblock-decorated MTs. Focusing on pausing events, which showed transitions between moving and pausing phases, enabled investigation of the sideways motion before, during and after the pause giving rise to the detection of side-shifts. These investigations, presented in the third section of this chapter, provide a detailed picture about the geometrical and mechanical properties of the circumvention mechanism kinesin-1 utilizes. Finally, in an attempt to

explain the observed distribution of side-shifts, a model treating the tail as a rigid linker is developed in the last section of this chapter.

4.1 Are AuNPs transported by single motors?

Of crucial interest in all SM studies is a prove for the observed events to be caused by individual molecules, especially when motors are attached to an artificial cargo such as AuNPs or tweezer beads [82,108,117]. In most cases, direct measurement of the number of motors attached to a cargo is not possible. Ways around that problem take the incubation stoichiometry of cargo and motor molecules into consideration or rely on the mere fact, that the motility parameters of the transported cargo are the same as for the single motor. The number of motor molecules bound to a cargo object was shown to follow Poisson statistics [118]. Thus, in an ideal case, a 10-to-1 incubation ratio of cargo to motor molecules provides 95 % certainty that the transported cargo is moved by a single motor. Using this argument as a starting point, several incubation ratios of AuNPs to GFP-motors were tested. Moving AuNPs were found only for incubation ratios of 5-to-1 and lower. Under these conditions, most GFP-motors were unbound, since they appeared with an about 100-fold higher frequency on the MT lattice than AuNP-motors. A 1-to-1 ratio of AuNPs to motors finally yielded a frequency of 5 AuNP-motors per minute per field of view, which was still 50-fold lower than the frequency of GFP-motors. The large number of unbound motors originates from the limited affinity of the GFP antibody to the GFP on the kinesin-1 tail, which has a dissociation constant in the 1 to 10 nM regime [119]. This is problematic because a similar range of concentrations was typically used for the GFP-motors in the incubation mixture. For the above conditions it was estimated[*] that only 10 % of the motors were bound to the AuNPs, which gives a 95 % certainty for single-motor transport of AuNPs.

A second argument for SM conditions was obtained by measuring the dwell time and run length of AuNP-motors. It was shown that the association

---

*Based on the assumption that the on-rate of a GFP- and AuNP-motors to the MT scales with the diffusion constant.

of more than one motor to either Quantum dots or DNA origami scaffolds caused both, the dwell time and run length to drastically increase by about 3-fold [65,120]. Evidence for SM movement is provided, if AuNP-motors show a similar dwell time and run length compared to single GFP-motors. However, the GFP label being subject to photobleaching, in contrast to the optically stable AuNP label, obscures this comparison. Therefore, a correction for the dwell time and run length was applied, which takes the bleaching time of 2.5 ± 1.0 s into account (mean $\pm$ sd, $N = 3$ movies, utilizing the parabolic prism-type TIR, compare Fig. 11, page 28, [67,104]). The motility parameters were compared using Welch's unpaired t-tests on a 99.5 % confidence interval.

The AuNP-motors showed on average a 1.4 times (0.5 seconds) longer dwell time and a 1.2 times (200 nm) longer run length compared to the single GFP-motors (Fig. 22A,B). Large dwell times of up to five seconds were only observed when incubating AuNPs with a 10-fold excess of motors (data not shown). Only then, AuNPs were transported along the complete length of the MT often only detaching when reaching the end of the MT.
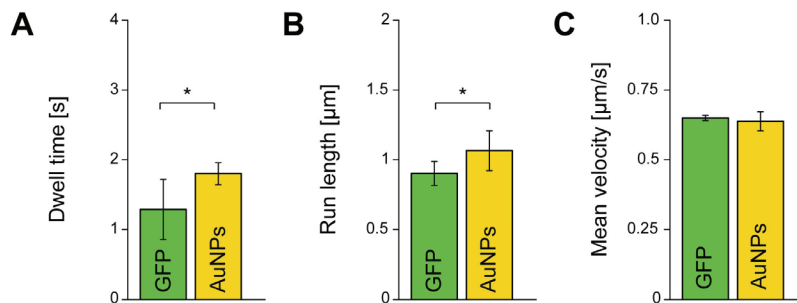
Fig. 22 | Comparing the motility parameters of single AuNP- and GFP-motors in absence of roadblocks.
(A) The bleaching-corrected dwell time of GFP-motors (green bar) was determined to 1.3 ± 0.4 s (mean $\pm$ sd, $N = 805$ molecules) and was significantly shorter (see asterisk, $p < 0.005$) than the dwell time of AuNP-motors (yellow bar) of 1.8 ± 0.2 s ($N = 63$ particles). (B) The bleaching-corrected run length of GFP-motors was determined to 0.90 ± 0.09 μm and was significantly shorter (see asterisk, $p < 0.005$) than the run length of AuNP-motors of 1.07 ± 0.14 μm. (C) The mean velocity of GFP-motors was determined to 650 ± 9 nm/s (mean $\pm$ sem) and was not significantly different ($p = 0.73$) from the mean velocity of AuNP-motors of 638 ± 34 nm/s.

The measured differences in dwell time and run length between AuNP- and GFP-motors are smaller than expected for multi-motor transport. Thus, it is concluded, that single motors transported the AuNPs. However, the difference for both parameters was found to be significant, even when taking into account the error of the bleaching time. This significance is thought to originate from the altered diffusion constant due to the large AuNP label which could enhance the rebinding probability of the motors to the MT. Interactions of the AuNPs with the surface could be ruled out as the origin of the higher dwell time and run length of the AuNP-motors, because the mean velocity of AuNP- and GFP-motors was found to be similar (Fig. 22C). Thus the drag force of a 40 nm AuNP is not sufficient to cause a significant slow-down of the motor.

A third argument for SM conditions involved the large size of the AuNP label, which allows approximately 25 antibodies to absorb on the particle surface, thus providing several binding sites for the motors. A single AuNP-motor could therefore pick up an additional GFP-motor, walking in close proximity. To reduce the probability of such pick-up events, a low total concentration of GFP-motors (150 to 250 pM) was used, which generated well-separated fluorescent motors on the MT lattice. An additional GFP-motor getting picked-up by the AuNP, is expected to exhibit a 3-fold enhanced dwell time and run length. As a consequence, AuNPs being transported by more than one motor have a higher probability of staying bound to the MT. This fact was considered in the evaluation by excluding those events whose attachment and detachment was not captured in the 10 seconds of the movie stream.

Controlled SM conditions of AuNP transport were achieved successfully and GFP- as well as AuNP-motors were shown to move with the same velocity. Thus, the large AuNP label does not influence the movement of single motors along MTs.

4.2 Do AuNP- and GFP-motors respond similarly to roadblocks?

Two approaches were of particular interest to prove for a similar behavior of AuNP-loaded and unloaded motors dealing with roadblocks. The first one involved comparison of the motility parameters of AuNP- and GFP-motors in presence of roadblocks (Fig. 23). The MTs were pre-incubated with 2 and 4 nM unlabeled roadblocks whereupon AuNP- and GFP-motors were allowed to walk along those MTs. Analogous to the previous section, the dwell time and run length were corrected for photobleaching in the case of the GFP-motors and compared to the AuNP-motors using Welch's unpaired t-tests on a 99.5 % confidence interval.
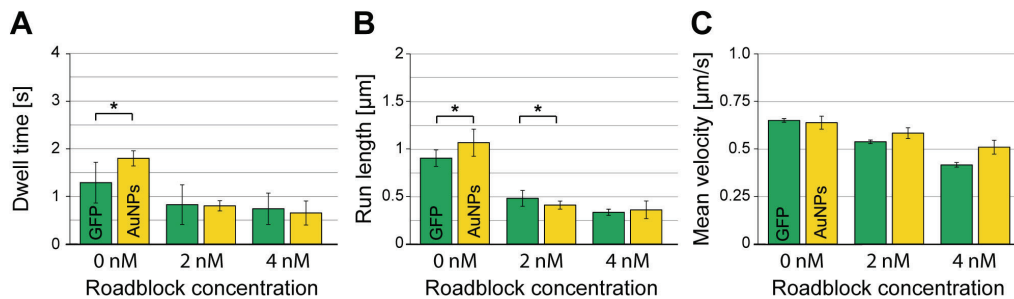

Fig. 23 | The motility parameters deteriorated equally for AuNP- and GFP-motors.
(A) The dwell time for GFP-motors deteriorated from 1.30 ± 0.40 s at 0 nM (mean ± sd, compare Fig. 22A) to 0.82 ± 0.42 s ($N_{GFP} = 985$ molecules) at 2 nM and 0.74 ± 0.33 s ($N_{GFP} = 649$) at 4 nM roadblocks and was not found to differ significantly from the dwell time of AuNP-motors ($p = 0.24$ and $p = 0.01$, respectively). (B) The run length for GFP-motors deteriorated from 0.90 ± 0.09 μm at 0 nM (compare Fig. 22B) to 0.48 ± 0.08 s at 2 nM and 0.33 ± 0.03 s at 4 nM roadblocks and was only found to differ significantly from the run length of the AuNP-motors in the 2 nM condition (see asterisk, $p = 0.03$ and, $p < 0.005$ respectively). (C) The mean velocity of GFP-motors deteriorated from 650 ± 9 nm/s at 0 nM (mean ± sem, compare Fig. 22C) to 537 ± 10 nm/s at 2 nM and 416 ± 12 nm/s at 4 nM and was not found to differ from the mean velocity of AuNP-motors (p = 0.14 and p = 0.02, respectively).

Upon addition of roadblocks the dwell time of the AuNP-motors showed the expected deterioration and did not differ significantly from the dwell time of GFP-motors. A stronger deterioration was observed for the run length, which is in agreement to the experiments presented in chapter 3. In presence of roadblocks, the difference in both dwell time and run length

between AuNP- and GFP-motors became statistically less pronounced compared to the 0 nM roadblock condition. The reason for this might be the reduced impact of the bleaching-correction on the determination of dwell time and run length.

The mean velocity for AuNP- and GFP-motors deteriorated not as pronounced compared to earlier experiments (compare chapter 3), however no statistically significant difference between the two was observed. The mean velocity of AuNP-motors was always higher compared to the GFP-motors, which originates from the fact that some non-moving AuNPs were excluded from the evaluation, when their attachment or detachment was not recorded within the movie stream. For the GFP-motors, no such sorting was applied because the movie stream was typically five to ten times longer (50 to 100 seconds), which renders the number of molecules present in the last frame of the stream to be negligible compared to the total number of events. Thus, the mean velocity of GFP-motors was affected by the presence of dysfunctional, non-moving GFP-motors and GFP-motors, which showed extraordinary long pausing times.

The deterioration of the motility parameters obtained for 2 and 4 nM roadblocks are in agreement with the previously obtained results, given the errors in determining the decay constants (compare Fig. 19). For example, the dwell time for the AuNPs is described well by the decay constant of 2.2 ± 1.2 nM and a waiting time of 0.5 seconds obtained for GFP-motors in chapter 3. For the run length and the mean velocity, a stronger deterioration was expected, however an overestimation of the roadblock density in the 4 nM case by only 30 % explains the observed difference. Thus it is concluded, that the AuNP- and GFP-motors responded similarly to roadblocks on the MT lattice.

A second approach for showing that AuNP- and GFP-motors responded similarly to roadblocks on the MTs involved comparison of the probabilities of

a steadily moving or stop-and-go (stopping, starting, pausing) event[*] to occur. Therefore, the AuNP- and GFP-motor events were classified into moving, stop-and-go, and non-classified groups, the latter containing trajectories, which were too short to allow event discrimination. In absence of roadblocks 52 % (51 %) of the GFP-motor (AuNP-motor) events were classified into the moving category (Fig. 24, left pair of bars). Upon addition of 4 nM roadblocks, this
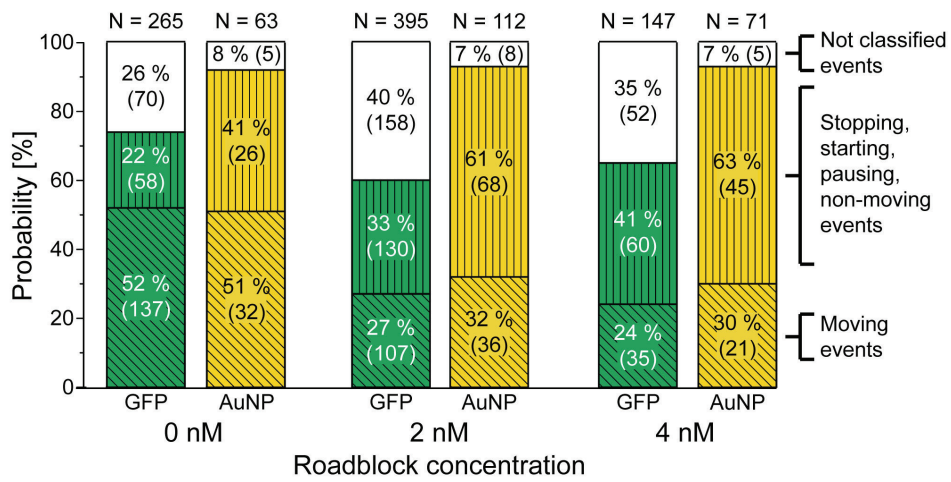

Fig. 24 | Event probabilities for GFP- and AuNP-motors at 0 nM, 2 nM, and 4 nM roadblocks.
The events for GFP- (green) and AuNP-motors (yellow) were sorted into three classes containing (i) steadily moving (diagonally lined area), (ii) stop-and-go (stopping, starting, pausing and non-moving, vertically lined area), and (iii) not classified events (white area). The event probability (in %) and the number of events (in brackets) are given in each block.

fraction was diminished to 24 % (30 %, Fig. 24, right pair of bars). In contrast, the probability of stop-and-go events was amplified from 22 % (41 %) in absence of roadblocks up to 41 % (63 %) at 4 nM roadblocks. A marked difference was observed for the probability of unclassified events, which contributed between 26 % to 40 % for the GFP-motors, but only 7 % to 8 % for

---

[*] A GFP-motor was termed 'event', when the molecule was visible in a minimum of four successive frames (400 ms), and the shortest 'pause' that could be reliably detected was two frames (200 ms). In contrast, a AuNP-motor was termed 'event', when the particle was visible in a minimum of 10 frames (only 10 ms) and periods during which the motor halted for longer than 50 frames (50 ms) were termed 'pause'. This definition was chosen, because the probability of a Poisson stepper at 100 8-nm steps per second to show a 50 ms pause is less than 1 %.

the AuNP-motors. This is due to differences in the event discrimination, which arose from the unequal acquisition times of 100 ms and 1 ms, for the GFP- and AuNP label, respectively. Furthermore, because pauses shorter than 200 ms were not possible to be identified for the GFP-motors, their classification into the moving class was favored.

Pre-incubation with 2 and 4 nM roadblocks caused a similar trend in the event probability for both, GFP- and AuNP-motors. The majority of GFP- and AuNP events moved steadily along the MTs in absence of roadblocks, whereas the major fractions in presence of roadblocks comprised of stop-and-go events. This is evidence for the motility of AuNP- and GFP-motors being affected similarly by the presence of roadblocks. However, compared to the GFP-motors, AuNP-motors showed a larger probability for stop-and-go behavior. One reason for this observation could be that the AuNP label exhibits undesired interactions with the MT lattice or the glass substrate, which may cause the motor to arrest shortly. However, two arguments speak against this hypothesis. First, within small errors it was proven that, in absence of roadblocks, AuNP-motors move with the same mean velocity compared to GFP-motors (compare Fig. 22), ruling out possible surface interactions. Secondly the run length and dwell time of the AuNP-motors were in agreement with the ones for GFP-motors in presence of 2 and 4 nM roadblocks. Therefore, a large probability for short stop-and-go movement might as well be present for GFP-motors, however due to the 100-fold longer acquisition time, their detection and classification is not possible. Hence, it can be speculated that GFP- and AuNP-motors in fact show similar probabilities for moving and stop-and-go behavior.

To get a better understanding of how the presence of roadblocks affects the stepping mechanism of a single motor, the event probabilities for the AuNP-motors were further analyzed. By summing up the run lengths of the AuNP-motors at each roadblock condition, the total number of performed steps was obtained, hence enabling the calculation of the probability per 8-nm step for detaching, pausing, stopping, and starting (Table 3). Furthermore, two

additional event groups of AuNP-motors were also detected: (i) immediate jumps (sudden forward or backward movements parallel to the MT by more than ± 25 nm) and (ii) sudden changes in the distance perpendicular to the MT, termed 'side-shifts' furtheron, both without prior pausing. The probabilities per step of these two event groups were also included in the table (for definition see the Appendix chapter A.7, page 117).

Table 3 | Comparing the event probabilities per 8-nm step for AuNP-motors at each roadblock condition.

Roadblock condition:	Probability [%][a]:					
	Detach	Pause	Stop	Start	Jumps w/o pause	Side-shifts w/o pause
0 nM[b]	0.73	0.33	0.10	0.03	0.18	0.18
2 nM[c]	1.36	0.88	0.72	0.17	0.52	0.16
4 nM[d]	1.16	1.08	0.67	0.13	0.43	0.13

[a]Probability calculated based on the total run length divided by the step size of 8 nm.
[b]Total run length: 69.289 μm (8.661 steps), N = 63 AuNP events
[c]65.749 μm (8.219), N = 112
[d]48.788 μm (6.099), N = 71

At the 0 nM condition, the AuNP-motor showed a detachment probability of 0.73 % per step, which corresponds to 137 steps before dissociating from the MT lattice. Moreover, a low probability for pausing, stopping, and starting was found. Jumps along the MT path and side-shifts occurred rarely. Upon addition of roadblocks, this pattern changed causing the probabilities to be increased by 2- to 7-fold. A remarkable observation is that jumps along the MT path without prior pausing occurred more often in presence of roadblocks pointing toward the mechanism of circumventing blocked sites by detachment and immediate re-attachment upon roadblock encounter. Side-shifts without prior pausing appeared to be independent of roadblocks. Thus, the PF tracking of kinesin-1 is not ultimately strict. Given the approximately 0.2 % probability for a side-shift (see Table 3, right column), kinesin-1 switches PFs every 500 steps (4 μm). Consequently, in absence of

roadblocks, every fourth kinesin-1 motor, having a run length of 1 μm, should show a side-shift during the run (see Appendix chapter A.7, page 117).

Having established and characterized the motility of single AuNP-motors in presence of roadblocks yielded a detailed picture of the event probabilities per 8-nm step. When confronted with roadblocks, AuNP-motors showed 2- to 3-fold enhanced forward and backward jumps along the MT without prior pausing. However, AuNP-motors also responded to roadblocks with a 2- to 3-fold enhanced probability for pausing. The following section will therefore focus on such pausing AuNP-motors to answer the question by which mechanism the permanent roadblocks are circumvented after the pause.

4.3 Do AuNP-motors overcome roadblocks by side stepping?

To study the precise path that kinesin-1 motors utilize to circumvent a blocked site, pausing AuNP-motors were of particular interest. These events made up approximately 30 % of all AuNP events and were characterized by an initial steady movement, then switched into a pausing phase, eventually overcame the blocked site and continued the run normally. The trajectories of AuNP-motors were obtained using the FIESTA tracking software and were projected onto the MT centerline, yielding (i) the distance along the path for parallel and (ii) the side distance for perpendicular movement. From these trajectories, the difference in side distances just before and after the pause was compared.

To provide an overview, several examples of such pausing events collected at 2 nM roadblocks are depicted in Fig. 25. At this roadblock condition, 80 % of the pausing events showed a significant side-shift when switching back into the moving phase. One example AuNP event (see Fig. 25A) showed two pausing phases with subsequent side-shifts into the same direction. It is interesting to note that the size of the first shift is smaller than the second one, which could originate from the three-dimensional structure of the MT. Depending on where the side-shift occurs on the MT, the projected length of the tethered AuNP onto the substrate plane is different (compare Fig. 21, front view and Fig. 28). For example, when the AuNP-motor is located on a

lateral PF and performs a side step toward the top of the MT, only a small change in the side distance of the AuNP is observed. This is because the projection of the tethered AuNP is mildly affected. In contrast, when the AuNP-motor makes another step toward the top, as observed in Fig. 25A, the change of the AuNP projection is more pronounced, leading to a larger change in the side distance. The largest side-shifts are expected, when the AuNP-motor side steps between the two topmost PFs of the MT. This explains the observation of the bigger changes in the side distance present in the event displayed in Fig. 25B.

Furthermore, it was observed that the fluctuation in side distance before and after a side-shift changed (Fig. 25A,B). Assuming that the AuNP-motor in Fig. 25A indeed moved from a lateral PF toward the top of the MT, leads to the conclusion that the side distance fluctuation is minimal on lateral PFs and maximal on the topmost PFs. This observation suggests that the AuNP, being flexibly tethered to the motor tail, exhibits restricted diffusion when held close to the substrate-surface. Accordingly, when the motor is attached to a PF on the side of the MT, the tethered AuNP explores a spatially restricted volume bounded by the MT and the glass-substrate. In contrast, when the motor is attached to a PF on the top of the MT, the tethered AuNP can freely explore the volume around the MT without spatial constraints. This mechanism could explain the variation in the side distance fluctuation being observed (see also Fig. 27B and the Appendix chapter A.7, page 117).

It is remarkable that AuNP-motors also showed side-shifts without a significant change in the fluctuation (see event in Fig. 25C), which is an indication that its amplitude not solely reports on the AuNP position relative to the MT. Instead differences in the way the AuNP is bound to the GFP-tail could contribute to the observed side distance variations. For example, whether the AuNP is attached to only one GFP or both GFPs at the tail of the motor can have an influence on the stiffness and orientation of the tail-anchored AuNP.
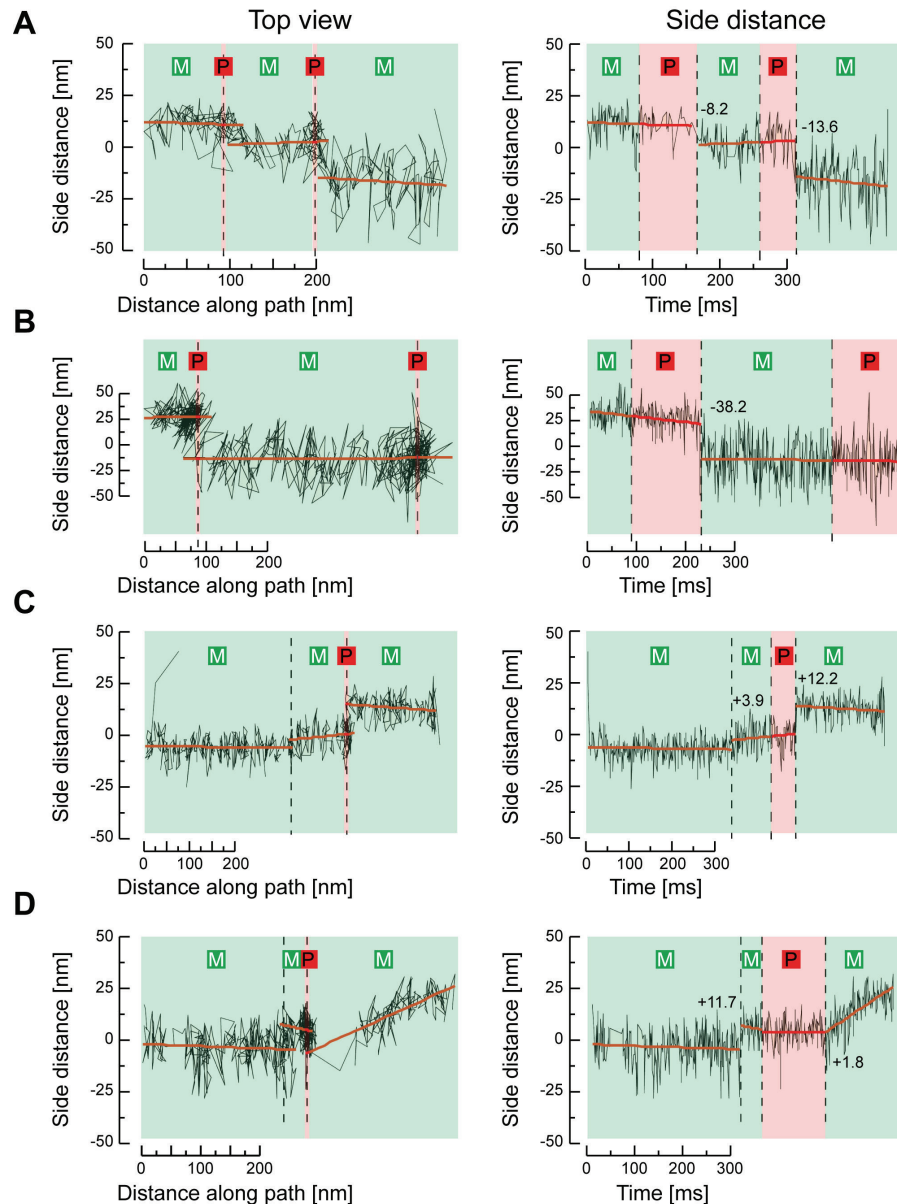
Fig. 25 | Examples of pausing events at 2 nM roadblocks.
The AuNP trajectories were inspected for moving (M) and pausing (P) phases. The vertically dashed lines depict transitions between either moving and pausing phases (A and B) and switching of PFs (C and D). The spatial and temporal development of the side distance (*y*-axis in all graphs) is plotted in the left and right column, respectively. The transition points (dashed lines) defined path and time segments, which were fitted to a linear function (red lines). If the side distance before and during the pause was not significantly different (~90 % of all cases), both segments were combined to one linear function. At the time point, where a transition from a pausing to a moving phase occurred, the difference of the thus obtained linear functions was calculated and gave rise to the size of a side-shift. A negative sign indicates a side-shift toward the left.

Finally, about 30 % of the AuNP events were able to overcome the blocked site by forward or backward jumps after having paused (see event in Fig. 25D). In this event, the roadblock was overcome by a sudden 80 nm forward jump, which only caused a small change in the side distance of + 1.8 nm. The direction of the movement (angle relative to the MT centerline) before and after the pause was clearly different. Such rare observations are thought to report on lattice defects, where the number of PFs and hence the MT supertwist changes locally. Consequently, AuNP-motors may also prove helpful for the investigation of changes in the PF number within the same MT.

Pausing events comparable to the ones exemplified in Fig. 25 were also obtained at 4 nM roadblocks as well as in absence of roadblocks. Also in these cases, the majority of the events showed a significant side-shift at the end of the pause (66 % at 4 nM and 61 % in absence of roadblocks). To quantify the sizes of the side-shifts, a total of 106 pausing events, obtained at the three roadblock conditions, were treated homogenously and pooled into one evaluation. The vast majority (90 %) of those events switched into the pausing phase without a significant change in the side distance (compare Fig. 25). This was indication for two aspects: (i) the motor indeed stopped because of a blocked binding site along the path. For example, if the motor would stop due to the AuNP interacting with the surface, a significant side movement or change in side distance fluctuation would be expected. (ii) The tethered AuNP adapts its equilibrium position faster than the 1 ms acquisition time. This also means that the equilibrium is reached between each step if the pauses between steps are longer than 1 ms. Consequently, if the AuNP were to be dragged behind the walking motor, one would expect a slow relaxation into the new position once the motor stopped. However, this process is expected to take place on a 10 to 100 µs timescale and is thus not observable here.

The 106 pausing events were summarized in a histogram to provide insight into the frequency and size of the side-shifts (top histogram in Fig. 26A). The histogram reveals, that smaller side-shifts occur more frequently than larger ones. Smaller side-shifts are thought to originate from AuNP-

motors walking on the lateral PFs of a MT, a result, which suggests that the majority of pausing events were caused on lateral PFs (compare front view in Fig. 21). Moreover, the histogram shows a rather large width, which is reasonable given the large number of possible PF transitions. For example, the topmost half of a MT provides approximately five pairs of adjacent PFs between which side steps could occur. However, when looking on top of the MT, each of these side steps would be differently sized due to the three-dimensional structure of the MT.

The majority of the side-shifts (90 %) showed sizes of ± 40 nm with the left and right direction occurring with almost equal frequency (45 % versus 55 %). Such a range of side-shift sizes can be explained assuming a rigid, extended 60 nm long linker between the motor domains and the center of the 40 nm AuNP (compare Fig. 28A). In fact, a linker length of 65 nm was obtained experimentally from a AuNP event, which moved from the far right to the far left side of a MT, thereby enabling direct measurement of the maximum projection of the AuNP reaching out from the MT surface (see Appendix chapter A.7, Supporting Fig. 9, page 121). The long, rigid linker could amplify the local distance between two neighboring PFs into a much larger distance due to a lever effect (compare front view in Fig. 21, and Fig. 28). By rule of proportion, the ratio of the 12.5 nm radius of the MT to the 6 nm distance between neighboring PFs should be similar to the ratio of the 77.5 nm distance of the AuNP from the MT center (65 nm linker + MT radius) to the largest detectable side step of 37.2 nm. It is argued, that the larger side-shifts originate from sideways transitions where several PFs were skipped at once, as observed in the AuNP event presented in Supporting Fig. 9, page 121. Therefore, it is assumed that the histogram mainly comprised side-shifts originating from transitions between adjacent PFs.

Insignificant side-shifts for which the error was larger than the actual shift size resemble a sharp peak located between ± 4 nm (second histogram from top in Fig. 26A). This is in agreement with the previously obtained

localization errors (3.8 nm, compare Fig. 13, page 33) obtained for AuNP-motors immobilized on surface-attached MTs.
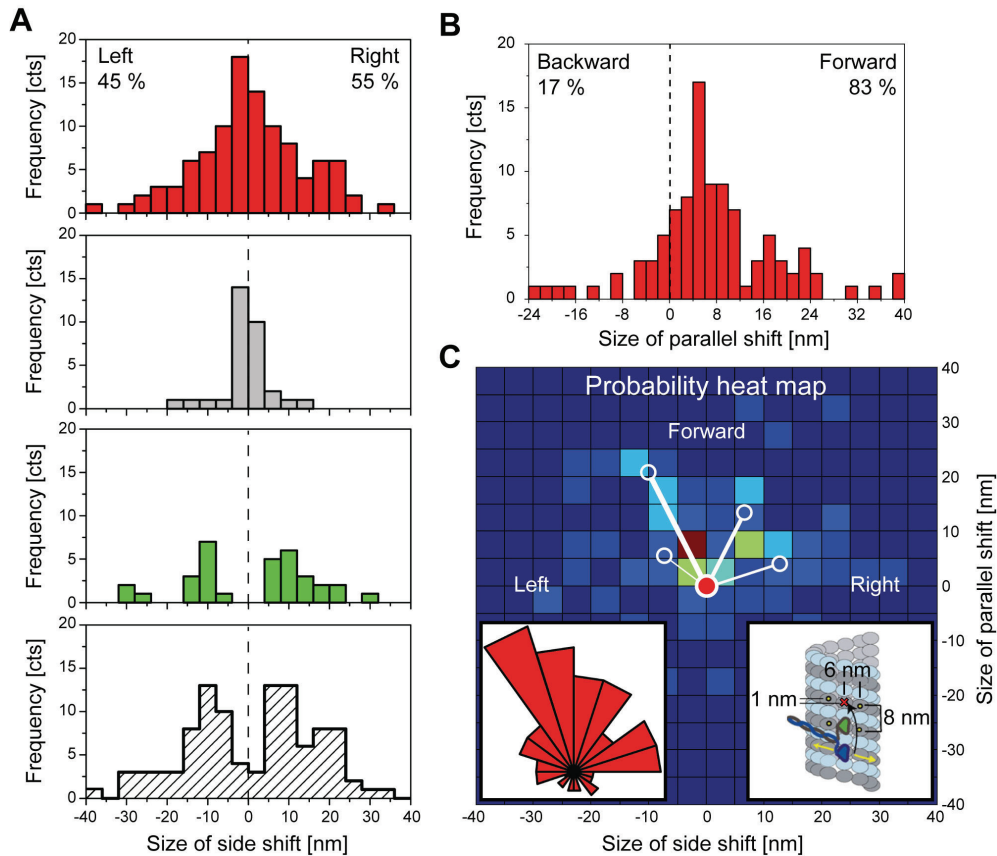

Fig. 26 | Size distribution of side and parallel shifts and accompanied direction of roadblock circumvention after a pause.
(A) The histogram of side-shifts detected from 106 pausing events (red bars) contained a number of insignificant side-shift (grey bars), for which the error was larger than the actual size of the side-shift. PF-switching events, which showed side-shifts without pausing (green bars), reproduced the initial distribution (top). The combination of the initial distribution with the side-shifts obtained from PF-switching events, ignoring the insignificant side-shift, resulted in the histogram of all significant side-shifts (dashed bars confined by black line). (B) Histogram of shifts detected parallel to the MT centerline during the transition from the pausing to the moving phase. The sizes of the parallel shifts were determined by averaging the distance along the MT 10 ms before and after the transition. (C) Two-dimensional probability heat map of the shifting pattern by combining the data from (A) and (B). From the blocked site (red dot), most circumvention moves occurred into the forward-left, forward-right, right and left direction (in order of frequency, indicated by solid white lines). Left inset: Radial histogram of shifting directions. Right inset: Top view onto a 13-PF MT showing four possible binding sites (yellow dots) for a kinesin-1 motor when the binding site lying ahead is blocked (red cross). Adapted from [38].

Since 25 % of the AuNP-motors showed sudden side movements without prior pausing, it was interesting to test, whether such PF-switching events showed similarly distributed side-shifts compared to pausing AuNP-motors (third histogram from top in Fig. 26A). This distribution was found to fit into the initial one obtained for the pausing events. Thus, it is concluded, that AuNP-motors utilize a similar pathway for side shifts, no matter if the path is blocked or not. Combining the side-shifts obtained from both, pausing and non-pausing events, thereby rejecting the insignificant side-shifts, resulted in a histogram of significant side-shifts (bottom histogram in Fig. 26A). This histogram revealed the existence of two frequent side-shifts (± 10 nm) to the left and right, and potentially less frequent side-shifts to ± 20 nm.

So far, the above analysis focused only on the magnitude of the side-shift. However, since the MT lattice resembles a two-dimensional environment for the motor, it is important to clarify, in which direction the AuNP-motor actually moves when overcoming a roadblock. Therefore, the shift parallel to the MT centerline was analyzed directly at the transition from the pausing to the moving phase. As the experiments were carried out at 1 mM ATP, the resolution of 8 nm steps, which take place on average every 10 ms (corresponds to 10 frames available for averaging), was not sufficient. However, information about the parallel (forward and backward) shift can be obtained by averaging the AuNP position 10 ms before and after the transition from the pausing to the moving phase. The majority of the thus extracted parallel shifts thereby showed a strong bias into the forward direction (83 %, Fig. 26B). Peaks at +16 nm and +24 nm appear in the histogram, which would be expected if the AuNP-motor would step 'over' the blocked site. However, the majority of parallel shifts showed sizes between −4 nm and +10 nm, possibly with a small contribution at +8 nm. No clear peak at 0 nm was detected, which proves the roadblock circumvention process of the AuNP-motor indeed being a two-dimensional process, having a non-zero component parallel to the MT centerline as well.

To gain insight into the direction of the roadblock circumvention move, the information on side- and parallel shifts were combined into a probability heat map (Fig. 26C). This map resembles a two-dimensional histogram color-coding for the number of circumvention moves performed toward a certain location around the blocked site. The warmer the color of the 10×10 nm^2 pixel, the higher was the frequency of such a move. The heat map clearly indicates that the circumvention move indeed involved a shift to the left and right (see bright-blue spots in Fig. 26C), which might point toward the existence of alternative 'hot spots' lying in the forward-left and -right direction. Taking into account the polar histogram of shift directions (left inset in Fig. 26C) revealed that the AuNP-motor additionally showed less frequent shifts into the strict right and even less likely into the strict left direction. Presumably, the distribution of shift directions is correlated to the distribution of available binding sites next to the blocked tubulin dimer (Fig. 26C, right inset). According to this schematic, alternative binding sites are indeed available in the forward-left and -right, as well as in strict right and left direction relative to the direction of motor movement.
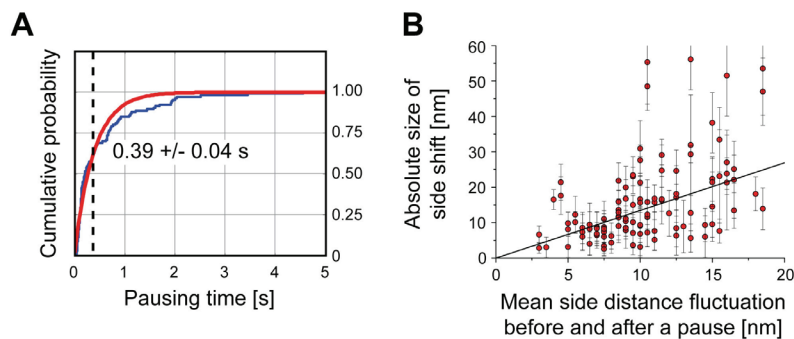

Fig. 27 | Pausing times and fluctuation of the side distance.
(A) CPD of pausing times (blue) with mono-exponential fit (red). (B) The side distance fluctuation was averaged before and after the pause and plotted against the absolute size of the side-shift. A linear regression yielded a coefficient of correlation of $R^2 = 0.13$.

To test, whether pausing in front of a roadblock is an intrinsic feature of the motor rather than being caused by variations in the experimental conditions, pausing times for each roadblock concentration were analyzed.

The distribution of pausing times was mono-exponential for the three roadblock concentrations tested and no significant difference in the characteristic pausing time was observed on a 95 % confidence interval ($p > 0.4$ in all three cases, data not shown). Thus, pooling the pausing events obtained at different roadblock densities into one data set was reasonable. The pausing times were therefore pooled into one CPD plot (Fig. 27A) and fitted with a mono-exponential function yielding a characteristic pausing time of 0.39 ± 0.04 s (mean ± sd, $N = 106$), which is in agreement with the previously determined pausing time for GFP-motors of 0.5 s (see previous chapter). Thus, the observed waiting times are independent of the kind of probe (GFP or AuNP) used to label the motor protein. Furthermore, since pausing AuNP-motors were also observed in the 0 nM roadblock condition, the pausing times might be independent of the kind of roadblock, as long as the roadblock is permanent. This is indication, that waiting is an intrinsic motor behavior in the sense that as long as the next tubulin dimer is blocked or made unavailable by a permanent molecule or local defect, the motor is able to wait for an extended period of time. Termination of the searching phase is presumably facilitated either by detachment of the trailing head or attachment of the leading head to an alternative binding site.

To investigate from where on the MT the differently sized side-shifts originated, the mean side distance fluctuation before and after a pause was determined. It was found that the absolute size of the side-shift was indeed correlated to the mean side distance fluctuation (Fig. 27B), which provides evidence that smaller side-shifts occurred on the lateral PFs of the MT, in agreement with the simple geometrical argument provided before (compare Fig. 21, front view and Fig. 28).

4.4 The kinesin-1 tail modeled as a rigid linker

To explain the distribution of side-shifts, a model was developed, which treated the tail of the motor protein as a rigid 65 nm long linker, oriented perpendicular to the surface of a 13-PF MT (Fig. 28A). Evidence for this
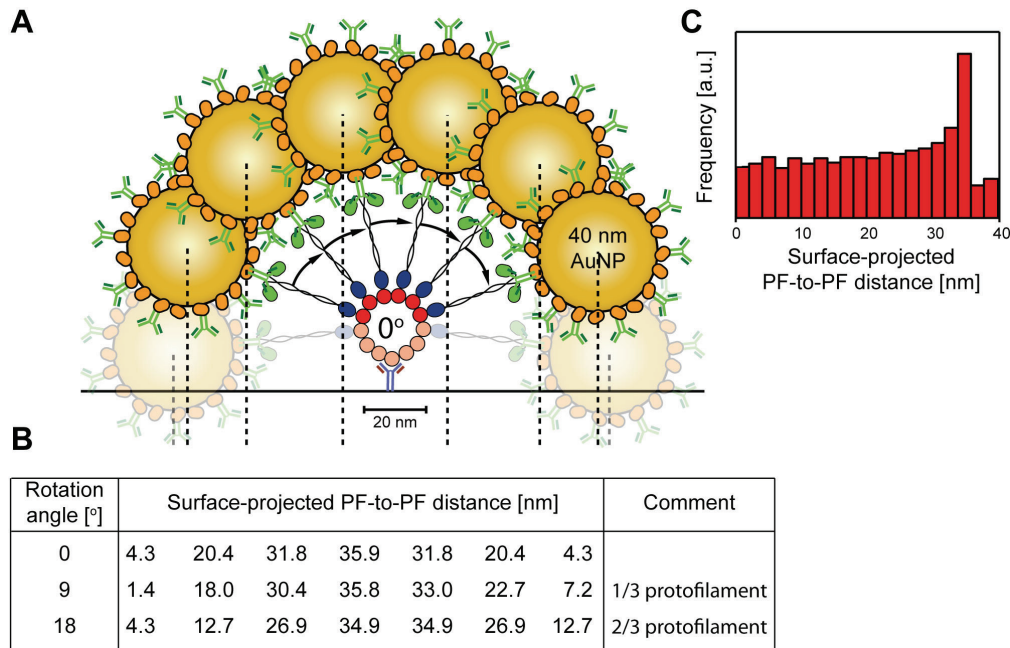
A

C

B

Rotation angle [°]	Surface-projected PF-to-PF distance [nm]						Comment
0	4.3	20.4	31.8	35.9	31.8	20.4	4.3	
9	1.4	18.0	30.4	35.8	33.0	22.7	7.2	1/3 protofilament
18	4.3	12.7	26.9	34.9	34.9	26.9	12.7	2/3 protofilament

Fig. 28 | A two-dimensional rigid linker model of AuNP-motors performing side steps between neighboring PFs.

(A) A surface-immobilized MT, anchored to the antibody with the lowest PF, provides six accessible (red circles) and seven inaccessible PFs (pale red circles). A AuNP-motor bound on a lateral PF is closer to or may interfere with the surface (bleached AuNP-motors), causing the diffusion of the AuNP to be spatially restricted. The projected length of a laterally positioned AuNP-motor changes only slightly as the motor performs a side step toward the top of the MT (see distance between the dashed lines). However, further side steps toward the top of the MT, cause stronger changes in the projected length. (B) The PF-to-PF distances were calculated based on a rigid 65 nm long linker and a 13-PF MT. The MT is rotated by 9° and 18° to consider various orientations relative to the surface. (C) Histogram of side-shifts obtained from the model in (A) by summing over all possible MT orientations. The side-shifts larger than 35 nm originate from transitions between further distanced PFs.

assumption to be reasonable came from a AuNP-motor, which moved from the far right to the far left side of a MT (see Appendix chapter A.7 and Supporting Fig. 9, page 121). This event revealed the linker to be in an extended, 65 nm long configuration when the motor was located on a lateral PF. In this model, it was assumed that the linker was also in the extended configuration when the motor was located on the topmost PF. Consequently, a side step to an adjacent PF is connected to a swing of the AuNP-linker by approximately 28° (360°/13 PFs). This causes the projected length of the AuNP linker onto the surface to be

different before and after each side step, generating a unique side-shift pattern for this MT orientation (0° in Fig. 28A). When the orientation of the MT is rotated by 9° and 18°, respectively, differently sized side-shifts occur (see table in Fig. 28B). The largest side-shift, in the range of ± 35 nm, occur on the topmost PFs. Larger side-shifts occurred due to several PFs being bridged at once, both in experiments and the model. However, a striking contradiction between experiment and model is the distribution of the side-shifts. The model clearly proposed a rather homogenous distribution, with the most frequent side-shift being the one, which occurs on top of the MT (Fig. 28C, see the peak at ~ 35 nm). This is in stark contrast to the experiments, which yielded smaller side-shifts of only ± 10 nm. Consequently, the model assumption of a rigid 65 nm linker might be too simplistic. A more elaborate model, taking into account the bending rigidity of the motor tail as well as the excluded volume occupied by the MT and the glass substrate needs to be developed in the future, in order to explain the distribution of side-shifts.

4.5 Discussion

The results presented in this chapter provide insight into the mechanism by which kinesin-1 circumvents permanent roadblocks. This process was studied with nanometer-precision by AuNP-labeling of individual kinesin-1 motor proteins dealing with permanent roadblocks. Imaging was carried out utilizing the newly developed parabolic prism-type TIR microscope, which allowed the imaging of AuNP-motors with 1 ms temporal resolution. Automated particle tracking using the FIESTA software enabled the investigation of pausing AuNP-motors showing side-shifts when overcoming a permanent roadblock.

To guarantee controlled SM conditions a combination of measures were applied, taking into account (i) the incubation ratio of AuNPs and GFP-motors, and (ii) the landing rate and density of those motors on MTs. These arguments allowed estimating the number of AuNP-bound and free GFP-motors in the experiment, which yielded a fraction of only 10 % of the motors being bound

to the AuNPs. Thus, applying Poisson statistics, a moving AuNP-motor was transported by a single motor with 95 % certainty.

AuNP- and GFP-motors were similarly affected by roadblocks, which was inferred from the comparison of their motility parameters at different roadblock conditions. This comparison revealed that the motility parameters of AuNP- and GFP-motors deteriorated similarly, which is evidence that the AuNP does not influence kinesin-1's ability to circumvent roadblocks. Moreover, this fact provided further evidence that single motors transported the AuNP, unlike in previous roadblock studies, where labeling with Quantum dots caused the kinesin-1 motors to aggregate on the cargo [65].

The finding that an increasing roadblock density caused both, the AuNP- and GFP-motors to show a lower (higher) probability for steady (stop-and-go) movement was in agreement with previous experiments (see chapter 3 in this work and [16,17]). In absence of roadblocks, AuNP-motors showed few stop-and-go events and immediate jumps along the MT, however, upon roadblock addition, the probabilities for both event groups were enhanced, i.e. the probability for jumping was increased 2- to 3-fold. This is clear indication that roadblocks can be circumvented by detachment followed by immediate re-binding.

Side-shifts without prior pausing were observed in 25 % of the AuNP-motor events, which resembles a new, surprising finding, allowing the estimation of the side step probability to 0.2 % per forward step. Thus, the PF tracking mechanism of kinesin-1 is not ultimately strict, causing the molecule to switch transport lanes every 500 forward steps (4 µm). Recently, somewhat surprising results were obtained for kip3 (a kinesin-8 family member) from gliding motility assays, which add a new aspect onto the ongoing discussion of processive motors performing side steps [68]. There, short-pitch rotations of Quantum dot-labeled 14-PF MTs being propelled by surface-immobilized kip3 motors were detected by fluorescence interference contrast (FLIC) microscopy. The kip3 motor, having a three amino acid longer neck-linker than kinesin-1, showed a pronounced tendency of stepping toward the left as inferred from

rotational pitches of approximately 1 µm, which corresponds to approximately one side step to the left per ten forward steps (side step probability ~ 10 % per forward step). This is in stark contrast to kinesin-1 driven MT rotations, which yielded rotational pitches of 8 µm [34], corresponding to the apparent supertwist of 14-PF MTs. Consequently, the PF-tracking ability of the kip3 motor is distinctly different from kinesin-1 since it exhibits a 50-fold higher probability of side stepping.

The finding that kinesin-1 showed equal probability of moving to the left and right is in agreement with the observed rotations of 8 µm. Furthermore, the estimated 0.2 % probability of side stepping would translate into a standard deviation of the rotational pitch of approximately ± 1.2 µm (± 2 side steps within the 8 µm supertwist), which is in agreement with a measured value of 1.37 µm by Nitzsche et. al. [34]. Thus, the rotational pitch is expected to deviate from the intrinsic 14-PF MT supertwist only when the rates for stepping to the left and right are markedly different as in the case of kip3.

Pausing AuNP-motors, which switched back and forth between a steadily moving and a pausing phase, were observed in 30 % of all AuNP events. These events enabled the detection of side-shifts and parallel shifts that were performed by the AuNP-motor at the end of the pause. The histogram of side-shifts showed a broad distribution between ± 40 nm having peaks at ± 10 nm to the left and right. The observation that (i) the size of the side-shift was directly correlated with the side distance fluctuation, and (ii) that smaller side-shifts occurred more often than larger ones, led to the conclusion that the majority of events were caused on lateral PFs. This is a counter-intuitive observation, because it was argued earlier (Chapter 3 in this work), that the top half of the MT should be freely accessible to the kinesin-1 motor (compare Appendix chapter A.7 AuNPs report on subtle details of the motor trajectory, page 117, i.e. the AuNP event in Supporting Fig. 9, which allowed counting the available PFs). Hence, this observation is indication that

the description of the motor tail by the rigid linker model may not be appropriate.

The main reason, why the rigid linker assumption does not hold, is the large flexibility of the kinesin-1 tail, which renders the AuNP to undergo tethered diffusion in a potential [121]. According to that, the tethered AuNP explores a volume within the 65 nm reach around the motor. Not accessible by the AuNP is the space occupied by the MT and the glass substrate. Thus, a AuNP tethered to a motor on a lateral PF is able to scan the volume only next to the MT and above the glass surface, leading to the probability of presence of the AuNP being slightly shifted toward the top of the MT. As a consequence, on lateral PFs the kinesin-1 tail might adopt a bent configuration. Such a tail bending could be the reason for the reduced side distance fluctuation observed for AuNP-motors located on lateral PFs, where, similar to tweezer experiments, an applied force stiffens the tail [122]. Furthermore, a bent tail would prevent the direct allocation of differently sized side-shifts to a certain pair of PFs. The degree of bending of the tail is not accessible directly, however may be inferred from the experimental results in combination with an appropriate model.

Answering the question whether roadblock circumvention originates from a direct side step to an adjacent PF or an intermittent detachment and re-attachment process is intricate. On the one hand, jumping events indeed occurred more often in presence of roadblocks (see Table 3, page 68) with equal probability into the forward and backward direction. Furthermore, approximately 30 % of the pauses were terminated by jumps of more than ± 25 nm parallel to the MT. The spatio-temporal resolution of the AuNP-motor was not sufficient to discriminate side-shifts into a detachment/re-attachment or a direct step process, because a diffusive transition from a PF to the neighboring one takes place on the µs timescale. Thus, the acquisition time of 1 ms applied here is too long to resolve nm-sized diffusion-based transitions.

On the other hand, it was found that first, in 66 % of all AuNP events, the pausing phase was terminated by a side-shift, notably in absence of sudden

forward or backward jumps (61 %, 80 %, and 66 % at 0 nM, 2 nM, and 4 nM roadblocks). This finding provides indication that the pausing phase may also be terminated by a movement of the AuNP-motor to an alternative binding site on a neighboring PF as argued previously [38,40,41,123,124]. It can be speculated that during the pausing phase, the trailing motor head holds contact to the MT lattice while the leading head performs a diffusive search for available tubulin dimers next to the blocked one.

Secondly, the directionality of the circumvention move was strongly shifted into the forward direction (Fig. 26B, 83 % of the pauses were overcome in forward direction). This is indication that roadblock circumvention after the pause is directionally biased in contrast to jumps without prior pausing. The directional bias could originate from two effects: First, to obtain information on the parallel movement of the motor after the pause, the AuNP position was averaged. However, the probability of missing several forward steps was kept to a minimum, by using a short time window of only 10 ms, corresponding to the mean waiting time per step. Secondly, it can be hypothesized that the unbound motor head undergoes electrostatically guided diffusion-to-capture by MTs [125]. The free motor head is thereby thought to be oriented, steered, and guided forward into an electrostatic channel, which is formed by the interaction of surface charges on the motor domain and the tubulin dimer. In close proximity to the MT surface, this mechanism could explain both, a screening process of the free head for alternative binding sites in forward direction next to the blocked site as well as a forward-biased diffusive-process of immediate detachment and re-attachment.

Another indication for a direct circumvention step can be obtained from the stepping probability heat map and the polar histogram of the stepping directions (Fig. 26C). These results showed that the motor utilized alternative binding sites located on the left and right of the blocked site. For strongly forward directed movement, a slight left tendency was observed, in contrast to a right tendency being found for strict sideways-directed shifts. Although these binding sites could be reached by both, a direct step and a

diffusive process, the observation of a slightly asymmetric stepping pattern, showing enhanced occurrences of movements toward the forward-left and forward-right tubulin dimers, could originate from direct steps utilizing the asymmetrically distributed tubulin dimers lying in front of the motor (compare Fig. 26C, right inset, [126]). More precisely, the PF on the left is shifted 1 nm toward the plus end, whereas the PF on the right lacks 1 nm behind [127]. From a geometrical point of view, a step to the right and forward-right tubulin dimer requires a step size of ~ 9.2 nm and ~ 16.2 nm, respectively, which is well in the range of the step size carried out along the PF. In contrast, a step to the left and forward-left tubulin dimer requires larger step sizes of ~ 10.8 nm and ~ 18.0 nm. Since the short, 14 amino acid neck linker of kinesin-1 is thought to be optimized for reaching the next binding site along the same PF and consequently does not allow protrusions much further than 16 nm [27,38], it was expected that the forward-left tubulin dimer is out of reach. Instead, it was found that the stepping probability heat map indicated the existence of a forward-left binding site questioning the concept of the neck linker being treated merely as a geometrical element.

No direct information about the length of the kinesin-1 neck linker is available, nevertheless estimations yielded values of 6.5 nm [68], 7 nm [123], and 8-10 nm [38,78]. It is known that longer neck linkers caused kinesin-1 to (i) perform forward steps longer than 8 nm and (ii) side steps to adjacent PFs more often [38], however detailed knowledge of how increasing the length of the neck linker translates into increased step sizes is lacking.

A somewhat inspiring approach was carried out by Bormuth. et. al. [68], who described the kip3 motor domains using a three-dimensional model taking into account the excluded volume of the motor heads and neck linkers. They found the forward-left tubulin dimer to be favored for binding because the neck linker could wrap around the motor domains more easily as compared to side steps to tubulin dimers on the right. Thus, not only the pure length of the neck linker matters but instead the three-dimensional arrangement of the linker relative to the motor domains. A similar approach

for kinesin-1 may provide valuable information on the availability of alternative binding sites on adjacent PFs.

A second cause for the asymmetric distribution of stepping directions could originate from the asymmetric hand-over-hand mechanism, which was demonstrated for the kinesin-1 motor protein [124]. The asymmetry is a consequence of the non-mirror-symmetric arrangement of the two motor monomers within the dimer. The two motor heads are thought to alternate between two asymmetric steps, where one step involves the trailing head to swings up and over the leading head, i.e. moving in a vertical plane relative to the MT surface, whereas the newly trailing head swings around to the side of the newly leading head, i.e. moving in a horizontal plane relative to the MT surface, [113,128-130]. Thus, a step in the horizontal plane could involve screening for potential binding sites on the adjacent PF, whereas the step in the vertical plane might be restricted in screening range. Since the detailed asymmetric trajectories of each motor head are unknown, it is not clear which of the two asymmetric processes makes up the 'right' and 'left' step. However, from the high-resolution X-ray structure of MTs decorated with kinesins-1, Hoenger et. al. [113] concluded, that the horizontal step occurs on the right. This could explain that side steps to the right were observed in forward-right and right direction, whereas side steps to the left PF were mainly found in forward-left position.

The finding of kinesin-1 exhibiting extended pausing times of 0.39 ± 0.04 seconds, reflects the fact that stepping to an adjacent PF has a low probability and that trailing head detachment is suppressed until the leading head made a connection to another tubulin dimer [38]. Thus, when a roadblock is occupying the next tubulin dimer, the leading head of the kinesin-1 motor cannot bind immediately, and the trailing head cannot detach. This keeps the motor in the pausing phase, which is ceased by detachment of the trailing head, or binding of the leading head to an adjacent PF. By comparison, the pausing phase was 50 times longer than the average waiting time per step of $\sim 10 \, ms$, which is in agreement with previous

85

publications [16,17], but disagrees with one other publication [66]. There, the pausing time of kinesin-1 on roadblock saturated MTs was determined to 24 ms using stopped flow and flash photolysis experiments in combination with dynamic light scattering. The difference in waiting time could be attributed to the enormous roadblock density applied in their study causing the motors (i) to perform only ~ 2.5 steps before encountering a roadblock possibly due to a charge effect of the massively crowded environment and (ii) to experience a limited availability of alternative binding sites on adjacent PFs. Thus, the kinesin-1 motor might exhibit a waiting phase in front of a roadblock only when enough space for the diffusive search of the free head is available. Furthermore, it can be speculated whether motor proteins with a tendency to perform side steps to a specified direction, such as kip3, might not utilize waiting phases when confronted with a roadblock, because an alternative route via side stepping to an adjacent PF is available.

Lacking the necessary temporal resolution to discriminate clearly between a direct step and a diffusive transition, it cannot be answered satisfyingly, if both processes co-exist, or if side-shifts originate from an intermittent detachment/re-attachment process causing jumps to be too short and too fast to be reliably detected with the approach utilized herein. Thus, it is concluded, that given the spatio-temporal resolution provided by the AuNP label, kinesin-1 motors are considered to utilize both, detachment and forward-biased re-attachment as well as direct stepping to the adjacent PF to get around a blocked tubulin dimer. Further investigations of road-blocked AuNP-motors are necessary to clearly discriminate between the two hypotheses. Serendipitously, AuNPs provide a sufficiently large number of photons to allow imaging with even faster cameras than the one utilized here.

5. Summary and outlook

Aspiring toward an improved understanding of (i) how the motor protein kinesin-1 is affected when confronted with permanent roadblocks and (ii) how the motor actually circumvents blocked sites along its path, a novel quartz-based parabolic prism-type, wide-field TIR microscope was developed. This new approach allowed the application of strongly scattering AuNP labels to report on the nanometer-precise position of the motor protein by still providing the necessary sensitivity to image SM fluorescence with high SNRs. The parabolic shape of the prism thereby allowed adjusting the penetration depth of the evanescent field – while keeping the illuminated area at the same location – establishing an easy-to-use instrument comparable in usability and comfort to common objective-type TIR microscopes. Interestingly, the device is easily implemented into any commercial microscope in place of the usual bright-field condenser, which highlights the enormous potential of scattering nanoparticles to replace organic dyes, fluorescent proteins, and quantum dots in SM experiments in the future. The development of high-performance and easy-to-use imaging devices, such as the parabolic prism-type TIR setup described here, is expected to accelerate this development.

Future applications of parabolic prism-type TIR

Several aspects of the parabolic prism-type TIR setup were not utilized in this work however they are of particular interest to the imaging community. First of all, the rotational symmetry of the prism allows for polarization- and direction-independent TIR illumination, e.g. by providing a second laser beam entering the prism at a position shifted 90° relative to the position of the first laser. This approach would enable (i) the illumination of both, fluorescent and scattering entities, with enhanced efficiency thus resulting in the detection of larger signals and (ii) the imaging of larger, e.g. cellular, structures without the effects of shadowing [99,131]. Secondly, the quartz material allows TIR

illumination with ultraviolet wavelengths down to approximately 200 nm. This is particularly interesting because commonly used TIRF objectives to date do not offer reasonable transmission below 350 nm. Thus, the application of parabolic prism-type TIR is expected to cover the shortcomings of today's (objective-type) TIR-based imaging techniques.

Prism-type TIR enables fluorophores to be replaced by scattering probes

A quantitative comparison of the detection efficiencies of prism-type and objective-type TIR setups revealed that objective-type TIRF generally collects more photons than prism-type TIRF, mainly because near-field emission into the glass substrate (i.e. into the direction of the image-collecting objective) is enhanced. This affects the SNRs obtainable for photon-limited fluorescent probes, however for scattering probes this resembles a negligible problem because the photon yield is several orders of magnitude higher and thus not limiting. Prism-type TIR is consequently the method of choice for the imaging of scattering probes, which naturally overcome the intrinsic limitations of photobleaching, photon blinking, and saturation inherent to fluorescent probes.

The advantage of using scattering particles instead of fluorescent probes was exemplified by performing localization studies on surface-immobilized 40 nm AuNPs. These probes were reliably localized to below 1 nm, a precision, which relies on the facts that (i) the peak positions of Gaussian photon distributions can be localized with much smaller errors than the optical resolution limit and (ii) the errors scale inversely with the square root of the number of collected photons. The enormous scattering cross-section of AuNPs gives them a distinct advantage with regard to the latter criterion. The applicability of these particles for the detection of conformational changes of biomolecules was exemplified for the detection of the characteristic 8-nm steps of individual kinesin-1 motor proteins walking along MTs. Notably, when attached to the tail of kinesin-1, the AuNPs were localized to approximately 3.8 nm, which strongly encourages further

applications of AuNPs to study conformational changes of proteins *in-vitro*. Nonetheless, the high flexibility of the kinesin-1 tail prevented the AuNPs from being localized to below 1 nm, as demonstrated for substrate-attached AuNPs. However, this can be addressed by genetically engineer shorter tails or facilitate several bonds between the AuNP and the tackled domain on the protein. Here, a shortened kinesin-1 construct was utilized, which was truncated behind the first dimerization domain. Any further shortening of the tail would prevent dimerization of kinesin-1 leading to non-processivity [132].

Moreover the large size of the AuNP can be a limiting factor. This is because the volume of the AuNP can interfere with the conformational change of the protein. In such cases, three bypasses are of particular interest to circumvent that problem:

a) Reducing the size of the AuNP label: The detection of smaller AuNPs with a diameter of only 20 nm was reported earlier [133], however detection was only possible on clean glass surfaces free of additional proteins. Since the scattering cross-section scales with the radius R of the AuNPs to the power of six (proportional to R^6), a 64-fold lower photon emission rate is obtained for 20 nm compared to 40 nm AuNPs. This poses a problem, because protein-decorated glass surfaces as well as the MTs themselves scatter a small portion of the illumination light, rendering discrimination of smaller particles from the background intricate. In this work, individual particles smaller than 20 nm were not reliably detected (data not shown).

The large size of the AuNP label did not cause sterical constraints when bound to the tail of kinesin-1. This is because the protein is evolutionarily optimized for the transport of large cargos, having sizes of up to several hundred nanometers. Thus, when bound in a cargo-like manner, the 40 nm AuNP resembles an ideal reporter for molecular movements. It is therefore expected that motor proteins, optimized for either (i) efficient transport, (ii) positioning of large intracellular vesicles, or (iii) movement of large protein structures, are ideally suited for an investigation using scattering nanoparticles.

b) Changing the shape of the AuNP label: A larger scattering cross-section can be obtained by deforming the AuNP, i.e. using elongated gold nanorods (AuNRs) instead of spheres. This however comes for the prize, that the AuNRs are strongly orientation-dependent scatterers, which offer a strong signal only when their long axis is oriented perpendicular to the incoming illumination light. Although this can be of interest to some applications [134,135], this bypass is still dictated by the scaling of the scattering cross-section with the aspect ratio of the probe to the power of six.

c) Changing the material of the label: Silver nanoparticles (AgNPs) were shown to provide even larger scattering cross-sections and narrower plasmon resonances than AuNPs [136]. However, AgNPs exhibit weak photostability due to photon-induced oxidation even under ambient conditions [137], which causes free silver ions, having the potential to denature proteins, to be released from the particles [138]. Photo-oxidation was significantly reduced by either coating the particles with dendrimers [139] or by performing experiments in anaerobic conditions [138], in essence canceling the toxic effect of AgNPs on microorganisms. Since fluorophore excitation was shown to cause the generation of free oxygen radicals harming the integrity of proteins [140], oxygen removal is actually beneficial for *in-vitro* motility assays.

d) Imaging techniques based on interferometry: An alternative imaging approach makes use of the interference between scattered and reflected light, whose signal amplitude was shown to scale with the radius of the particles to the power of three, hence enabling the detection of AuNPs with diameters of only 5 nm in aqueous solution [79,141]. A particularly interesting application of this technique was demonstrated by Kukura et. al. [142], who imaged the position and orientation of single quantum dot-labeled virus particles by utilizing the interferometric scattering signal of the virus and the single-particle fluorescence of the quantum dot. Currently, this technique is exploited toward the label-free imaging of vesicles and resembles an attractive

technique to achieve μs acquisition times in the future (see [143] for an excellent review).

The driving force for the development of a scattering-based imaging technique was the low spatio-temporal resolution and short observation time with which fluorescently labeled motor proteins can be observed. The limitations, namely photobleaching, photon blinking, fluorescence saturation, and a low number of photons being generated upon excitation [75-77], are intrinsic to fluorescence and lead to a trade-off between spatial resolution and total observation time. Although this problem can be partly compromised by using extremely stable fluorescent probes (such as Yildiz et. al. [40]), enhanced photon emission and thus increased localization precision generally limits the total observation time of the labeled protein. Typically, the resolution of GFP-labeled motor proteins is limited to some tens of nanometers in space and about hundred milliseconds in time. Thus, the simultaneous observation of the nanometer-precise stepping of motor proteins along PFs over extended periods of time is not possible.

As a consequence, TIRF microscopy of GFP-labeled kinesin-1 motors literally treats the individual kinesin-1 motors as steadily moving molecules, advancing uniformly by 800 nm per second on a 25 nm wide one-way MT road. For the investigation regarding the deterioration of the motility parameters in dependence on the mean spacing of roadblocks, as presented in chapter 3, TIRF microscopy still yielded valuable information. However, applying AuNPs to the tail of the motor protein markedly increased the information content of the molecular trajectories, clearly enabling the detection of switches between PFs, stop-and-go motion, and 8-nm stepping due to the spatial resolution in the few-nanometer regime and a temporal resolution of 1 ms.

The results presented in chapter 3 and 4 contribute to the ongoing debate of how kinesin-1 deals with permanent roadblocks. The deterioration

of the mean velocity is clear evidence for the existence of waiting phases, a fact which was further verified by the finding that the run length deteriorated faster (6-fold) than the dwell time (2-fold). The length of the waiting phase was determined to 0.5 seconds and 0.39 seconds in two independent approaches, resulting in a 2- to 3-fold enhanced off-rate when kinesin-1 is dealing with a roadblock compared to the unhindered off-rate.

Using AuNP-motors, it was possible to detect differently sized side-shifts at the end of the waiting phase in 66 % of the cases. Together with the finding that the majority of circumvention steps resulted in a bias into the forward direction (83 %) and that the direction of the circumvention move reproduced the distribution of tubulin dimers around the blocked site lead to the conclusion that the roadblocks can be circumvented by a direct step to an adjacent PF. The directions of circumvention steps indicated that a left- and right-circumvention step was equally likely. Thus, the kinesin-1 motor protein, formerly expected to be strongly restricted to the tubulin dimer lying in front, can actually utilize alternative binding sites on the left and right of the blocked tubulin dimer.

However, a diffusion-based process based on detachment and immediate rebinding could not be ruled out as a major mode of circumvention. Quite to the contrary, roadblock addition caused AuNP-motors to show an enhanced probability for jumps parallel to the MT lattice and about 30 % of the pausing phases were terminated by such jumps. Interestingly, kinesin-1 also showed stepping to an adjacent PF without pausing, indicating that the PF tracking mechanism of kinesin-1 is not perfect, resulting in a PF switch every 500 steps.

A model of kinesin-1 being road blocked: The following model of kinesin-1 when dealing with a roadblock is therefore proposed (Fig. 29): *The processivity of kinesin-1 results from mechanical and chemical coordination between the two motor heads causing the trailing head to remain bound to the MT until the front head made a connection to another tubulin dimer thereby*

favoring the one, which lies along the same PF [34,37,38,41,125]*. When this tubulin dimer is occupied by another molecule, the front head cannot bind to the favored position while the trailing head holds on to the MT. This traps the motor protein in a paused state* [16,67] *thereby allowing the small probabilities of stepping to the tubulin dimer on the adjacent PF to become important. The pausing phase can be terminated either by (i) the leading head facilitating a side step to an adjacent PF or (ii) the trailing head detaching prematurely from the MT lattice. In the former case, electrostatically biased diffusion of the free motor head allows the screening for tubulin dimers on the left and right of the blocked site, eventually enabling a side step. In the latter case, the detached motor protein performs an electrostatically biased diffusion, which either leads to immediate re-binding to the MT in forward direction, i.e. behind or next to the blocked site, or to free diffusion into solution.*
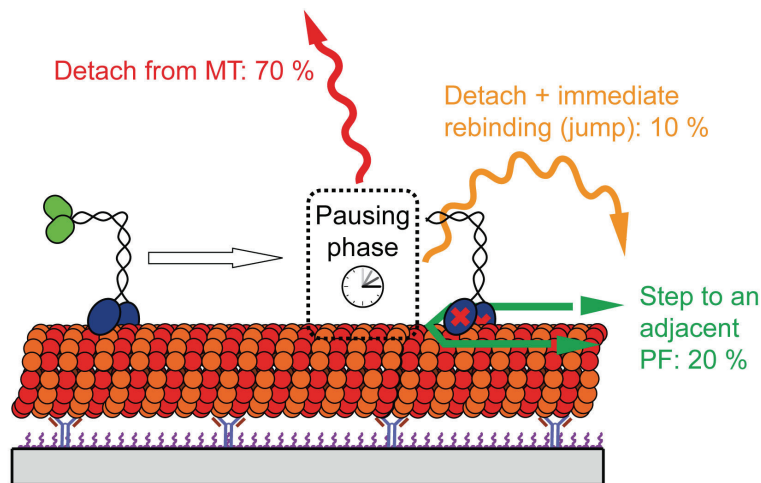
Fig. 29 | Model of kinesin-1 dealing with permanent roadblocks.
A walking kinesin-1 motor encounters a permanent roadblock and switches into a pausing phase (dotted box). The pausing phase is terminated primarily by detaching from the MT (red pathway), however, in 30 % of the cases the motor overcomes the blocked site (i) by side stepping to the neighboring PFs (green arrows), and (ii) by so-called jumps, which presumably consist of detachment followed by forward-biased diffusion and immediate re-binding (orange arrow).

This mechanism allows efficient transport and positioning of vesicles by kinesin-1. While transporting, small groups of kinesin-1 motors share the task of vesicle delivery. When one motor detaches, due to the processivity of

only 1 μm, another motor can take over the job of transportation. When confronted with a stretch of roadblock-decorated MTs, the motors individually exhibit waiting phases before detaching. The same mechanism that causes multi-motor transport to show longer run lengths and dwell times compared to SM transport, causes a small group of road-blocked motors to allow long-term halt of the vesicle and thus provide a means to position the cargo.

Native MAPs might influence kinesin-1 motility differently

The rigor kinesin-1 mutant used as the roadblock in this study offered irreversible binding to the exact same binding site as the kinesin-1 motor. This approach enabled (i) control over the mean spacing of roadblocks, which was held constant over the time course of an experiment and (ii) to selectively hinder the stepping of kinesin-1. Other native, neuronal roadblocks and MAPs, such as tau, may not bind irreversibly to the MT lattice and may not occupy the same binding site [71]. Thus, it would be interesting to investigate how the motility parameters of kinesin-1 depend on increasing concentration of native MAPs and whether waiting phases are still present. It can be speculated that native MAPs might possess 'road-blocking' and 're-routing' properties at the same time, intrinsically carrying the information telling a motor to either stop permanently, detach, detour, or even turn around. Such an interaction was in part observed for tau proteins and dynein motors [12] and could alternatively explain why native MAPs did not cause a significant slow down in the transport velocity of molecular motors. Thus, comparing the circumvention behavior of AuNP-loaded kinesin-1 motors when being confronted with various native roadblocks might provide more insight into the *in-vivo* function of both, the motor protein and the roadblock.

Kinesin-1 as a marker for neurodegenerative diseases

The finding that the landing rate deteriorated significantly came as a surprise, because only 1 % of the tubulin dimers were occupied under these conditions. Thus, the kinesin-1 motor protein is expected to accurately 'sense'

the crowdedness of the MT lattice. This is a promising starting point for investigating the possibility to utilize impaired molecular transport as an indicator for the onset of neurodegenerative diseases. This approach would be particularly useful because neurodegenerative diseases are diagnosed mainly by symptoms occurring in later stages, such as atrophy of brain matter, accumulation of protein aggregates and dementia. Thus, future investigations of how roadblocks affect the motility parameters of kinesin-1 motors *in-vivo* are necessary in order to utilize this interaction for diagnosis.

The kip3 motor as a model side stepper

For further insight into the mechanism of roadblock circumvention, the kinesin-8 motor protein kip3 is a highly promising candidate. This motor, moving with a velocity of ~ 50 nm/s (15-fold slower than kinesin-1), was shown to exhibit an extreme processivity of up to 12 μm, allowing the motor to (i) walk along the complete length of a MT and (ii) perform a length-dependent depolymerization at the MT plus end. The underlying mechanism was described by an antenna-model, where the uniform binding of kip3 motors along the entire length of a MT leads to subsequent accumulation of motors at the MT plus end [144]. Thus, the longer the MT, the more motors accumulate at the end, leading to faster depolymerization compared to shorter MTs. The task of kip3 therefore involves measurement of the length of a MT. This explains why kip3 needs an extreme processivity, because premature detachment would disrupt efficient length determination.

However, during the long runs of this motor protein, encounters with roadblocks are expected to occur frequently *in-vivo*. Thus, it can be speculated whether the recent finding of kip3, being able to step toward the left PF [68], is the result of an evolutionary optimized process, that enables a highly efficient roadblock circumvention. This is what makes the investigation of kip3 in presence of roadblocks an ideal follow-up experiment, because it leaves the researcher with an interesting hypothesis: The extremely low detachment rate of kip3 results in its extreme processivity enabling the protein to reach the end

of the MT. During the long runs, a large number of roadblocks may need to be circumvented. Since the motor is capable of readily moving forward (90 %) and leftward (10 %), it is hypothesized that the motor can efficiently utilize this pathway to get around a blocked site. Thus, it is expected that kip3 shows no or only short waiting phases when encountering a roadblock. This would be quite in contrast to kinesin-1, which waited 50 times longer than the average time per step. On the other hand, an argument against the hypothesis of an evolutionary optimized process would be obtained, if the kip3 motor is found to exhibit extended waiting phases comparable to kinesin-1. An earlier investigation of kip3 in the presence of streptavidin roadblocks by Wüseke et. al. [145] provided an indication toward the latter proposal, i.e. kip3 showed deteriorated motility however quantification of the motility parameters was obscured by photobleaching. Loading AuNPs onto the tail of kip3, would form a perfect follow-up experiment to gain insight into the significance of roadblock circumvention

Concluding remarks

The application of novel imaging techniques has been a major driving force in SM biophysics. In particular, optical techniques with their non-invasiveness, specificity, ease of use and low cost, have made microscopes the core research tools [146]. In addition, back in 1959, Richard Feynman stated "*It is very easy to answer many […] fundamental biological questions; you just look at the thing!*" [147] and thereby expressed the need for optical imaging, knowing of the magical impact an image has on the human's perception of nature.

Along these lines, the herein developed parabolic prism-type TIR microscope enabled the direct observation of kinesin-1 motor proteins and their interaction with permanent roadblocks blocking the path along the MT filament. However, the application of brightly scattering AuNPs to motor proteins only resembles one example highlighting the potential of scattering particles to replace organic dyes, fluorescent proteins, and quantum dots in SM

experiments. Therefore, future experiments may involve application of AuNPs to investigate the mechanics of biophysical processes ranging from ciliary beating over bidirectional transport to polymerization of cytoskeletal filaments. Thus, the availability of high-performance and easy-to-use imaging devices, such as the parabolic prism-type TIR setup described here, are expected to contribute and facilitate this development.

6. Materials and methods

All experiments were performed in flow cells constructed from 22x22 mm² and 18x18 mm² glass slides (#1.5, Gerhard Menzel Glasbearbeitungswerk GmbH & Co. KG, Braunschweig, Germany) and 1 mm wide stripes of double-sided sticky tape. Glass slides were rendered hydrophobic before use by treatment with dichlorodimethyl-silane (DDS, Sigma). Typically, the channels were 18 mm in length, 2 mm in width and 100 μm in height resulting in an inner volume of approximately 4 μL (see [61] for more experimental details). The standard buffer solution in our experiments was BRB80 (80 mM potassium PIPES, pH 6.9, 1 mM EGTA, 1 mM $MgCl_2$).

6.1 Scattering probes

Two different probes were used as *surface-immobilized scatterers*: 40 nm streptavidin-coated AuNPs (British Biocell International, Cardiff, UK) as well as 100 nm Tetraspeck beads (Invitrogen, Carlsbad, CA, USA). For immobilization of 40 nm streptavidin-coated AuNPs (Tetraspeck beads) the stock solution was diluted 1000-fold in BRB80, flushed into a channel of a flow cell made from clean cover slips and incubated for 30 seconds (5 minutes). Unbound AuNPs (Tetraspeck beads) were removed by washing with 20 μL BRB80. To prevent evaporation, channels were sealed using nail polish. *Antibody-conjugated AuNPs* were prepared from 40 nm streptavidin-conjugated AuNPs and biotinylated GFP antibodies (from MPI-CBG, batch number 106A20). A volume of 500 μL of the streptavidin-conjugated AuNP stock solution was centrifuged for 3 minutes at 10,000g and, after collecting 450 μL of supernatant, resuspended to the same volume of BRB80 supplemented with 1% Tween20. Repeating this procedure three times ensured reduction of free streptavidin and other chemicals. After the last centrifugation step, the remaining 50 μL of AuNP solution was mixed with

10 μM of biotinylated GFP antibody (in a ratio of 180 antibodies per AuNP) and kept at 4° C over night. The next morning, the AuNP solution was diluted to the same starting volume (500 μL) and was again centrifuged three times for 3 minutes at 10,000g to reduce the amount of free antibody. After the last centrifugation step, the total volume was reduced to 50 μL and the concentration of AuNPs was measured in a spectrometer according to the method described in [148]. Typically, the final solution of antibody-conjugated AuNPs had a concentration of 10 nM to 25 nM and was always made freshly the day before use.

6.2 Proteins

Fluorescent MTs were polymerized from 5 μL of a 1:3 mixture of rhodamine-labeled and unlabeled porcine brain tubulin (4 mg/mL, self-made tubulin purification according to [149]) in BRB80 with 4 mM $MgCl_2$, 1 mM MgGTP, and 5 % DMSO. After 30 minutes, microtubule polymers were stabilized by the addition of BRB80T (BRB80 with 10 μM taxol) and stored at room temperature. MTs were always made freshly before each experiment. For stepping assays a *GFP-motor*, based on a truncated, eGFP-labeled rat kinesin-1 construct (rkin430eGFP, originally from the Cross lab [28]) was expressed. This dimeric protein contains the first 430 amino acids of conventional kinesin-1 fused to an eGFP domain and a polyhistidine (HIS) tag at the tail. An *unlabeled motor* protein (rkin430) was derived from the GFP-motor by introducing a polyhistidine tag terminated by a stop codon before the eGFP domain. *GFP-labeled and unlabeled roadblocks* were generated from the GFP-motor and unlabeled motor, respectively, by performing a T93N single-point mutation, similar to the method described in [16]. The motor proteins and roadblocks were expressed in *E. coli* and purified by affinity chromatography on Ni-NTA columns.

6.3 Loading of AuNPs to motors

Loading of antibody-conjugated AuNPs to GFP-labeled motor proteins was performed by incubating AuNPs and GFP-motors in ratios ranging from 1:1 to 10:1, for 15 minutes. Always the lowest ratio that still produced transported AuNPs was used. The concentration of GFP-motors in the incubation varied between 1 nM and 5 nM.

6.4 Stepping assays for GFP- and AuNP-motors

For GFP-motor stepping assays the flow cell was washed with a sequence of buffers to allow fluorescent MTs to bind to the glass substrate. First, a solution of β-tubulin antibodies (0.5% SAP.4G5, Thermo Fisher Scientific) diluted in BRB80 was incubated for 5 minutes, followed by a washing step with BRB80. The channel was then incubated with 1% Pluronic F127 in BRB80 for a minimum of 15 minutes. Subsequently, the channel was washed with 80 µL of BRB80T. A solution of MTs was flushed in and was allowed to adsorb for 1 minute. Unbound MTs were removed from the channel by washing with 40 µL BRB80T. The microtubule density on the glass substrate was checked under the microscope before continuing with the flow sequence. Finally, 20 µL of 150 pM to 250 pM GFP-labeled motors in imaging buffer (265 µg/mL Casein, 47 mM Glucose, 130 µg/mL Glucose Oxidase, 24 µg/mL Catalase, 12 mM DTT, 1.2% Tween20, and 1.2 µM to 1 mM MgATP in BRB80T) were flushed into the channel. For the experiments involving roadblock decoration of MTs, the channel was washed for 1 minute with 0.2 nM to 4 nM GFP-roadblocks and 0.75 nM to 15 nM unlabeled roadblock in imaging buffer. Subsequently, the roadblocks were replaced by 20 µL of imaging buffer. For the experiments involving AuNP-loaded motors, the AuNP-motor incubation was diluted in imaging solution to a final 150 pM to 250 pM AuNP concentration and subsequently flushed into the channel. The mean velocity of a single molecule (termed 'mean SM velocity') was determined by fitting a line to all data points making up the time-displacement curve. The mean velocity of a population of many single molecules was obtained by

averaging over all thus obtained mean SM velocities. AuNP events were excluded from the analysis when their attachment and detachment was not covered in the movie stream. Given the implications involved in proving for SM transport of AuNPs in these experiments, ultimate care was taken in selecting and rejecting events from the analysis.

6.5 Imaging

For all experiments described in chapter 2, image acquisition was performed using an inverted Axiovert 200M microscope (Zeiss, Göttingen, Germany) in combination with an Andor iXon DV 897 electron-multiplied (EM) CCD camera (Andor, Belfast, Northern Ireland). For all other experiments an inverted AxioObserver from Zeiss in combination with (i) an Andor iXon DV 897E EM CCD camera and (ii) an Andor Neo scientific CMOS (sCMOS) camera was used. Image capture was performed using a PC and imaging software MetaMorph (Molecular Devices, Sunnyvale, CA, USA). Both microscopes were equipped with a Lumen 200 metal arc lamp (Prior Scientific Instruments, Jena, Germany) to provide fluorescence in epi-illumination.

Fluorescence imaging with prism-type TIR microscope: For excitation of eGFP-labeled proteins (FITC-labeled streptavidin) the following laser sources were used: (i) the 488 nm laser line of a fiber-coupled Innova 70C spectrum laser (Coherent, Santa Clara, CA, USA) or a (ii) Stradus 488-50 mW diode laser (Vortran Laser Technology Inc., Sacramento, CA, USA). The following filters were used for imaging: excitation 488/10, dichroic 505LP, emission 515/30, all from Chroma (Bellows Falls, VT, USA). The EM gain of the CCD camera was typically adjusted to between 100x and 300x. For the excitation of 100 nm Tetraspeck beads and rhodamine-labeled MTs the following laser sources were used: (i) the 530 nm laser line of the Innova 70C spectrum laser or a (ii) Cobolt Samba 100 mW 532 nm laser (Cobolt AB, Solna, Sweden). The following filters were used for imaging: excitation 535/50, dichroic 565LP, emission 610/75, all from Chroma. Fluorescence was collected using a 63x C-Apochromat 1.2W Korr from Zeiss. The power of the lasers was measured with a power meter just before the laser beam entered the prism.

Fluorescence imaging with objective-type TIR: For objective-type TIRF a slider system from Zeiss was used, which was fiber-coupled to the aforementioned lasers. Focusing of illumination light and detection of fluorescence was achieved using a 100x alpha Plan-Apochromat NA1.46 from Zeiss. The power of the illumination light was measured with a power meter when the laser beam exited the TIRF objective in a straight line.

Scattering imaging with prism-type TIR microscope: For illumination of the AuNPs and the 100 nm Tetraspeck beads the aforementioned 530 nm (532 nm) lasers were used. Scattered light was collected using a 63x C-Apochromat 1.2W Korr. No additional spectral filters were used and the EM gain of the camera was set to 1x. For stepping assays with AuNP-loaded motors described in Chapter 2, half of the 512 x 512 pixel camera chip of the EM CCD was utilized to achieve acquisition times of 15 ms. For all other experiments with AuNP-loaded motors, the smallest region of interest (144 x 128 pixels) of the water-cooled sCMOS camera was utilized, allowing for 1 ms acquisition time in rolling shutter mode. Water-cooling was achieved using an Exos-2.5 Liquid Cooling System (Koolance, Auburn, WA, USA). The brightness of the AuNPs was adjusted by varying the power of the 532 nm laser, which was measured with a power meter just before the laser beam enters the parabolic prism.

6.6 Bleaching assays

The bleaching times of immobile eGFP-labeled motor proteins were measured in a stepping assay configuration. Surface-immobilized MTs were incubated for 1 minute with 300 pM rkin430eGFP in the presence of 10 μM AMP-PNP, followed by washing with 20 μL imaging buffer. Upon laser illumination with 488 nm, SM bleaching events were imaged by continuous streaming with 100 ms acquisition times. The decay in fluorescence intensity superimposed with the MTs was measured over time and fitted to a mono-exponential function to yield the characteristic decay constant τ_{bleach}. The individuality of the molecules was checked by detecting several two-step bleaching processes (data not shown). The noise level b was determined by

calculating the standard deviation of the background signal in regions, which were close to the MTs but did not contain any fluorescent molecules during the whole stream. To match the apparent pixel size of the camera to 102 nm (100 nm) per pixel an additional 2.5x (1.6x) lens was placed in the detection path of the 63x water objective (100x oil-objective) used for prism-type (objective-type) TIRF. All measurements where performed within the same time span right after flushing in the final imaging solution (typically 5-10 minutes). The camera settings for both TIR setups were exactly the same. The parabolic prism-type TIR setup was compared to objective-type TIR setups at different excitation powers that caused equal bleaching times. A total of 225 (362) molecules being bleached with the parabolic prism-type (objective-type) TIR setup showed mean amplitudes of 240 ± 78 (1136 ± 406) counts, background level of 177 (497) counts with a noise level b of 50 (107) counts. The measured widths of the molecules (prism-type: 135 ± 19 nm, N = 225, objective-type: 131 ± 13 nm, N = 362, mean $\pm$ sd) were found to differ significantly ($p < 0.005$, Welch's unpaired t-test) in both setups, however the width was found to have negligible impact on the determination of the difference in SNRs between both setups. Therefore, the amplitude of the molecules rather than their volume intensity was used as a measure for the number of photons being collected.

6.11 Localization of point-like objects

To study the localization precision, immobile eGFP-labeled kinesin-1 motor proteins were bound on MTs and their localization error was compared with (i) streptavidin-conjugated 40 nm AuNPs immobilized on the substrate and (ii) streptavidin-conjugated 40 nm AuNPs bound to the tails of immobile kinesin-1 via a biotinylated anti-eGFP antibodies. Several movie streams of the AuNPs were collected while varying the acquisition times from 1 to 100 ms and excitation powers from 5 mW to 100 µW. Image analysis was performed using FIESTA tracking software [106], which fits two-dimensional Gaussians to the pixelated intensity distribution of the objects and extracts the center

position (x_i- and y_i-coordinate) of the intensity maximum, the width σ_i of the distribution, and the amplitude A_i of the maximum above background in every i-th frame. The distribution of the center positions in every frame resembled a symmetrical two-dimensional distribution (estimated by a normal distribution) around the mean position whose width is termed 'localization error'. The pixel size of the camera, the sensitivity of the chip, and the applied magnification was used to convert the volume under the fitted distribution into the number of detected photons per frame. Stage drift was corrected by separately tracking the positions of 100 nm Tetraspeck beads. The measured localization errors were compared to a theoretical expression derived by Thompson et. al. [150] describing the uncertainty in each dimension <Δx>:

$$\langle \Delta x \rangle = \sqrt{\frac{\sigma^2 + a^2/12}{N} + \frac{8\pi\sigma^4 b^2}{a^2 N^2}} \ . \tag{S1}$$

Here, σ describes the width of the fitted Gaussian, a the pixel size of the camera, N the number of detected photons, and b the noise level. The parameters used in Eq. S1 were determined to $\sigma = 122.9$ nm, $a = 101.6$ nm, and $b = 2$ photons and resulted in good agreement with the experimental data (compare Fig. 13A, page 33, dashed line). The noise of 2 photons was estimated from the eGFP data. Selecting those molecules and particles that (i) showed less than 3000 photons per frame and (ii) were localized best in a certain interval of photon counts enabled analysis of the factor by which Eq. S1 missed the data. This factor was determined to 1.5 ± 0.1 (mean ± sd, $N = 54$ localized objects). The localization error of AuNPs attached to the tail of immobile kinesin-1 via biotinylated anti-eGFP antibodies was measured with 30 ms acquisition time and a histogram of the localization errors showed a log normal distribution (data not shown) yielding a mean localization error of 3.8 ± 1.8 nm (mean ± sd, $N = 385$ AuNPs).

For step detection, 22 AuNPs, which were transported along MTs with a velocity of 17 ± 6 nm/s (mean ± sd) at 1.2 µM MgATP, were tracked. To obtain an averaged path for each molecular event, the trajectory was fitted to a line and subsequently the movement of the AuNP was projected onto that line. An

excellent step-finding algorithm from Kerssemakers et. al. [107] was utilized to find step-like motion in the distance along the path data. This step-finding algorithm does not make an assumption about the step size. Evaluation of the step sizes of the 22 tracks was performed carefully by (i) displaying the distance along the path data versus time, without scale bars as to not provide a bias for 8 nm distances and (ii) the step size histogram was displayed only at the end of the whole evaluation (no in-between checking for 8 nm steps). Successively increasing the sampling rate of the algorithm allowed rejection of traces, which showed oversampling. Regardless of the sampling rate a majority of 8 nm steps was found in all traces. The step size distribution was fit to a three-peak Gaussian and yielded peaks at -5.5 nm, 8.3 nm and 16.5 nm.

6.12 Determination of roadblock density

Surface-immobilized MTs were pre-incubated with 0.2 nM to 4 nM GFP-roadblocks in imaging solution for 1 minute. Afterwards, the channel was washed with 20 µL of freshly made imaging solution. Subsequently, 250 pM of GFP-labeled motors in imaging solution were flushed in. Movie streams of 50 s to 100 s in length were recorded with the EM CCD camera. During the streaming process, the GFP-roadblocks photobleached within approximately 7.5 seconds and individual motor trajectories became visible. The brightness of single motors was obtained from the individual motor trajectories using FIESTA tracking software and brought into relation to the integrated GFP-signal along the MTs in the first frame. This allowed determination of the number of GFP-labeled proteins present in the first frame from which the average number of GFP-motors per frame was subtracted to yield the number of immobile GFP-roadblocks.

6.13 Computer simulation of kinesin-1 in presence of roadblocks

The computer simulation was carried out using MATLAB (The MathWorks, Natick, MA, United States). Input parameters for the simulation were the dwell time, the unimpeded transport velocity, and the roadblock spacing along a single PF, which defined the length of the free path. Motor

106

trajectories were than produced by using exponentially distributed random numbers, which resembled the time intervals of the individual 8 nm motor steps. The total length of the trajectory was given by the dwell time, which was obtained from another set of exponentially distributed random numbers. The start points of the trajectories were then uniformly distributed along the length of the PF. The motors, which encountered a roadblock and thus reached the end of a PF were simulated to exhibit a waiting phase with exponentially distributed waiting times with an average of 0.5 seconds. After the waiting phase, the motor trajectory was ceased. The mean SM velocity of a molecule was then found by fitting a line to the time-displacement curve. All thus collected mean SM velocities were collected in histograms with 100 nm/s bins. For the run length and dwell times, the CPDs were calculated and fitted to the corresponding representation of an exponential function in a CPD plot, yielding the decay constants. When the roadblock spacing exceeded the run length of the motors (>> 1 μm), the motility parameters yielded the expected values.

A. Appendix

A.1 Design of the parabolic prism

The paraboloid, custom-manufactured with the help of Dr. Volkmar Giggel from Carl Zeiss Jena GmbH (Jena, Germany), consists of a single piece of quartz with refractive index of $n_{quartz} = 1.46$ (Supporting Fig. 1A). The upper
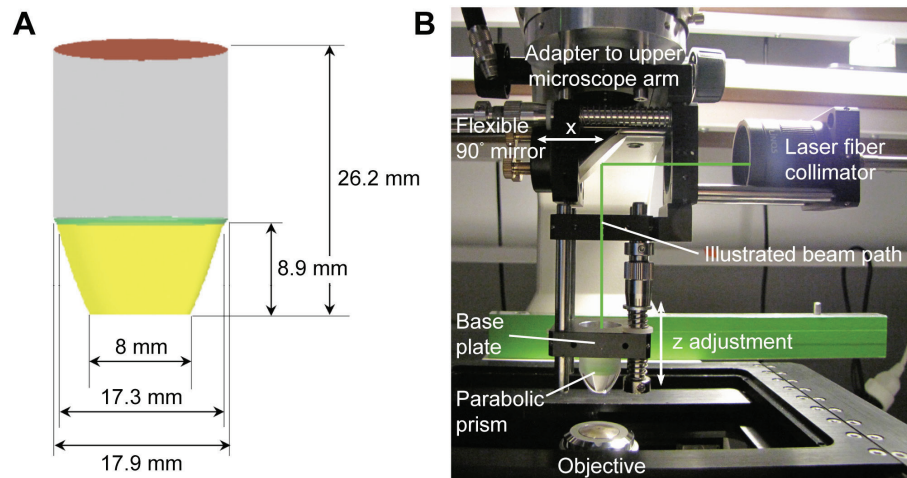
Supporting Fig. 1 | Constructional sketch and photograph of the parabolic prism-type TIR setup.
(A) The parabolic part of the quartz prism (yellow part, described by Eq. S2) stretches up to a height of 8.9 mm, where a sharp transition (green) leads into a cylindrically shaped part (grey). A laser beam enters and leaves the prism through the top surface (red). (B) A photograph of the prism holder attached to the upper arm of an inverted Axiovert 200M microscope.

part of the prism is cylindrically shaped with a height (diameter) of 17.3 mm (17.9 mm). The cylindrical shape merges into the parabolically shaped bottom part that has a height of 8.9 mm. The analytical function that describes the parabolic surface along one dimension is given by

$$f(x) = \frac{x^2}{7.2\ mm} - 2.22\ mm, \tag{S2}$$

where x denotes the distance from the optical axis. The lowest part of the parabola was cut off in order to obtain a surface at which TIR can occur. The exact cut-off height was obtained as follows: The minimum height to be cut off

is given by the distance of the focal spot from the apex of the paraboloid. Here, the focal spot is located at $z = 1.8$ mm. Additionally, a distance, which is given by the thickness of the glass slide and the thickness of the immersion oil layer, has to be cut off. The thickness of a #1.5 grade glass slide was estimated to be 170 μm, and a layer of 250 μm immersion oil was chosen for experimental practicability. This resulted in a total cut off height of 2.22 mm creating a circular bottom surface with a diameter of 8 mm.

The range of horizontal distances from the optical axis at which a laser beam can enter the parabolic prism and impinge onto the parabolically-shaped curvature is limited from 4.2 mm to 8.2 mm. Using geometrical optics and Eq. S2 a given horizontal distance can be translated into an AOI inside the quartz prism α_{quartz} (see inset of Fig. 8A for definition of angles) by Eq. S3:

$$\alpha_{quartz} = 2 \cdot \left| ArcTan\left(-\frac{1}{f'(x)}\right)\right| \cdot \frac{360°}{2\pi}. \tag{S3}$$

Here $f'(x)$ denotes the first derivative of Eq. S2. For the horizontal distances given above, this angle reaches from 80° to 47° degree. For TIR to occur at the upper glass-water interface, the laser beam has to pass from the quartz prism into immersion oil and needs to further penetrate into the top glass slide of the flow cell. Due to the different refractive indices of the quartz material, the immersion oil (Zeiss Immersol 518F, $n_{oil} = 1.52$) and the glass slide itself ($n_{glass} = n_{oil} = 1.52$), the angles calculated with Eq. S3 are subject to refraction. This was accounted for by applying Snell's law to α_{quartz} using the following equation:

$$\alpha_{glass} = ArcSin\left(Sin(\alpha_{quartz}) \cdot {n_{quartz}}\Big/{n_{glass}} \right) \tag{S4}$$

Here α_{glass} denotes the AOI inside the glass slide and was calculated to reach from 72° to 45°. All optical components were mounted in a micro bench system (LINOS, Göttingen, Germany) where the cylindrical part of the prism was fixed to a custom-made base plate (Supporting Fig. 1B). The position of the prism along the optical axis was adjusted using a fine micrometer screw. A monomode glass fiber (OZ Optics, Ottawa, Canada, article no.: LPSC-04-

400/700-3.5/125-P-6AC-11-40-3S-3AS-10, $NA = 0.1$) was coupled to the system via an adjustable fiber collimator (LINOS, Focusing Collimator MB 02 FC0/PC0, Order No. G169003000), which allowed for focusing of the laser beam. Mounting to the upper arm of an inverted microscope Axiovert 200M microscope was achieved using a custom-made adapter.

A.2 Alignment of the parabolic prism

To align the parabolic prism with the optical axis of the microscope two adjustable diaphragms were placed in the vertical beam path and the laser beam was directed in a straight line through both diaphragms by adjusting the 90° mirror. Subsequently, the diaphragms were removed and the laser beam was free to travel through the parabolic prism into the front lens of the objective. The laser beam was directed onto a sheet of paper (using the ocular port of the microscope) and was centered in the field of view using two adjustment screws on the upper arm of the microscope. This ensured that the laser beam traveled along the optical axis of the microscope. The parabolic prism was brought into contact with the flow cell by placing a drop of immersion oil on the topside of the flow cell. The prism holder was than lowered onto the flow cell by using a z-adjustment screw provided at the upper arm of the microscope until the prism touched the oil droplet.

Once in contact with the droplet, the distance between the upper side of the flow cell and the bottom side of the prism was adjusted to within 300 μm. Utilizing the fact that a laser beam entering the parabolic prism with a distance from the optical axis above x_{crit} (compare Fig. 8A in the main text) caused several reflections because (i) media with subtle differences in refractive indices were penetrated (i. e. from quartz into immersion oil and from immersion oil into the glass substrate) and (ii) the illumination light was totally reflected at the glass-water interface and provided a measure to always position the prism at the correct height (Supporting Fig. 2). In fact, the latter reflex was the most intense and was used to position the focal spot at the

glass-water interface by finding the height at which it leaves the parabolic prism in parallel to the incoming laser beam.
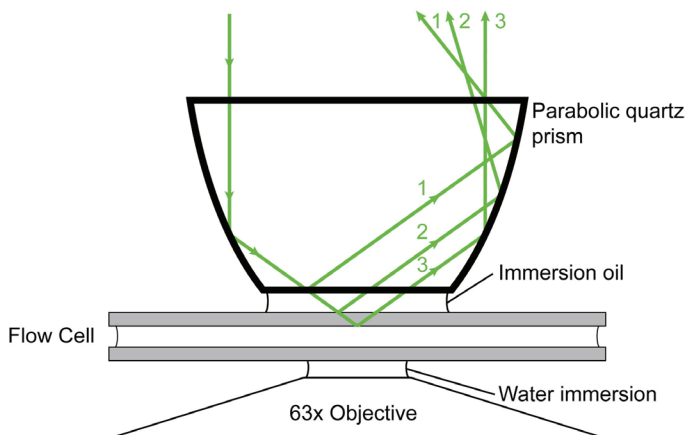

Supporting Fig. 2 | Alignment of the parabolic prism.
A laser beam entering the parabolic prism with a distance from the optical axis above x_{crit}, causes three different reflexes when passing from quartz into immersion oil (1), from immersion oil into the glass substrate (2), and when totally-reflected at the glass-water interface (3). As a consequence, all three beams leave the parabolic-prism with different angles, but the latter is strongest and leaves the prism vertically toward the top when the correct distance between prism surface and flow cell is kept.

A.3 Variation of the illuminated area

The size of the illumination area was varied using the adjustable fiber collimator to which the monomode glass fiber was coupled via a FC/PC connector. When the laser light was collimated, it yielded a minimal illumination area of 90 x 35 μm^2. The minimal illumination area was expected to depend on the focusing properties of the collimator in use. When defocusing the fiber collimator, the illumination area increased in size up to areas bigger than the 130 x 130 μm^2 camera chip, thereby yielding a homogenous illumination profile. 40 nm AuNPs (Fig. 8B in the main text) and fluorescently labeled streptavidin molecules (Supporting Fig. 3) were unspecifically attached to the substrate to image the obtainable illumination areas.
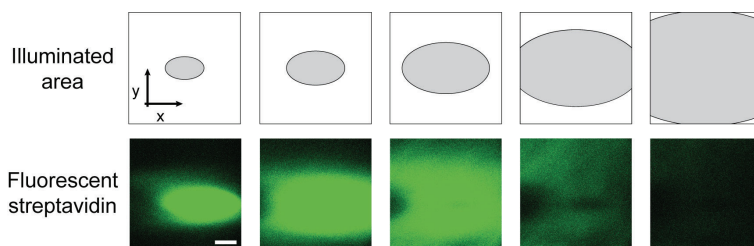
Supporting Fig. 3 | The size of the illumination area was varied by an adjustable fiber collimator.
Fluorescent streptavidin molecules unspecifically adsorbed to the substrate surface were illuminated with a 488 nm laser. The illumination area was increased from a minimal size of 90 x 35 μm² up to 130 x 130 μm² (left to right) stretching out to a homogenous illumination profile. Bar size: 25 μm.

A.4 Variation of the AOI

When the parabolic prism was placed at the correct distance from the flow cell, translational movement of the 90° mirror enabled the variation of the AOI. This was tested by measuring the influence of the AOI on the scattered intensity of surface-immobilized 40 nm AuNPs (compare Fig. 9 in the main text). The AOIs were measured by converting the horizontal displacement of the 90° mirror (which was measured accurately to within 0.1 mm yielding an angular error of 0.5° to 0.7°) using Eq. S3 and Eq. S4. The scattered intensity was fitted with the corresponding Fresnel equations for sub- and super-critical angle illumination yielding a critical angle of 63°. This compares to the theoretical value of the critical angle for a glass-water interface of $\text{ArcSin}(n_{\text{water}}/n_{\text{glass}}) = 61°$ assuming refractive indices of $n_{\text{water}} = 1.33$ and $n_{\text{glass}} = 1.52$ (see Gell et. al. [101] for an excellent discussion). The deviation from the theoretical value was due to (i) the uncertainty in the refractive indices of the used glass slides and the aqueous medium inside the flow cell and (ii) due to the imperfect angle measurement. A third contribution arose from a slight shift of the illumination spot along the *x*-axis (approximately 10 μm) when the AOI was varied from 45° to 72°. This movement did not play a significant role because the illumination spot was expanded to 130 x 130 μm². Shifting of the illumination spot was due to imperfections in the actual beam path, because the glass slides and immersion oil used did not have the same refractive index as the quartz prism itself. In case of quartz

cover slips as well as glycerol immersion, the illumination spot is expected to reside at a permanent position. In this case the shift is expected to be well below 10 μm. As calculated with Eq. S4, the AOIs accessible with prism-type TIR actually range from 45° to 72°. For dark-field illumination however, the NA of the objective being used for detection dictates the lower AOI limit and hence the lowest accessible AOI can be larger than 45°. For example, the water objective being used for detection here has an NA of 1.2. This corresponds to a maximum opening angle in water of $\alpha_{\text{det}} = 64.4°$, which, using Snell's law, converts into an angle inside the glass of $\alpha_{\text{glass}} = 52°$. This explains the lower limit of AOIs observed in Fig. 9 at around 50°, because illumination light is captured by the detection objective.

A.5 Noise and SNR depend on square root of amplitude

The noise present in the recorded streams was plotted versus the mean amplitude of the imaged molecules (Supporting Fig. 4A). Subsequently, the
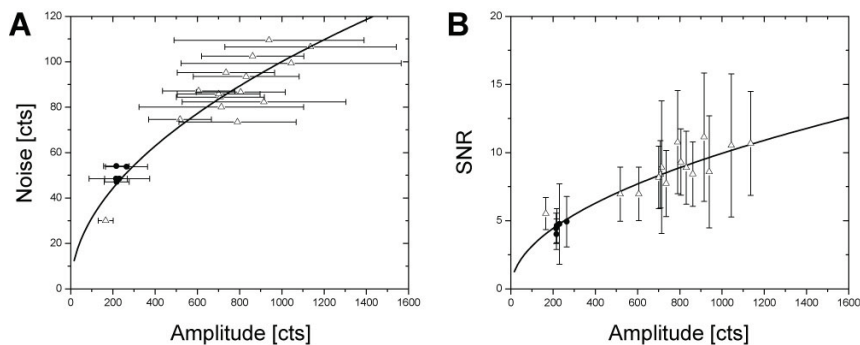
Supporting Fig. 4 | The noise level *b* and the SNR depended on the square root of the number of detected photons.

(A) The measured noise level is plotted versus the mean amplitude of the molecules (mean ± sd; dots – prism-type TIRF, triangles – objective-type TIRF). The data is fitted to a square-root relationship because a scaling factor of 0.5 was found when fitting the data to a weighted power function. (B) The SNRs (mean ± sd) obtained from the experiments were compared to the calculated SNRs using the square root dependency found in (A). Each data point averages over at least 70 (100) molecules for prism-type (objective-type) TIRF. Note the left-most triangle obtained with objective-type TIRF using a 4-fold lower illumination power (amplitude decreased by 4-fold) yielding a 2-fold lower SNR, reproducing SNRs typically obtained for prism-type TIRF.

data was fit to a power function $f(x) = y_0 + B \cdot x^C$, where y_0 describes an offset value, B correlates noise to amplitude, and C describes the exponent with which amplitude translates into noise. The offset value y_0 was found to equal zero within the error bars. The exponent C was found to be 0.51 ± 0.04 demonstrating a square-root dependency. The factor B was found to be 3.0 ± 0.8. Therefore, the data was well described by $Noise = 3\sqrt{Amplitude}$. Additionally the SNR was calculated based on the measured noise level and amplitudes of the molecules. The measured SNRs were compared to the calculated SNRs using the previous equation yielding $SNR = \frac{1}{3}\sqrt{Amplitude}$. This function was plotted in Supporting Fig. 4B and clearly fits the observed SNRs.

A.6 Dipole emission patterns near interfaces

The emission pattern of a dipole close to an optical interface (e. g. glass-water interface) is very different from the emission pattern in the free space [151]. This difference originates from the different refractive indices of water ($n_{water} = 1.33$) and glass ($n_{glass} = 1.52$). Light emitted by the dipole in very shallow angles with respect to the interface is refracted into the optically thicker medium (here the glass surface). As a consequence, shallow-angle-emission is bent toward the detection cone of a detection objective. This effect leads to a distortion of the 'free space' emission pattern toward the optically thicker interface (Supporting Fig. 5). The shallow-angle-emission is mainly collected along the critical angle for that interface favoring objective-type collection schemes because of the high NA objectives being able to collect that light. In contrast to that, prism-type collection schemes only harvest the minor part of the emission pattern being emitted toward the optically thinner medium (here the water medium).

The percentage of light being emitted into the half-space of the glass was estimated to be 72 % (28 % being emitted toward the half-space of water) using an excellent paper by Ruckstuhl et. al. [151]. This was tested directly by imaging 100 nm Tetraspeck beads adsorbed unspecifically to the upper and

lower glass surface within a flow cell. As the working distance of the TIRF objective is limited to approximately 170 µm a compressed flow cell, having a thickness of 20 µm, was used. For illumination and detection the aforementioned objectives were utilized and subsequently the ratio of mean intensities of Tetraspeck beads on the bottom and top surface was quantified.
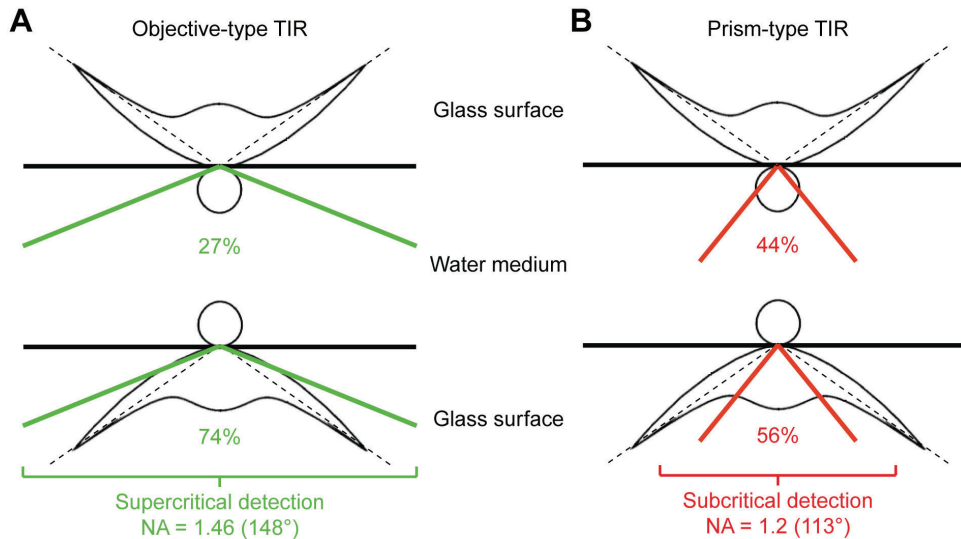
Supporting Fig. 5 | The emission pattern of a dipole close to an optical interface.
The larger refractive index of glass (n_{glass} = 1.52) compared to water (n_{water} = 1.33) causes enhanced emission toward the optically denser medium. This effect favors objective-type over prism-type collection schemes in terms of detection efficiency. (A) In the objective-type case 2.7 times (74 % ÷ 27 %) more photons are being collected from the bottom surface compared to the upper surface. (B) In the prism-type case, only 1.3 times (56 % ÷ 44 %) more photons are being collected from the bottom surface compared to the upper surface.

In the case of using the TIRF objective, the beads on the bottom surface showed a mean intensity a factor of 2.7 ± 0.2 (mean ± sem, N = 146) times higher compared to the beads on the upper surface. This gives rise to a 2.7 times higher probability for photons to be emitted toward the glass slide compared to the probability to be emitted toward the water medium. Hence, a fraction of 74 % of the photons was emitted toward the glass interface, which is in close agreement with the estimation mentioned above. Accordingly, the remaining fraction of photons emitted toward the water medium was 26 %. The ratio of these two probabilities directly reflects a factor of three times

more photons being collected using objective-type TIRF compared to prism-type TIRF. For the case of the water objective an intensity ration of 1.27 ± 0.04 (mean ± sem, N = 550) was measured. Here, this corresponded to a fraction of photons emitted toward the glass interface of 56 % compared to 44 % of the photons being emitted toward the water medium. Thus, the impact of surface enhanced emission becomes evident primarily for high NA objectives.

A.7 AuNPs report on subtle details of the motor trajectory

To acquire a picture of the normal, uninfluenced motor movement, the transport of AuNPs was studied in absence of roadblocks. The trajectories of AuNP-motors were obtained from FIESTA tracking software and were projected onto the MT centerline, yielding (i) the distance along the path for movement parallel to the MT and (ii) the side distance for movement perpendicular to the MT centerline. The AuNP events were classified into the steadily moving, a stop-and-go (stopping, starting, and pausing) and a non-classified event group. In this appendix section, an overview of trajectories will be provided. Besides the two dominant classes of nicely moving and stop-and-go, an unexpected richness in detail was observed in some of the trajectories. Three such example traces will be presented here, which provide a clearer picture on how manifold the movement of an AuNP-motor in the nano-world can be. Furthermore, insights into the mechanical arrangement of the AuNP and the motor tail can be obtained from such 'abnormal' events.

The majority of AuNP-motors move steadily along MTs

In absence of roadblocks, the majority of particles (51 %, compare Fig. 24 in the main text) moved linearly along the MTs, without showing intermittent pausing (Supporting Fig. 6A). For such events, the AuNP-motor progressed steadily along the MT centerline. The mean velocity of steadily moving AuNP events was determined to 829 ± 91 nm/s (mean ± sd, N = 31). Interestingly, it was found that 30 % of the AuNP-motors moved with an angle relative to the MT centerline (red-lined wedge in Supporting Fig. 6A, left and

right graph). This is indication that the surface-bound MTs showed variations in the number of PFs.
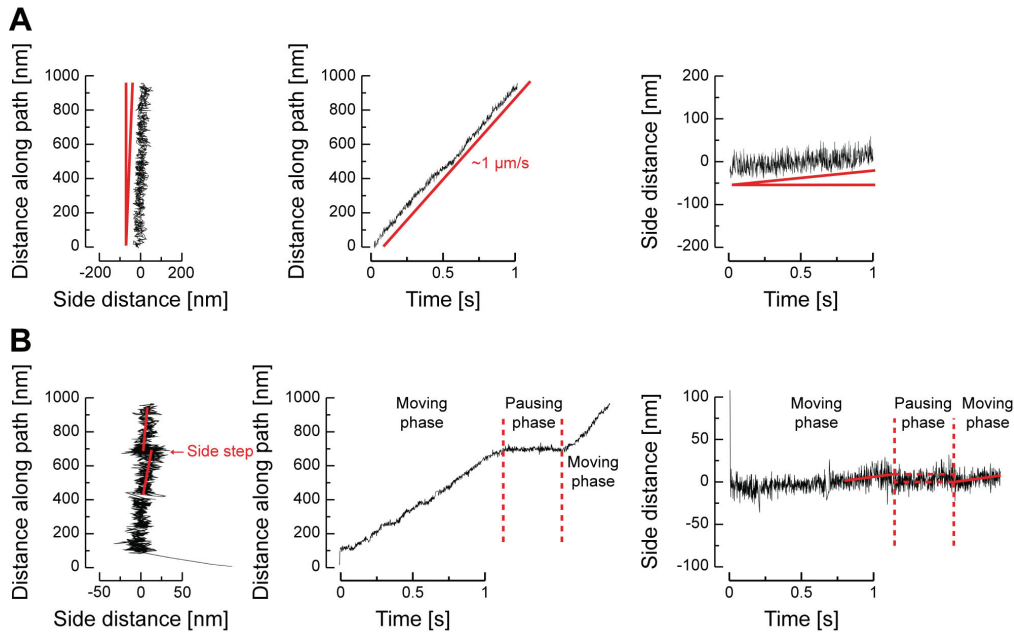
Supporting Fig. 6 | Examples of a typical moving and pausing event.
(A) A typical moving event shows purely straight movement along the MT centerline (left), a slope of approximately $1\,\mu m/s$ in the time-distance plot (middle), and little sideways deviation over time (right). (B) A typical pausing event is identified by a slub in the distribution of the AuNP positions along the MT path (left, arrow). The trajectories before and after the pause were fitted to a linear path (red lines) revealing a clear offset, which indicated a side-shift. The moving and pausing phases were distinguishable in a time-distance plot (middle) where the AuNP moved with a velocity of 600 nm/s initially, then showed a pause for 0.5 seconds, and finally continued the run with a velocity of 1000 nm/s. The side distance before and after the pausing phase (right, compare horizontally dashed lines) is shifted toward the left by -7.6 ± 3.6 nm (mean ± sd, $N_{before} = 354$ data points before and $N_{after} = 317$ data points after the pause).

AuNP-motors show pauses even in the absence of roadblocks

Surprisingly, a large number (41 %, compare Fig. 24 in the main text) of stop-and-go events were detected in absence of roadblocks. Typically, pausing events were identified by inhomogeneities in the distribution of the AuNP positions along the MT (Supporting Fig. 6B, left, arrow). During the pausing period, the AuNP-motor is not moving and consequently contributes a larger number of data points to this position in contrast to a moving AuNP-motor.

This enhanced residence time results in a larger spread of the AuNP position at this position, which finally leads to the observed inhomogeneity. Pauses were identified in time-distance plots as horizontal plateaus, which depict periods of no net AuNP movement (Supporting Fig. 6B, middle). To identify shifts in the side distance, the trajectories right before and after the pause were fitted to a linear path. From the fit, the side distance at the beginning and the end of the pause were determined. The size of a side-shift was calculated from the difference in these two side distances. A negative sign corresponds to a shift toward the left, defined relative to the direction of the AuNP movement. The event described in Supporting Fig. 6B is unique in the sense, that the side distance changes at the beginning of the pause. The vast majority of AuNP events showed a side-shift only at the end of the pause.

AuNP-motors showed occasional jumps along the MT

One remarkable example of an unexpected AuNP event is presented in Supporting Fig. 7. This motor moved normally along the MT for up to 1.5 seconds, but then performed a sudden 500 nm backward jump. This was identified by an overlap of the AuNP positions along the MT centerline and a sharp vertical transition in the time-distance plot (Supporting Fig. 7, left and middle). The transition takes place within 3 ms, which can be explained by thermal diffusion[*]. Such re-binding events were observed in 13 % of all AuNP events in absence of roadblocks (56 % at 2 nM and 37 % at 4 nM roadblocks, respectively) and are thought to provide a simple pathway to re-attach to the MT. As outlined before, the large AuNP label may increase the re-binding probability to the MT lattice and it would be hypothesized that larger labels provide even higher rebinding probabilities. This also explains the bias of AuNP-motors to show slightly longer dwell times as well as run lengths compared to GFP-motors. This event showed large amplitude in the side

---

[*]According to the one-dimensional diffusion equation $<x^2> = 2Dt$, diffusion of 500 nm would take approximately 10 ms, assuming a diffusion constant of the AuNP of 10 μm^2/s (compare Table 2, page 27).

distance fluctuation, which made the identification of a significant side-shift impossible (Supporting Fig. 7, right).
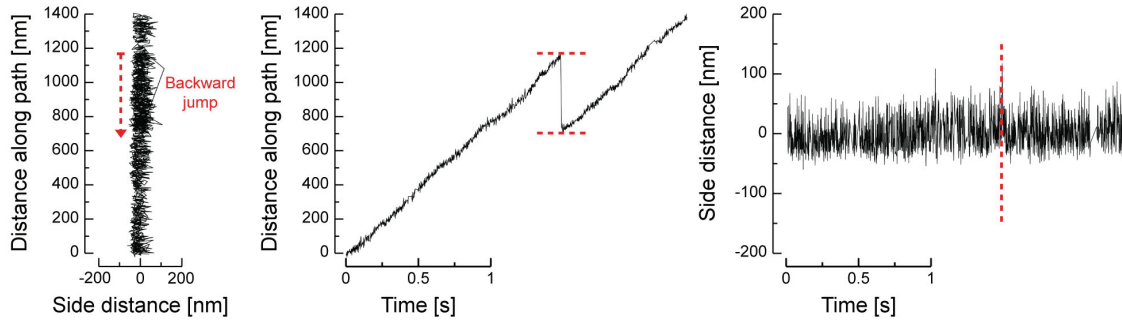
Supporting Fig. 7 | Example of a AuNP-motor jumping along the MT track.
A jumping event was identified by overlapping AuNP positions along the MT centerline (left, dashed arrow). In the time-distance plot a 500 nm jump appeared by a vertical transition from 1200 nm back to 700 nm (middle, dashed lines). Because the side distance fluctuation was large (right), no significant change was detected before and after the jump (right, transitions indicated by dashed line).

AuNP-motors switch PFs without pausing

Another unexpected event, classified into the nicely moving class, showed an AuNP-motor that switched the PF without exhibiting a pausing phase (Supporting Fig. 8). The sudden transition in the side distance, takes place within one frame (1 ms).
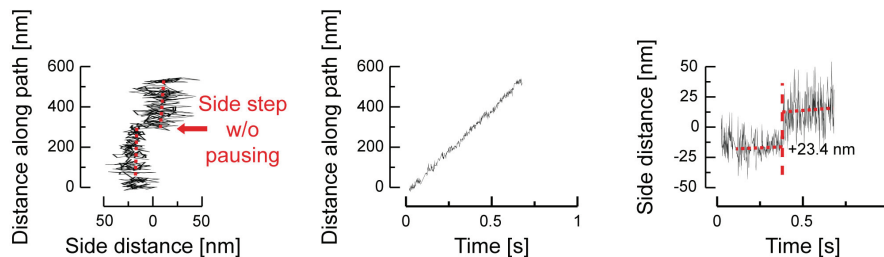
Supporting Fig. 8 | Example of a AuNP-motors switching PFs without pausing.
A PF-switching event is identified by a sudden side-shift of the AuNP positions along the MT centerline (left, compare dashed lines and red arrow). The AuNP moved normally with a velocity of 800 nm/s without showing a distinct pausing phase (middle). The side distance plot showed a distinct jump toward the right by +23.4 ± 5.2 nm.

Such switches were observed in 25 % of all motor trajectories, providing evidence, that the PF-tracking mechanism of kinesin-1 is not ultimately strict. The diffusion of the AuNP-motor to the binding site of the adjacent PF is expected to occur much faster[*] than the 1 ms acquisition time provided here.

AuNP-motors showed variations in side distance fluctuation

A last remarkable AuNP-motor event provides insight into the mechanical arrangement of the AuNP label and the motor tail. This AuNP-motor, showed several side-shifts while moving along the MT for up to 1.5 μm (Supporting Fig. 9A). Connected to the side-shifts, a significant change in the amplitude of the side distance fluctuation was observed (Supporting Fig. 9B).
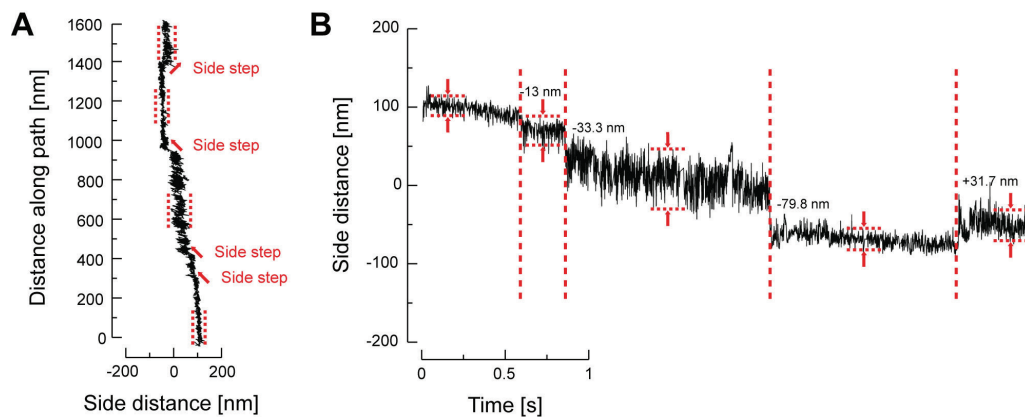
Supporting Fig. 9 | The side distance fluctuation varied with distance from the MT centerline.
(A) The trajectory of this AuNP-motor showed four side-shifts during the run (left, indicated by the arrows) in conjunction with a marked change in the amplitude of the side distance fluctuation (indicated by the dashed lines). (B) The change in side distance fluctuation coincides with the side-shift (indicated by vertical dashed lines) and changes from small amplitude on the far right and left side of the MT, to large amplitude on top of the MT. The size of each side-shift is given at the transition point.

---

[*]According to the one-dimensional diffusion equation $<x^2> = 2Dt$, the diffusion to an adjacent PF would take approximately 2 μs, assuming a diffusion constant D of the AuNP of 10 μm^2/s (compare Table 2, page 27).

The amplitude was minimal when the AuNP was located on the far right side, then increased when the AuNP was moving closer to the middle, and finally decreased again when the AuNP moved to the far left side of the MT centerline. A last side-shift back toward the middle of the MT was connected with another increase in amplitude. This observation suggests that the AuNP, being flexibly tethered to the motor tail, exhibits restricted diffusion when held close to the substrate-surface. Accordingly, when the motor is attached to a PF on the side of the MT, the tethered AuNP explores a spatially restricted volume bounded by the MT and the glass-substrate. In contrast, when the motor is attached to a PF on the top of the MT, the tethered AuNP can freely explore the volume around the MT without spatial constraints. This mechanism, together with a potential bending/stiffening of the tail when the motor is bound to a lateral PF, is thought to cause the variation in the side distance fluctuation.

Moreover, this event allows estimating the number of PFs available for the AuNP-motor. From a geometrical point of view, the size of the AuNP label, only allows the top half of the MT to be available for transport. The PFs positioned on the bottom half of the MT are only accessible if the motor tail is allowed to bend so that the motor can reach underneath the MT. Thus, the observation of the five distinct fluctuation regimes in Supporting Fig. 9B (dashed lines) is evidence for such a low number of available PFs. The different absolute sizes of the oppositely oriented third and fourth side-shift (-79.8 nm versus +31.7 nm) in Supporting Fig. 9B indicated that two PFs could be bridged at once. As a consequence, a total of 6 PFs might be present in this example trace, which agrees with the assumption that the top half of the MT is accessible by the AuNP-motors.

Interestingly, the total distance between the far right and the far left position was determined to approximately 160 nm and is in agreement with the expected total length of the AuNP-motor of approximately 65 nm[*]. Thus, when the motor is bound on the side of the MT, the particle can reach out by

---

[*]Assuming a total length of the kinesin-1 motor of 30 nm, GFP domain, GFP antibody, and streptavidin with about 5 nm, and a radius of the AuNP of 20 nm.

approximately 80 nm (65 nm AuNP + 12.5 nm MT radius) on either side of the MT. This crude estimation is evidence for the AuNP-motor being in a rather stretched orientation when bound to a lateral PF.

Notably, the trajectories discuss in this section were captured in absence of roadblocks. The surprisingly rich behavior of the single-motor events occurred unexpectedly at this stage of the experiments. However, these events provide a clearer picture of the multi-lane environment in which kinesin-1 transport takes place.

References

[1]   E. Schrödinger, *What is life? The physical aspect of the living cell.*, 1st ed., p. 194, Cambridge University Press (1944).

[2]   P. Schwille and S. Diez, "Synthetic biology of minimal systems," *Critical Reviews in Biochemistry and Molecular Biology* **44**, 223–242 (2009).

[3]   E. Neher and B. Sakmann, "Single-channel currents recorded from membrane of devervated frog muscle fibers," *Nature* **260**, 799–802 (1976).

[4]   F. G. Prendergast and K. G. Mann, "Chemical and physical properties of aequorin and the green fluorescent protein isolated from Aequorea forskalea," *Biochemistry* **17**, 3448–3453 (1978).

[5]   I. Newton, *Opticks - Or a treatise of the reflections, refractions, inflections and colours of light*, 4th ed., p. 414, London, William Innys (1730).

[6]   D. Axelrod, "Cell-substrate contacts illuminated by total internal reflection fluorescence," *Journal of Cell Biology* **89**, 141–145 (1981).

[7]   W. Boyle and G. Smith, "Charge coupled semiconductor devices," *Bell System Technical Journal* **49**, 587–593 (1970).

[8]   P. Schwille, "Freedom is the greatest gift," in *Innovation - The Magazine from Carl Zeiss*, 25th ed., D. Brocksch and S. Schmid, Eds., pp. 22–23, Innovation - Das Magazin von Carl Zeiss, Oberkochen, Germany (2010).

[9]   T. Funatsu, Y. Harada, M. Tokunaga, K. Saito, and T. Yanagida, "Imaging of single fluorescent molecules and individual ATP turnovers by single myosin molecules in aqueous solution," *Nature* **374**, 555–559 (1995).

[10]   R. D. Vale, T. Funatsu, D. W. Pierce, L. Romberg, Y. Harada, and T. Yanagida, "Direct observation of single kinesin molecules moving along microtubules," *Nature* **380**, 451–453 (1996).

[11]   A. Hendricks, E. Perlson, J. Ross, H. Schroeder, M. Tokito, and E. Holzbaur, "Motor coordination via a tug-of-war mechanism drives bidirectional vesicle transport," *Current Biology* **20**, 697–702 (2010).

[12] R. Dixit, J. L. Ross, Y. E. Goldman, and E. L. F. Holzbaur, "Differential regulation of dynein and kinesin motor proteins by tau," *Science Signalling* **319**, 1086–1089 (2008).

[13] T. L. Blasius, D. Cai, G. T. Jih, C. P. Toret, and K. J. Verhey, "Two binding partners cooperate to activate the molecular motor kinesin-1," *Journal of Cell Biology* **176**, 11–17 (2007).

[14] E. Chevalier-Larsen and E. L. F. Holzbaur, "Axonal transport and neurodegenerative disease," *Biochimica et Biophysica Acta (BBA)-Molecular Basis of Disease* **1762**, 1094–1108 (2006).

[15] G. B. Stokin and L. S. B. Goldstein, "Axonal transport and Alzheimer's disease," *Annual Review of Biochemistry* **75**, 607–627 (2006).

[16] I. A. Telley, P. Bieling, and T. Surrey, "Obstacles on the microtubule reduce the processivity of Kinesin-1 in a minimal in vitro system and in cell extract," *Biophysical Journal* **96**, 3341–3353 (2009).

[17] T. Korten and S. Diez, "Setting up roadblocks for kinesin-1: mechanism for the selective speed control of cargo carrying microtubules," *Lab on a Chip* **8**, 1441–1447 (2008).

[18] S. T. Brady, R. J. Lasek, and R. D. Allen, "Fast axonal transport in extruded axoplasm from squid giant axon," *Science* **218**, 1129–1131 (1982).

[19] J. Howard, A. Hudspeth, and R. Vale, "Movement of microtubules by single kinesin molecules," *Nature* **342**, 154–158 (1989).

[20] B. Lewin, L. Cassimeris, V. Lingappa, and G. Plopper, *Cells*, 1st ed., Jones and Bartlett Publishers Inc. (2007).

[21] R. D. Vale, T. S. Reese, and M. P. Sheetz, "Identification of a novel force-generating protein, kinesin, involved in microtubule-based motility," *Cell* **42**, 39–50 (1985).

[22] E. Nogales, S. G. Wolf, I. A. Khan, R. F. Ludueña, and K. H. Downing, "Structure of tubulin at 6.5 Å and location of the taxol-binding site," *Nature* **375**, 424–427 (1995).

[23] R. Wade, D. Chrétien, and D. Job, "Characterization of microtubule protofilament numbers: How does the surface lattice accommodate?," *Journal of Molecular Biology* **212**, 775–786 (1990).

[24] J. van Mameren, K. C. Vermeulen, F. Gittes, and C. F. Schmidt, "Leveraging single protein polymers to measure flexural rigidity," *The Journal of Physical Chemistry B* **113**, 3837–3844 (2009).

[25]   P. Schiff, J. Fant, and S. Horwitz, "Promotion of microtubule assembly in vitro by taxol," *Nature* **277**, 665–667 (1979).

[26]   C. V. Sindelar and K. H. Downing, "The beginning of kinesin's force-generating cycle visualized at 9-Å resolution," *Journal of Cell Biology* **177**, 377–385 (2007).

[27]   S. Rice, A. W. Lin, D. Safer, C. L. Hart, N. Naber, B. O. Carragher, S. M. Cain, E. Pechatnikova, E. M. Wilson-Kubalek, et al., "A structural change in the kinesin motor protein that drives motility," *Nature* **402**, 778–784 (1999).

[28]   K. Rogers, S. Weiss, I. Crevel, P. Brophy, M. Geeves, and R. Cross, "KIF1D is a fast non-processive kinesin that demonstrates novel K-loop-dependent mechanochemistry," *EMBO Journal* **20**, 5101–5113 (2001).

[29]   W. Jiang, M. Stock, X. Li, and D. Hackney, "Influence of the kinesin neck domain on dimerization and ATPase kinetics," *Journal of Biological Chemistry* **272**, 7626–7632 (1997).

[30]   G. Woehlke and M. Schliwa, "Walking on two heads: the many talents of kinesin," *Nat Rev Mol Cell Biol* **1**, 50–58 (2000).

[31]   D. Friedman and R. Vale, "Single-molecule analysis of kinesin motility reveals regulation by the cargo-binding tail domain," *Nature cell biology* **1**, 293–297 (1999).

[32]   H. Y. K. Kaan, D. D. Hackney, and F. Kozielski, "The Structure of the Kinesin-1 Motor-Tail Complex Reveals the Mechanism of Autoinhibition," *Science* **333**, 883 (2011).

[33]   C. Leduc, F. Ruhnow, J. Howard, and S. Diez, "Detection of fractional steps in cargo movement by the collective operation of kinesin-1 motors," *Proceedings of the National Academy of Sciences* **104**, 10847–10852 (2007).

[34]   B. Nitzsche, F. Ruhnow, and S. Diez, "Quantum-dot-assisted characterization of microtubule rotations during cargo transport," *Nature Nanotechnology* **3**, 552–556 (2008).

[35]   S. T. Brady, K. K. Pfister, and G. S. Bloom, "A monoclonal antibody against kinesin inhibits both anterograde and retrograde fast axonal transport in squid axoplasm," *Proceedings of the National Academy of Sciences* **87**, 1061–1065 (1990).

[36]   G. T. Shubeita, S. L. Tran, J. Xu, M. Vershinin, S. Cermelli, S. L. Cotton, M. A. Welte, and S. P. Gross, "Consequences of motor copy number on the intracellular transport of kinesin-1-driven lipid droplets," *Cell* **135**, 1098–1107 (2008).

[37]   S. Ray, E. Meyhofer, R. A. Milligan, and J. Howard, "Kinesin follows the microtubule's protofilament axis," *Journal of Cell Biology* **121**, 1083–1093 (1993).

[38]   A. Yildiz, M. Tomishige, A. Gennerich, and R. D. Vale, "Intramolecular strain coordinates kinesin stepping behavior along microtubules," *Cell* **134**, 1030–1041 (2008).

[39]   K. Kawaguchi, "Energetics of kinesin-1 stepping mechanism," *FEBS letters* **582**, 3719–3722 (2008).

[40]   A. Yildiz, M. Tomishige, R. D. Vale, and P. R. Selvin, "Kinesin walks hand-over-hand," *Science* **303**, 676–678 (2004).

[41]   W. O. Hancock and J. Howard, "Kinesin's processivity results from mechanical and chemical coordination between the ATP hydrolysis cycles of the two motor domains," *Proceedings of the National Academy of Sciences* **96**, 13147–13152 (1999).

[42]   J. E. Walker, M. Saraste, M. J. Runswick, and N. J. Gay, "Distantly related sequences in the alpha-and beta-subunits of ATP synthase, myosin, kinases and other ATP-requiring enzymes and a common nucleotide binding fold," *The EMBO Journal* **1**, 945–951 (1982).

[43]   T. Nakata and N. Hirokawa, "Point mutation of adenosine triphosphate-binding motif generated rigor kinesin that selectively blocks anterograde lysosome membrane-transport," *Journal of Cell Biology* **131**, 1039–1053 (1995).

[44]   R. Murphey, P. Caruccio, M. Getzinger, P. Westgate, and R. Phillis, "Dynein–dynactin function and sensory axon growth during drosophila metamorphosis: A role for retrograde motors," *Developmental biology* **209**, 86–97 (1999).

[45]   W. M. Saxton, J. Hicks, L. S. B. Goldstein, and E. C. Raff, "Kinesin heavy chain is essential for viability and neuromuscular functions in Drosophila, but mutants show no defects in mitosis," *Cell* **64**, 1093–1102 (1991).

[46]   D. D. Hurd and W. M. Saxton, "Kinesin mutations cause motor neuron disease phenotypes by disrupting fast axonal transport in Drosophila," *Genetics* **144**, 1075–1085 (1996).

[47]   N. Hirokawa, "Organelle transport along microtubules - The role of KIFs," *Trends in Cell Biology* **6**, 135–141 (1996).

[48]   L. Wang, C. Ho, D. Sun, R. Liem, and A. Brown, "Rapid movement of axonal neurofilaments interrupted by prolonged pauses," *Nature cell biology* **2**, 137–141 (2000).

[49]   M. Trabucchi, "An economic perspective on Alzheimer's disease," *Journal of geriatric psychiatry and neurology* **12**, 29–38 (1999).

[50]   P. W. Baas and L. Qiang, "Neuronal microtubules: when the MAP is the roadblock," *Trends in Cell Biology* **15**, 183–187 (2005).

[51]   D. G. Drubin and M. W. Kirschner, "Tau protein function in living cells," *Journal of Cell Biology* **103**, 2739–2746 (1986).

[52]   A. Ebneth, R. Godemann, K. Stamer, S. Illenberger, B. Trinczek, E.-M. Mandelkow, and E. Mandelkow, "Overexpression of tau protein inhibits kinesin-dependent trafficking of vesicles, mitochondria, and endoplasmic reticulum: implications for Alzheimer's disease," *Journal of Cell Biology* **143**, 777–794 (1998).

[53]   B. Trinczek, A. Ebneth, E. Mandelkow, and E. Mandelkow, "Tau regulates the attachment/detachment but not the speed of motors in microtubule-dependent transport of single vesicles and organelles," *Journal of Cell Science* **112**, 2355–2367 (1999).

[54]   K. Stamer, R. Vogel, E. Thies, E. Mandelkow, and E. Mandelkow, "Tau blocks traffic of organelles, neurofilaments, and APP vesicles in neurons and enhances oxidative stress," *Journal of Cell Biology* **156**, 1051–1063 (2002).

[55]   A. Seitz, H. Kojima, K. Oiwa, E. Mandelkow, Y. Song, and E. Mandelkow, "Single-molecule investigation of the interference between kinesin, tau and MAP2c," *EMBO Journal* **21**, 4896–4905 (2002).

[56]   E.-M. Mandelkow, E. Thies, B. Trinczek, J. Biernat, and E. Mandelkow, "MARK/PAR1 kinase is a regulator of microtubule-dependent transport in axons," *Journal of Cell Biology* **167**, 99–110 (2004).

[57]   F. J. Ahmad, W. Yu, F. J. McNally, and P. W. Baas, "An essential role for katanin in severing microtubules in the neuron," *Journal of Cell Biology* **145**, 305–315 (1999).

[58]   S. B. Prusiner, "A unifying role for prions in neurodegenerative diseases," *Science* **336**, 1511–1513 (2012).

[59] J. Gelles, B. J. Schnapp, and M. P. Sheetz, "Tracking kinesin-driven movements with nanometre-scale precision," *Nature* **331**, 450–453 (1988).

[60] T. Korten, B. Nitzsche, C. Gell, F. Ruhnow, C. Leduc, and S. Diez, "Fluorescence imaging of single kinesin motors on immobilized microtubules.," *Methods in Molecular Biology* **783**, 121–137 (2011).

[61] C. Gell, V. Bormuth, G. J. Brouhard, D. N. Cohen, S. Diez, C. T. Friel, J. Helenius, B. Nitzsche, H. Petzold, et al., "Microtubule dynamics reconstituted in vitro and imaged by single-molecule fluorescence microscopy," *Methods in Cell Biology* **95**, 221–245 (2010).

[62] M. Vershinin, B. C. Carter, D. S. Razafsky, S. J. King, and S. P. Gross, "Multiple-motor based transport and its regulation by Tau," *Proceedings of the National Academy of Sciences* **104**, 87–92 (2007).

[63] K. Dreblow, N. Kalchishkova, and K. J. Böhm, "Kinesin passing permanent blockages along its protofilament track," *Biochemical and Biophysical Research Communications* **395**, 490–495 (2010).

[64] C. Leduc, K. Padberg-Gehle, V. Varga, D. Helbing, S. Diez, and J. Howard, "Molecular crowding creates traffic jams of kinesin motors on microtubules," *Proceedings of the National Academy of Sciences* **109**, 6100–6105 (2012).

[65] A. Seitz and T. Surrey, "Processive movement of single kinesins on crowded microtubules visualized using quantum dots," *The EMBO Journal* **25**, 267–277 (2006).

[66] I. M.-T. Crevel, M. Nyitrai, M. C. Alonso, S. Weiss, M. A. Geeves, and R. A. Cross, "What kinesin does at roadblocks: the coordination mechanism for molecular walking," *The EMBO Journal* **23**, 23–32 (2004).

[67] T. V. Korten, *How kinesin-1 deals with roadblocks: Biophysical description and nanotechnological application*, S. Diez, Ed., pp. 1–120, PhD thesis (2009).

[68] V. Bormuth, B. Nitzsche, F. Ruhnow, A. Mitra, M. Storch, B. Rammner, J. Howard, and S. Diez, "The highly processive kinesin-8, kip3, switches microtubule protofilaments with a bias toward the left," *Biophysical Journal* **103**, L04–L06 (2012).

[69] M. Brunnbauer, R. Dombi, T. H. Ho, M. Schliwa, M. Rief, and Z. Ökten, "Torque generation of kinesin motors is governed by the stability of the neck domain," *Molecular Cell* **46**, 147–158 (2012).

[70]   E. Mandelkow and E. Mandelkow, "Biochemistry and cell biology of tau protein in neurofibrillary degeneration," *Cold Spring Harbor Perspectives in Medicine* **2**, 1–25 (2012).

[71]   R. A. Santarella, G. Skiniotis, K. N. Goldie, P. Tittmann, H. Gross, E.-M. Mandelkow, E. Mandelkow, and A. Hoenger, "Surface-decoration of microtubules by human tau," *Journal of Molecular Biology* **339**, 539–553 (2004).

[72]   D. K. Jamison, J. W. Driver, A. R. Rogers, P. E. Constantinou, and M. R. Diehl, "Two kinesins transport cargo primarily via the action of one motor: implications for intracellular transport," *Biophysical Journal* **99**, 2967–2977 (2010).

[73]   D. Axelrod, "Total internal reflection fluorescence microscopy in cell biology," *Traffic* **2**, 764–774 (2001).

[74]   R. M. Fulbright and D. Axelrod, "Dynamics of nonspecific adsorption of insulin to erythrocyte membranes," *Journal of Fluorescence* **3**, 1–16 (1993).

[75]   U. Resch-Genger, M. Grabolle, S. Cavaliere-Jaricot, R. Nitschke, and T. Nann, "Quantum dots versus organic dyes as fluorescent labels," *Nature Methods* **5**, 763–775 (2008).

[76]   C. Joo, H. Balci, Y. Ishitsuka, C. Buranachai, and T. Ha, "Advances in single-molecule fluorescence methods for molecular biology," *Annual Review of Biochemistry* **77**, 51–76 (2008).

[77]   X. Wang, X. Ren, K. Kahen, M. A. Hahn, M. Rajeswaran, S. Maccagnano-Zacher, J. Silcox, G. E. Cragg, A. L. Efros, et al., "Non-blinking semiconductor nanocrystals," *Nature* **459**, 686–689 (2009).

[78]   A. Yildiz and P. R. Selvin, "Fluorescence imaging with one nanometer accuracy: application to molecular motors," *Accounts of chemical research* **38**, 574–582 (2005).

[79]   M. Van Dijk, A. Tchebotareva, M. Orrit, M. Lippitz, S. Berciaud, D. Lasne, L. Cognet, and B. Lounis, "Absorption and scattering microscopy of single metal nanoparticles," *Physical Chemistry Chemical Physics* **8**, 3486–3495 (2006).

[80]   J. Yguerabide and E. E. Yguerabide, "Light-scattering submicroscopic particles as highly fluorescent analogs and their use as tracer labels in clinical and biological applications: I. Theory," *Analytical biochemistry* **262**, 137–156 (1998).

[81]   J. Yguerabide and E. E. Yguerabide, "Light-scattering submicroscopic particles as highly fluorescent analogs and their use as tracer labels in clinical and biological applications: II. Experimental characterization," *Analytical biochemistry* **262**, 157–176 (1998).

[82]   A. R. Dunn and J. A. Spudich, "Dynamics of the unbound head during myosin V processive translocation," *Nature structural & molecular biology* **14**, 246–248 (2007).

[83]   G. Mie, "Beiträge zur Optik trüber Medien, speziell kolloidaler Metallösungen," *Annalen der Physik* **330**, 377–445 (1908).

[84]   U. Kubitscheck, O. Kuckmann, T. Kues, and R. Peters, "Imaging and tracking of single GFP molecules in solution," *Biophysical Journal* **78**, 2170–2179 (2000).

[85]   R. Swaminathan, C. Hoang, and A. Verkman, "Photobleaching recovery and anisotropy decay of green fluorescent protein GFP-S65T in solution and cells: Cytoplasmic viscosity probed by green fluorescent protein translational and rotational diffusion," *Biophysical Journal* **72**, 1900–1907 (1997).

[86]   R. Y. Tsien, "The green fluorescent protein," *Annual Review of Biochemistry* **67**, 509–544 (1998).

[87]   J. Howard, *Mechanics of motor proteins and the cytoskeleton*, 1st ed., p. 367, Sinauer Associates Inc (2001).

[88]   S. Nishikawa, I. Arimoto, K. Ikezaki, M. Sugawa, H. Ueno, T. Komori, A. H. Iwane, and T. Yanagida, "Switch between large hand-over-hand and small inchworm-like steps in myosin VI," *Cell* **142**, 879–888 (2010).

[89]   M. van't Hoff, M. Reuter, D. T. F. Dryden, and M. Oheim, "Screening by imaging: scaling up single-DNA-molecule analysis with a novel parabolic VA-TIRF reflector and noise-reduction techniques," *Physical Chemistry Chemical Physics* **11**, 7713–7720 (2009).

[90]   S. Diez, R. Schneider, T. Glaser, B. Venus, and M. Berndt, "Verfahren und Vorrichtung zur Weitfeld-Mikroskopie," German patent application no.: 10 2011 053 003.7.

[91]   D. Axelrod, T. P. Burghardt, and N. L. Thompson, "Total internal reflection fluorescence," *Annual review of biophysics and bioengineering* **13**, 247–268 (1984).

[92]   H. Schneckenburger, "Total internal reflection fluorescence microscopy: technical innovations and novel applications," *Current opinion in biotechnology* **16**, 13 (2005).

[93]   T. Ruckstuhl, M. Rankl, and S. Seeger, "Confocal TIRF microscopy of single molecules," *Manipulation and Analysis of Biomolecules, Cells, and Tissues, Proceedings of SPIE* **4962**, 126–134 (2003).

[94]   T. Ruckstuhl and S. Seeger, "Confocal total-internal-reflection fluorescence microscopy with a high-aperture parabolic mirror lens," *Applied Optics* **42**, 3277–3283 (2003).

[95]   T. Ruckstuhl and S. Seeger, "Attoliter detection volumes by confocal total-internal-reflection fluorescence microscopy," *Optics Letters* **29**, 569–571 (2004).

[96]   H. Välimäki and K. Tappura, "A novel platform for highly surface-sensitive fluorescent measurements applying simultaneous total internal reflection excitation and super critical angle detection," *Chemical Physics Letters* **473**, 358–362 (2009).

[97]   C. M. Winterflood, T. Ruckstuhl, D. Verdes, and S. Seeger, "Nanometer axial resolution by three-dimensional supercritical angle fluorescence microscopy," *Physical review letters* **105**, 108103 (2010).

[98]   E. Lassila, T. Alahautala, and R. Hernberg, "Focusing diode lasers using a truncated paraboloid with spherical output surface," *Optical Engineering* **46**, 054301–054301–5 (2007).

[99]   R. Fiolka, Y. Belyaev, H. Ewers, and A. Stemmer, "Even illumination in total internal reflection fluorescence microscopy using laser light," *Microscopy Research and Technique* **71**, 45–50 (2008).

[100]   A. L. Mattheyses, K. Shaw, and D. Axelrod, "Effective elimination of laser interference fringing in fluorescence microscopy by spinning azimuthal incidence angle," *Microscopy Research and Technique* **69**, 642–647 (2006).

[101]   C. Gell, M. Berndt, J. Enderlein, and S. Diez, "TIRF microscopy evanescent field calibration using tilted fluorescent microtubules," *Journal of Microscopy* **234**, 38–46 (2009).

[102]   W. P. Ambrose, P. M. Goodwin, and J. P. Nolan, "Single-molecule detection with total internal reflection excitation: Comparing signal-to-background and total signals in different geometries," *Cytometry* **36**, 224–231 (1999).

[103]   S. Verbrugge, S. M. J. L. Van den Wildenberg, and E. J. G. Peterman, "Novel ways to determine kinesin-1's run length and randomness using fluorescence microscopy," *Biophysical Journal* **97**, 2287–2294 (2009).

[104]   G. I. Mashanov, D. Tacon, M. Peckham, and J. E. Molloy, "The spatial and temporal dynamics of pleckstrin homology domain binding at the plasma membrane measured by imaging single molecules in live mouse myoblasts," *Journal of Biological Chemistry* **279**, 15274–15280 (2004).

[105]   J. Enderlein and T. Ruckstuhl, "The efficiency of surface-plasmon coupled emission for sensitive fluorescence detection," *Optics Express* **13**, 8855–8865 (2005).

[106]   F. Ruhnow, D. Zwicker, and S. Diez, "Tracking single particles and elongated filaments with nanometer precision," *Biophysical Journal* **100**, 2820–2828 (2011).

[107]   J. Kerssemakers, E. Munteanu, L. Laan, and T. Noetzel, "Assembly dynamics of microtubules at molecular resolution," *Nature* **442**, 709-712 (2006).

[108]   M. J. Schnitzer and S. M. Block, "Kinesin hydrolyses one ATP per 8-nm step," *Nature* **388**, 386–390 (1997).

[109]   R. Schneider, T. Glaser, M. Berndt, and S. Diez, "Using a quartz paraboloid for versatile wide-field TIR microscopy with sub-nanometer localization accuracy," accepted for publication in *Optics Express* (2012).

[110]   K. S. Thorn, J. A. Ubersax, and R. D. Vale, "Engineering the processive run length of the kinesin motor," *Journal of Cell Biology* **151**, 1093–1100 (2000).

[111]   R. Huber, J. Deisenhofer, P. M. Colman, M. Matsushima, and W. Palm, "Crystallographic structure studies of an IgG molecule and an Fc fragment," *Nature* **264**, 415–420 (1976).

[112]   S. He, A. Lam, Y. Jeune-Smith, and H. Hess, "Modeling negative cooperativity in streptavidin adsorption onto biotinylated microtubules," *Langmuir* **28**, 10635–10639 (2012).

[113]   A. Hoenger, M. Thormahlen, R. Diaz-Avalos, M. Doerhoefer, K. N. Goldie, J. Muller, and E. Mandelkow, "A new look at the microtubule binding patterns of dimeric kinesins," *Journal of Molecular Biology* **297**, 1087–1103 (2000).

[114]   G. Drewes, A. Ebneth, and E.-M. Mandelkow, "MAPs, MARKs and microtubule dynamics," *Trends in biochemical sciences* **23**, 307–311 (1998).

[115]   T. Korten, A. Månsson, and S. Diez, "Towards the application of cytoskeletal motor proteins in molecular detection and diagnostic devices," *Current opinion in biotechnology* **21**, 477–488 (2010).

[116]   W. H. Roos, O. Campas, F. Montel, G. Woehlke, J. P. Spatz, P. Bassereau, and G. Cappello, "Dynamic kinesin-1 clustering on microtubules due to mutually attractive interactions," *Physical Biology* **5**, 046004 (2008).

[117]   V. Bormuth, V. Varga, J. Howard, and E. Schaffer, "Protein friction limits diffusive and directed movements of kinesin motors on microtubules," *Science* **325**, 870–873 (2009).

[118]   S. M. Block, L. S. B. Goldstein, and B. J. Schnapp, "Bead movement by single kinesin molecules studied with optical tweezers," *Nature* **348**, 348–352 (1990).

[119]   Personal communication with Patrick Keller, Max Planck Institute of Molecular Cell Biology and Genetics (MPI-CBG), Leader of the antibody facility, Pfotenhauerstr. 108, 01307 Dresden, Germany.

[120]   N. Derr, B. Goodman, R. Jungmann, A. Leschziner, W. Shih, and S. Reck-Peterson, "Tug-of-war in motor protein ensembles revealed with a programmable DNA origami scaffold," *Science* 1226734, Published online 11 October 2012.

[121]   S. Jin, P. M. Haggie, and A. Verkman, "Single-particle tracking of membrane protein diffusion in a potential: Simulation, detection, and application to confined diffusion of CFTR Cl$^-$ channels," *Biophysical Journal* **93**, 1079–1088 (2007).

[122]   K. Svoboda and S. M. Block, "Force and velocity measured for single kinesin molecules," *Cell* **77**, 773–784 (1994).

[123]   C. L. Asbury, "Kinesin: world's tiniest biped," *Current opinion in cell biology* **17**, 89–97 (2005).

[124]   C. L. Asbury, A. N. Fehr, and S. M. Block, "Kinesin moves by an asymmetric hand-over-hand mechanism," *Science* **302**, 2130–2134 (2003).

[125]   B. J. Grant, D. M. Gheorghe, W. Zheng, M. Alonso, G. Huber, M. Dlugosz, J. A. McCammon, and R. A. Cross, "Electrostatically biased binding of kinesin to microtubules," *PLoS biology* **9**, 1–11 (2011).

[126]   L. A. Amos, "Microtubule structure and its stabilisation," *Organic and Biomolecular Chemistry* **2**, 2153–2160 (2004).

[127]   D. Chrétien and R. H. Wade, "New data on the microtubule surface lattice," *Biology of the Cell* **71**, 161–174 (1991).

[128]   A. N. Fehr, B. Gutiérrez-Medina, C. L. Asbury, and S. M. Block, "On the origin of kinesin limping," *Biophysical Journal* **97**, 1663–1670 (2009).

[129]   R. D. Vale and R. A. Milligan, "The way things move: looking under the hood of molecular motor proteins," *Science* **288**, 88–95 (2000).

[130]   S. M. Block, "Kinesin motor mechanics: binding, stepping, tracking, gating, and limping," *Biophysical Journal* **92**, 2986–2995 (2007).

[131]   A. L. Mattheyses, K. Shaw, and D. Axelrod, "Effective elimination of laser interference fringing in fluorescence microscopy by spinning azimuthal incidence angle," *Microscopy Research and Technique* **69**, 642–647 (2006).

[132]   J. Yajima and R. A. Cross, "A torque component in the kinesin-1 power stroke," *Nature chemical biology* **1**, 338–341 (2005).

[133]   C. Sönnichsen, S. Geier, N. Hecker, and G. Von Plessen, "Spectroscopy of single metallic nanoparticles using total internal reflection microscopy," *Applied Physics Letters* (2000).

[134]   C. L. Baciu, J. Becker, A. Janshoff, and C. Sönnichsen, "Protein–membrane interaction probed by single plasmonic nanoparticles," *Nano Letters* **8**, 1724–1728 (2008).

[135]   G. Wang, W. Sun, Y. Luo, and N. Fang, "Resolving rotational motions of nano-objects in engineered environments and live cells with gold nanorods and differential interference contrast microscopy," *Journal of the American Chemical Society* **132**, 16417–16422 (2010).

[136]   P. B. Johnson and R. Christy, "Optical constants of the noble metals," *Physical Review B* **6**, 4370–4379 (1972).

[137]   L. A. Peyser, A. E. Vinson, A. P. Bartko, and R. M. Dickson, "Photoactivated fluorescence from individual silver nanoclusters," *Science* **291**, 103–106 (2001).

[138]   Z. Xiu, Q. Zhang, H. L. Puppala, V. L. Colvin, and P. J. Alvarez, "Negligible particle-specific antibacterial activity of silver nanoparticles," *Nano Letters* **12**, 4271–4275 (2012).

[139]   J. Zheng and R. M. Dickson, "Individual water-soluble dendrimer-encapsulated silver nanodot fluorescence," *Journal of the American*

Chemical Society **124**, 13982–13983 (2002).

[140]   C. E. Aitken, R. A. Marshall, and J. D. Puglisi, "An oxygen scavenging system for improvement of dye stability in single-molecule fluorescence experiments," *Biophysical Journal* **94**, 1826–1835 (2008).

[141]   V. Jacobsen, P. Stoller, C. Brunner, V. Vogel, and V. Sandoghdar, "Interferometric optical detection and tracking of very small gold nanoparticles at a water-glass interface," *Optics Express* **14**, 405–414 (2006).

[142]   P. Kukura, H. Ewers, C. Müller, A. Renn, A. Helenius, and V. Sandoghdar, "High-speed nanoscopic tracking of the position and orientation of a single virus," *Nature Methods* **6**, 923–927 (2009).

[143]   J. Ortega-Arroyo and P. Kukura, "Interferometric scattering microscopy (iSCAT): New frontiers in ultrafast and ultrasensitive optical microscopy," *Physical Chemistry Chemical Physics* (2012).

[144]   V. Varga, C. Leduc, V. Bormuth, S. Diez, and J. Howard, "Kinesin-8 motors act cooperatively to mediate length-dependent microtubule depolymerization," *Cell* **138**, 1174–1183 (2009).

[145]   O. Wüseke, *Processivity and roadblocks - How kinesin-1 and kinesin-8 behave in the presence of obstacles on the microtubule lattice*, S. Diez, Eds., pp. 1–60, Bachelor Thesis (2009).

[146]   R. C. Dunn, "Near-field scanning optical microscopy," *Chemical reviews* **99**, 2891–2928 (1999).

[147]   R. Feynman, "There's Plenty of Room at the Bottom," *Talk at the Annual Meeting of the American Physical Society* (1959).

[148]   W. Haiss, N. T. K. Thanh, J. Aveyard, and D. G. Fernig, "Determination of Size and Concentration of Gold Nanoparticles from UV-Vis Spectra," *Analytical Chemistry* **79**, 4215–4221 (2007).

[149]   C. Gell, C. Friel, B. Borgonovo, and D. Drechsel, "Purification of tubulin from porcine brain," *Methods in Molecular Biology* **777**, A. Straube, Ed., 15–28 (2011).

[150]   R. E. Thompson, D. R. Larson, and W. W. Webb, "Precise nanometer localization analysis for individual fluorescent probes," *Biophysical Journal* **82**, 2775–2783 (2002).

[151] T. Ruckstuhl, J. Enderlein, S. Jung, and S. Seeger, "Forbidden Light Detection from Single Molecules," *Analytical Chemistry* **72**, 2117–2123 (2000).

List of figures

List of supporting figures

List of tables

Publications related to this work

1. R. Schneider, T. Glaser, M. Berndt, and S. Diez, "Using a quartz paraboloid for versatile wide-field TIR microscopy with sub-nanometer localization accuracy", *Optics Express* **21**, 3523-3539 (2013).

2. German patent: Application no. 10 2011 053 003.7: "Verfahren und Vorrichtung zur Weitfeld-Mikroskopie" (Applicants: Diez S, Schneider R, Glaser T, Venus B, Berndt M), filed August 26, 2011.

Conference participation related to this work

Talks

| 2012 | "Versatile tracking of fluorescent and scattering probes with nanometer precision", Spring meeting of the German Physical Society (DPG), **Berlin**, Germany |

Posters

2012	"Versatile tracking of fluorescent and scattering probes with nm-precision", 56th Biophysical Society Meeting, **San Diego**, CA, United States
2011	"Revival of prism-based TIR microscopy – Versatile tracking of motor proteins with nanometer precision", Saxon Biotechnology Symposium, **Dresden**, Germany
2011	"Revival of prism-based TIR microscopy – Versatile tracking of motor proteins with nanometer precision", Hot Nanoparticles and Nanostructures Symposium, **Leipzig**, Germany
2011	"Revival of prism-based TIR microscopy – Versatile tracking of motor proteins with nanometer precision", Gordon Research Conference, **New London**, NH, United States
2009	"Fast and precise optical tracking of individual motor proteins and motor systems using gold nanoparticles", Microscopy workshop of the German Research Foundation (DFG), **New York**, NY, United States

Curriculum vitae

Personal details

Name	René Schneider
Born	April 28, 1983 in Dresden, Germany

Education

2005 – 2008	Continued study of physics at the Technische Universität Dresden (Diploma 2008, thesis: *"Investigation of lipid bilayers using gold nanoparticles – influences on layer geometry, diffusion constant and fluorescence enhancement"*, Grade: 1.2 — Very Good)
2004 – 2005	Sabbatical in Australia, New Zealand and Indonesia
2002 – 2004	Study of physics at the Technische Universität Dresden (Prediploma 2004)
1993 – 2001	Secondary school "Gymnasium Dresden-Cotta" (specialization on the natural sciences; Abitur 2001)
1989 – 1993	Primary school in Dresden

Professional experience

since 2009	Scientist at the Max Planck Institute of Molecular Cell Biology and Genetics (MPI-CBG) and the B CUBE – Center for Molecular Bioengineering in Dresden
2007 – 2009	Assistant scientist at the Institute of Applied Photophysics (IAPP) in Dresden
2002 - 2003	Assistant tutor for undergraduate students at the Institute of Theoretical Physics (ITP, Courses: Theoretical Mechanics & Electrodynamics)

Awards and nominations

2011	Representative for the biophysics program pillar in the internal evaluation round of the MPI science advisory board
2011	DIGS-BB Travel Award for the participation in the Gordon Research Conference on Muscle & Molecular Motors in New London, NH, United States, 2011
2009	Scholarship of the International Max Planck Research School (IMPRS) and the Dresden International Graduate School for Biomedicine and Bioengineering (DIGS-BB)

Acknowledgement

During my PhD thesis, I enjoyed being surrounded by many supporting individuals who contributed to the outcome of this thesis in many different ways. Although it is impossible to mention everyone by name, I will at least try to take this unique opportunity to express my gratitude to all of them.

First and foremost, I wholeheartedly thank my supervisor *Stefan Diez*, who granted me the opportunity to work in his lab and turn this project into my dissertation. His fair, enthusiastic, and ever optimistic character not only piloted me through this topic, but impacted sustainably on my way of thinking about myself, my friends, and of course, science. During the three and a half years of supervision, it was stunning to experience how he could convert depression into euphoria, one out of many reasons that make his impact on this thesis invaluable. Furthermore, I would like to thank my thesis advisory committee members *Joe Howard* and *Marino Zerial*, who always supported my project and ideas and I am grateful for the time that we spent together during the meetings.

I am particularly grateful to my colleagues in the lab who always provided a friendly, cooperative, and entertaining atmosphere, which was essential to eventually have fun doing science independent of the outcome of some protocol or experiment. Especially without the help of *Corina Bräuer* and *Cornelia Thodte*, our good souls taking care of us careless students, this thesis would have never come to the stage presented here.

Furthermore, I want to thank a couple of colleagues who contributed to the thesis through their previous work: I profited from the initial work of *Michael Berndt*, who conceptually designed the very first prototype of a parabolic prism. In this context, I want to express my gratitude to *Till Glaser, Volkmar Giggel, Tiemo Anhut*, and *Brüne Venus* for the help with manufacturing and patenting our novel imaging approach. A core tool utilized in this thesis was the FIESTA tracking software written by *Felix Ruhnow* and *David Zwicker*. I'm very glad about having received extensive Matlab support from *Felix* and I always wondered how patiently he handled every single dumb programming

question I had. The previous work of *Till Korten* on kinesin-1 being affected by streptavidin roadblocks was of great importance to this thesis and I am particularly grateful having received his comments and expertise. It was a stroke of luck that *Wim Walter* joined our lab. He helped me with setting up the experimental route of my thesis and introduced me to the mutation, expression and purification of proteins. Eventually, I enjoyed being supported by *Bert Nitzsche*, who helped me a lot with considering various optical details involved in novel imaging approaches. Furthermore, looking at his way of doing experiments, I always had the feeling being behind by some orders of 'skill' magnitude. I am happy that he was willing to share some of his tricks. Finally, I have to thank *Christian Heck, Wiebke Jahr*, and *Lara Scharrel*, for not being distracted by the projects I offered them for their bachelor, diploma, and master theses. I enjoyed every minute working together with them, which had the appreciable effect of turning 'my' into 'our' research topic.

Many more people were involved in turning the PhD period into a lot of fun. First of all, I thank *Veikko Geyer* and *Oliver Wüseke* for several science seminars in the Nordbad, *Gero Fink* for celebrating a daily five minutes of laugh-out-loud sessions in the lab, *Marcus Braun* for introducing me to the fascinating idea of 'being authentic', *Barbara Lindemann* and *Antje Franz* for taking care of the bureaucratic part of academia, *Aniruddha Mitra, Juliane Beyer*, and *Rahul Grover* for keeping up the interaction between the MPI and B CUBE labs, and *Zdenek Lansky* for several squash sessions with ever-and-ever increasing intensity and, more importantly even, for defending the 'place de garbage', one of Dresden's finest canteens, against any attempts of boycott. Once again, I want to appreciate the efforts of *Wim, Bert, Marcus, Till, Nina*, and *Stefan* in proofreading of and commenting on the manuscript of my thesis.

Last but most important, I would like to thank my family, especially my parents, without whose sacrificial help I would have never ended up as a PhD student. Further immeasurable support I gained from *Nina Schwab*, actually for much longer now than just the timespan of this thesis. Several times during the past years, it was her extremely positive and confident nature that cheered me up when things were looking bad.